# X-ray observations of black hole and neutron star binary systems

Dissertation
zur Erlangung des Grades eines
Doktors der Naturwissenschaften
der Fakultät für Mathematik und Physik
der Eberhard-Karls-Universität Tübingen

vorgelegt von

Sonja Fritz

aus Tübingen
2008

| | |
|---|---|
| Selbstverlegt von: | S. Fritz, Kelternstr. 27, 72555 Metzingen |
| Tag der mündlichen Prüfung: | 10. Juli 2008 |
| Dekan: | Prof. Dr. N. Schopohl |
| 1. Berichterstatter: | Prof. Dr. A. Santangelo |
| 2. Berichterstatter: | Prof. Dr. R. Staubert |

## Erweiterte deutsche Zusammenfassung

**Fritz, Sonja**

### Röntgenbeobachtungen von Schwarzloch- und Neutronensternsystemen

Schwarze Löcher und Neutronensterne sind die kompakten Überbleibsel massiver Sterne am Ende ihres Lebens. Da alle nuklearen Reaktionen in ihrem Inneren zum Erliegen gekommen sind, senden sie selbst keine Strahlung mehr aus. Isolierte kompakte Objekte sind daher gar nicht oder nur nur sehr schwer zu entdecken. Befindet sich ein solcher Himmelskörper jedoch in einem Doppelsternsystem, so kann er von seinem Begleitstern Materie akkretieren. Hierbei entsteht Strahlung die im Röntgenbereich beobachtbar ist. Eine Übersicht über die hierbei relevanten Prozesse ist in Kapitel 2 gegeben.

Im Rahmen dieser Arbeit wurden Röntgenbeobachtungen beider Typen kompakter Objekte, Schwarzer Löcher und Neutronensterne, analysiert:

Der erste Teil der Arbeit ist einer detailierten Analyse des Breitbandspektrums des Schwarzloch-Doppelsternsystems Cygnus X-1 gewidmet, das eine der hellsten persistenten Quellen am Röntgenhimmel ist. Cyg X-1 wurde Ende 2004 simultan von den drei Satelliten *XMM-Newton*, *RXTE* und *INTEGRAL* beobachtet. Dank des grossen Energiebereichs der duch diese Missionen abgedeckt wird (2.8 keV– 1 MeV) resultierten aus diesen Beobachtungen einige der höchstaufgelösten Breitbandspektren die jemals aufgenommen wurden. Da Cyg X-1 eigentlich zu hell ist um von *XMM-Newton* in einem der Standardbeobachtungsmodi beobachtet zu werden, musste ein neuer Modus für die EPIC-pn Kamera entwickelt werden. Dieser sogenannte “Modified Timing mode” und Details zu seiner Kalibrierung sind in Kapitel 4 beschrieben. In den beiden darauffolgenden Kapiteln werden die Ergebnisse der Datenanalyse dargestellt, die in zwei Hauptbereiche aufgeteilt war. Auf der einen Seite stand eine Untersuchung des Breitband-Kontinuums mit dem Ziel, verschiedene Modelle für das Comptonisierende Plasma zu testen, welches das Schwarze Loch und die Akkretionsscheibe umgibt, auf der anderen Seite eine detailierte Analyse der Fe K$\alpha$ Region des Spektrum um eine relativitische Verbreiterung der Eisenlinie zu bestätigen. Die Analyse des Breitband-Kontinuums wurde mit *RXTE* und *INTEGRAL* durchgeführt und wird in Kapitel 3 beschrieben. Für die Eisenlinie wurden zwar die Kontinuumsparameter mit *RXTE* bestimmt, die hauptsächliche Analyse beruht jedoch auf *XMM-Newton* Daten (Kapitel 5). Im Breitband-Kontinuum wurde bei Energien über ~300 keV ein Exzess detektiert, ein sogenannter “hard tail”. Dieser “hard tail” ist typisch für den Hard Intermediate State von Schwarzen Löchern

in dem sich Cygnus X-1 während der Beobachtungen befand und kann mit einer nicht-thermischen Komponente im Comptonisierenden Plasma erklärt werden. Die ebenfalls für diesen State typische verbreiterte Eisenlinie konnte in den Daten von *XMM-Newton* nachgewiesen werden. Im Unterschied zu früheren Messungen mit dem amerikanischen *Chandra* Satelliten eignen sich für die Beschreibung des Linienprofils in den *XMM-Newton* Daten Modelle die auf der Kerr-Metrik beruhen jedoch besser als Modelle, die die Schwarzschild-Metrik zugrunde legen.

Im zweiten Teil dieser Arbeit werden die Ergebnisse von zwei Jahren *INTEGRAL* Beobachtungen des Neutronensternsystems 4U 1907+09 vorgestellt. Das Hauptaugenmerk lag hier auf der Untersuchung der zeitlichen Variablilität der Quelle, da 4U 1907+09 eines der wenigen bekannten Objekte ist, das über einen Zeitraum von 20 Jahren (seit der ersten Bestimmung der Pulsperiode in 1983) einen konstanten “spin-down” Trend zeigt. Dieses Verhalten kehrte sich 2004 komplett um und 4U 1907+09 zeigt seitdem einen deutlichen “spin-up” mit konstant abnehmender Pulsperiode. Neben der Untersuchung dieser zeitlichen Variablilität wurde auch eine Analyse des 5–90 keV Spektrums vorgenommen, das zwei Zyklotronlinien aufweist. Mit Kenntnis der Energie dieser Linien ist es möglich, die Stärke des Magnetfeldes von 4U 1907+09 zu berechnen, was Rückschlüsse auf die Akkretionsgeometrie und die zeitliche Entwicklung der Pulsperiode zulässt (Kapitel 7).

## Extended Abstract

**Fritz, Sonja**

### X-ray observations of black hole and neutron star binary systems

Black holes and neutron stars are compact remnants of massive stars at the endpoint of stellar evolution. As they have consumed all their nuclear fuel they are not radiating themselves anymore, which makes isolated compact objects rather difficult if not even impossible to discover. If they are found in binary systems, however, they may accrete matter from their stellar companion, thereby producing radiation that can be observed in the X-ray regime (Chapter 2).

In this thesis I analyze and discuss X-ray observations of two binary systems, containing a black hole and a neutron star, respectively:

The first part of the work is dedicated to a detailed broadband study of the black hole binary Cygnus X-1, which is one of the brightest persistent sources in the X-ray sky. Cyg X-1 was observed at the end of 2004 simultaneously by the three satellites *XMM-Newton*, *RXTE*, and *INTEGRAL*. As these three instruments cover an energy range from 2.8 keV– 1 MeV, one of the best resolved broadband spectra ever was obtained. As Cyg X-1 is too bright actually to be observable by *XMM-Newton* in its standard modes, a new observing mode (called the "Modified Timing mode") has been developed for the EPIC-pn camera. This mode and its calibration are described in Chapter 4. In the two following chapters the results of the data analysis are presented, which was split in two main parts. On the one hand a study of the broadband continuum was performed to constrain models for the Comptonizing plasma surrounding the black hole and its accretion disk (using *RXTE* and *INTEGRAL*, Chapter 3), on the other hand a detailed analysis of the Fe K$\alpha$ region was conducted to search for effects of relativistic line broadening (using *XMM-Newton*, Chapter 5). The broadband continuum is found to show a hard tail above ~300 keV (as it is expected for the Hard Intermediate State during which the observations took place) which could be explained in terms of non-thermal Comptonization. The presence of a broadened iron line, which is also expected in this state, could be confirmed in the *XMM-Newton* analysis. Contrary to results by the *Chandra* observatory, however, Kerr models are favored for the description of the line profile in the *XMM-Newton* observations.

In the second part of this thesis the results of two years of *INTEGRAL* observations of the neutron star binary 4U 1907+09 are reported. The main focus of this analysis is a study of the timing behavior of this source, as 4U 1907+09 is one of the few sources known to show a steady spin-down behavior over the

last 20 years since the first measurement of its pulse period in 1983. This behavior changed completely during the *INTEGRAL* observations in 2004 when 4U 1907+09 underwent a complete torque reversal. Since then the pulse period of the neutron star is constantly decreasing. In addition to the timing also an analysis of the 5–90 keV spectrum is performed. The presence of two cyclotron lines in the spectrum allows the calculation of the magnetic field strength of this object. With the knowledge of this field strength it is in turn possible to draw conclusions on the accretion geometry and the spin behavior (Chapter 7).

# Contents

**1 Introduction** **15**
1.1 X-ray Binaries . . . 16
1.1.1 Neutron Star Binaries . . . 20
1.1.2 Black Hole Binaries . . . 23
1.2 Instrumentation . . . 24
1.2.1 Collimator Techniques: *RXTE* . . . 25
1.2.2 Coded Mask Techniques: *INTEGRAL* . . . 26
1.2.3 Wolter Telescopes: *XMM-Newton* . . . 30
1.3 Thesis outline . . . 32

**I Black Hole Binaries: Cygnus X-1** **35**

**2 Radiation Processes in Black Hole Systems** **37**
2.1 Black body Radiation . . . 38
2.2 Comptonization . . . 40
2.3 Compton Reflection . . . 42
2.4 Pair production . . . 44
2.5 Models . . . 45
2.5.1 The *XSPEC* model `compTT` . . . 46
2.5.2 The *XSPEC* model `eqpair` . . . 46

**3 The broadband spectrum of Cygnus X-1** **50**
3.1 The Cygnus X-1 system . . . 50
3.2 The states of black holes . . . 51
3.3 Observations and data reduction . . . 55
3.4 Comparison with the long term monitoring campaign . . . 58
3.4.1 Broken power law Fits . . . 60
3.4.2 `compTT` Fits . . . 61
3.4.3 `eqpair` Fits . . . 63
3.4.4 Time averaged broad band spectra . . . 66

3.5 Summary and Discussion . . . . . 69

**4 The Relativistic Iron Line – Techniques 75**
4.1 Relativistically broadened Iron lines . . . . . 75
4.2 Models . . . . . 78
4.2.1 The *XSPEC* model `diskline` . . . . . 79
4.2.2 The *XSPEC* model `laor` . . . . . 80
4.2.3 The *XSPEC* model `kdblur` . . . . . 80
4.3 The Modified Timing mode of *XMM-Newton* . . . . . 81
4.3.1 Observation of bright sources with *XMM-Newton* . . 81
4.3.2 Calibration of the Modified Timing mode – The new response matrix . . . . . 82
4.3.3 Calibration of the Modified Timing mode – CTE effects 86

**5 The Relativistic Iron Line – Analysis 90**
5.1 Observations and data reduction . . . . . 91
5.2 Structure of the line . . . . . 91
5.2.1 Composition of the *XSPEC* model . . . . . 92
5.2.2 Another way of doing it: `kdblur` . . . . . 103
5.3 Variability of the line . . . . . 106
5.3.1 Variability with time . . . . . 106
5.3.2 Variability with luminosity . . . . . 106
5.4 Summary and Discussion . . . . . 109
5.4.1 Comparison with *Chandra* . . . . . 111

**II Neutron Star Binaries: 4U 1907+09 115**

**6 Some Neutron Star X-ray Binary Physics 117**
6.1 Accretion onto highly magnetized Neutron Stars . . . . . 117
6.2 Variability of Neutron Star XRBs . . . . . 120
6.3 Cyclotron Resonant Scattering Features . . . . . 122

**7 A torque reversal of 4U 1907+09 126**
7.1 The 4U 1907+09 system . . . . . 126
7.2 Observation and data reduction . . . . . 127
7.3 Spectral Analysis . . . . . 129
7.4 Timing Analysis . . . . . 133
7.4.1 The X-ray light curve of 4U 1907+09 . . . . . 133
7.4.2 Pulsar Period and Pulse Profiles . . . . . 135
7.5 Summary and Discussion . . . . . 139

**III Summary and Outlook 147**

**8 Summary and Outlook 149**
8.1 Cygnus X-1 . . . . . 149
8.1.1 Broadband . . . . . 150
8.1.2 Iron Line . . . . . 150
8.2 4U 1907+09 . . . . . 151

**Bibliography 155**

**A Calibration of Modified Timing mode 164**

**Acknowledgments 172**

**Curriculum Vitae 174**

# List of Figures


1.1 Roche-Potential . . . . . 17
1.2 Wind accretion in the Bondi-Hoyle model . . . . . 19
1.3 Wind accretion, hydrodynamical simulations . . . . . 19
1.4 Be star accretion . . . . . 20
1.5 Endpoints of stellar evolution . . . . . 21
1.6 Principle of the collimator technique . . . . . 26
1.7 Advanced principle of the collimator technique . . . . . 26
1.8 The *RXTE* spacecraft . . . . . 27
1.9 Coded mask imaging . . . . . 29
1.10 The *INTEGRAL* spacecraft . . . . . 30
1.11 The principle of Wolter telescopes . . . . . 32
1.12 The *XMM-Newton* spacecraft . . . . . 33
2.1 Accretion in black hole systems . . . . . 38
2.2 Black body radiation . . . . . 40
2.3 Wien's displacement law . . . . . 40
2.4 Compton scattering . . . . . 41
2.5 Cross sections . . . . . 44
2.6 Differences between a thermal and a non-thermal plasma . . 48
3.1 The states of black hole binaries . . . . . 53
3.2 Jet-disk coupling and state transitions . . . . . 56
3.3 *RXTE* ASM light curve of Cyg X-1. . . . . 58
3.4 Cyg X-1 light curves . . . . . 59
3.5 Correlation between $\Gamma_1$ and $\Gamma_2$ . . . . . 62
3.6 Correlation between Compton y and $\Omega/2\pi$ . . . . . 64
3.7 Correlation between $\Gamma_2$ and $\ell_h/\ell_s$ . . . . . 66
3.8 Correlation between $\Omega/2\pi$ and $\ell_h/\ell_s$ . . . . . 67
3.9 `eqpair` model . . . . . 69
3.10 Strength of spectral components . . . . . 71
3.11 Orbital light curve of Cyg X-1 . . . . . 72
3.12 Correlation between $\tau$ and $\ell_h/\ell_s$ . . . . . 74
4.1 Theory of iron line profiles . . . . . 76

| | | |
|---|---|---|
| 4.2 | Iron line profiles for different spin parameters | 77 |
| 4.3 | Iron line profiles for different emissivity indices | 78 |
| 4.4 | Iron line profiles for different inclination angles | 79 |
| 4.5 | Comparison of a simulated Modified Timing mode observation and a standard Timing mode Observation | 83 |
| 4.6 | Cut through redistribution matrix | 84 |
| 4.7 | Comparison of the standard Timing mode RMF and the Modified Timing mode RMF for the thick filter | 87 |
| 4.8 | CTE effects - shift of Fe line position | 88 |
| 4.9 | Calibration of CTE effects | 89 |
| 5.1 | XMM-Newton spectrum of obs 2 | 93 |
| 5.2 | `diskline` fit to *XMM-Newton* obs2 | 96 |
| 5.3 | Confidence contours of obs2 and obs3 | 103 |
| 5.4 | Inclinations found using `kdblur` | 104 |
| 5.5 | Variation of the iron line with time | 108 |
| 5.6 | XMM-Newton light curves | 109 |
| 5.7 | Variation of the iron line with luminosity | 110 |
| 5.8 | Comparison XMM – *Chandra* | 112 |
| 6.1 | Accretion column | 118 |
| 6.2 | Inside of the accretion column | 119 |
| 6.3 | Accretion geometry in the Ghosh&Lamb model | 121 |
| 6.4 | Correlation between spin-up and period/luminosity | 122 |
| 6.5 | Cyclotron lines in 4U 0115+63 | 124 |
| 6.6 | Line shape of cyclotron lines | 125 |
| 7.1 | Orbital light curve of 4U 1907+09 | 128 |
| 7.2 | ISGRI image of the 4U 1907+09 region | 131 |
| 7.3 | FDC fit to 4U 1907+09 spectrum | 132 |
| 7.4 | IBIS (ISGRI) light curve of revolution 193 | 136 |
| 7.5 | Evolution of the 4U 1907+09 pulse period | 137 |
| 7.6 | Close up of periods found for 4U 1907+09 | 139 |
| 7.7 | 4U 1907+09 pulse profiles for different revolutions | 140 |
| 7.8 | 4U 1907+09 energy resolved pulse profiles | 141 |
| 8.1 | Period evolution of 4U 1907+09 in the Suzaku era | 152 |
| A.1 | Comparison of the standard Timing mode RMF and the Modified Timing mode RMF for the thin1 filter | 170 |
| A.2 | Comparison of the standard Timing mode RMF and the Modified Timing mode RMF for the medium filter | 171 |

# List of Tables


| | | |
|---|---|---|
| 1.1 | RXTE instruments | 28 |
| 1.2 | INTEGRAL instruments | 31 |
| 1.3 | XMM-Newton instruments | 33 |
| 3.1 | Cyg X-1 system parameters | 52 |
| 3.2 | Observation log for *INTEGRAL* | 57 |
| 3.3 | Observation log for *RXTE* | 57 |
| 3.4 | Statistical properties of the light curves | 60 |
| 3.5 | Best fit parameters for the broken power law model. | 63 |
| 3.6 | Best fit parameters for the `compTT` model. | 65 |
| 3.7 | Best fit parameters for the `eqpair` model. | 68 |
| 3.8 | Best fit parameters for the time averaged `eqpair` model. | 70 |
| 4.1 | Observation modes of the EPIC cameras | 82 |
| 5.1 | Observation log for *XMM-Newton* | 91 |
| 5.2 | Fits using the `diskline` model | 94 |
| 5.3 | Fits using the `laor` model | 95 |
| 5.4 | Fits using the `diskline` model and a smeared edge | 97 |
| 5.5 | Fits using the `laor` model and a smeared edge | 98 |
| 5.6 | Fits using the `diskline` model and a smeared edge (with *RXTE* continuum parameters) | 101 |
| 5.7 | Fits using the `laor` model and a smeared edge (with *RXTE* continuum parameters) | 102 |
| 5.8 | Predictions for the disk viewing angle $\theta$. | 103 |
| 5.9 | Fits using the `kdblur` model | 105 |
| 5.10 | Variability of the iron line with luminosity | 107 |
| 7.1 | Ephemeris used for binary correction of 4U 1907+09 | 129 |
| 7.2 | 4U 1907+09 log of observations | 130 |
| 7.3 | Best fit parameters for FDC model | 133 |
| 7.4 | Best fit parameters for NPEX model | 134 |
| 7.5 | Flares in the X-ray light curve of 4U 1907+09 | 135 |
| 7.6 | Period measurements of 4U 1907+09 | 138 |
| A.1 | Log of observations. – Part I | 165 |

A.2 Log of observations. – Part II . . . . . 166
A.3 Log of observations. – Part III . . . . . 167
A.4 Log of observations. – Part IV . . . . . 168
A.5 Log of observations. – Part V . . . . . 169

# Chapter 1

# Introduction

*"You look at a star for two reasons,*
*because it is luminous,*
*and because it is impenetrable."*
Victor Hugo (Les Misérables)

The stars discussed in this thesis are indeed some of the most *"luminous"* stars in the sky[1]. However, I am not talking about the "classical" sky as it has been observed since ancient times with the naked eye but in fact about the picture that can be seen when observing the sky in the light of X- and $\gamma$-rays. These observations reveal a completely different picture of the sky. Even the stars are no "normal" stars any more – among the sources seen in these higher energy bands are the relics of stars at the end of their life: white dwarfs, neutron stars, or black holes. And unlike the calm and steady sea of lights seen in the optical band the X-ray sky is highly variable and unpredictable. Some sources undergo split second changes of their luminosity while others show giant outbursts.

Seeing the sky in X-rays is seeing the hottest places of the universe. For example the main source of the observed X-rays from the above mentioned compact objects is matter which is accreted onto them from a companion star and thereby heated up to many million K. By the interaction of the stars (or better sources) it is therefore possible to gain a lot of information about them although they are *"impenetrable"* themselves. In the following section the conditions under which mass transfer from one star to another can take place will be explained before the sources discussed in this thesis – neutron stars and black holes – are described in more detail.

[1]Compared to extra galactic sources like Active Galactic Nuclei (AGN) – which upon their discovery were believed to be stars until their true identity as super massive black holes was revealed – the physically defined luminosity of the objects described in this thesis is of course lower by several orders of magnitude.

## 1.1 X-ray Binaries

Binary systems are much more common in nature than it might appear at the first glance as about half of the stars in the sky are not single stars but rather composed in binary systems or even systems with more components. So it is only natural that the study of binary systems traces back to the beginnings of astrophysics for those studies provide the opportunity to get information that cannot be gained for single stars. Binary systems provide for example the best method to determine the mass of stars through Kepler's third law[2], a parameter which is essential for any further analyses of the star.

The binary systems discussed in this thesis are of a special kind as one of their constituents is not a "normal" star but a compact object, meaning in this case a neutron star or a black hole. The compact object is accreting matter from its companion, leading to the emission of X-rays as the energy which is released due the accretion process is

$$\Delta E_{\mathrm{acc}} \propto \frac{M}{R} \quad , \tag{1.1}$$

in other words the more compact an object the more efficient the accretion process. Typical values for the energy released by accretion onto a neutron star are of the order of 100 keV for electrons and 200 MeV for protons (due to their higher mass). The luminosity of an accreting system depends on the mass accretion rate $\dot{M}$, with

$$L_{\mathrm{acc}} = \frac{GM\dot{M}}{R} \tag{1.2}$$

if all released energy would be radiated away. However, there is an upper limit to the luminosity given by the equilibrium of the gravitational force of the source and the radiation pressure due to X-ray luminosity. For the case of spherical symmetric accretion of fully ionized matter this limit is reached at the so called Eddington luminosity (e.g. Padmanabhan 2000)

$$L_{\mathrm{Edd}} = \frac{4\pi G m_{\mathrm{p}} c}{\sigma_{\mathrm{T}}} M \approx 1.3 \cdot 10^{38} \frac{M}{M_{\odot}} \mathrm{erg\,s^{-1}} \quad . \tag{1.3}$$

In reality the accretion processes are hardly spherical symmetric resulting in the observation of sources with luminosities above the Eddington limit.

The accretion process itself can occur via three different mechanisms:

1. **Roche lobe overflow:** The gravitational potential in a binary system (exemplified for a mass ratio of 5:1 in Fig. 1.1) is described by the Roche potential

[2] For the determination of the masses and radii of the two constituents separately further spectroscopic techniques are required.

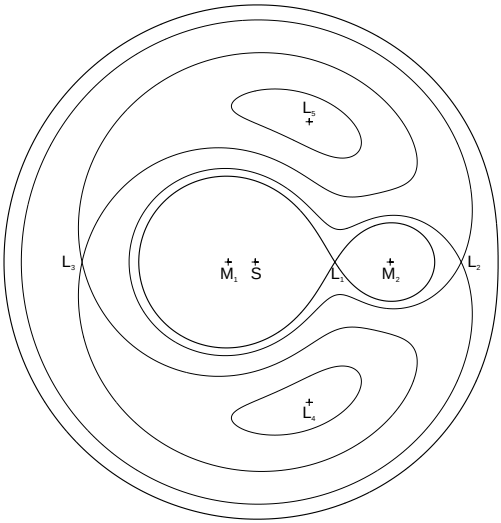


Figure 1.1: Equipotential lines of the Roche potential for a mass ratio of $M_1/M_2 = 5/1$. $M_1$ and $M_2$ denote the position of the stars, $S$ is the center of gravity, and $L_x$ mark the five Lagrangian points (Kretschmar 1996).

(Frank et al. 1992)

$$\Phi(\vec{r}) = -\frac{GM_1}{|\vec{r}-\vec{r_1}|} - \frac{GM_2}{|\vec{r}-\vec{r_2}|} - \frac{1}{2}(\omega \times \vec{r})^2 \tag{1.4}$$

with $M_1$ and $M_2$ being the masses of the two stellar components, $r_1$ and $r_2$ the respective position vectors, and $\omega$ the angular velocity of the system. From this equation the size of the so called "Roche lobe" – the surface within which a particle is bound to one of the systems components – can be derived. If the companion star is evolved and has therefore grown in radius it can fill its Roche lobe and matter can flow over the inner Lagrangian point L1 (which is a saddle point of the function $\Phi$) onto the compact object. This material, however, has too much angular momentum due to the rotation of the star and can not directly fall down onto the compact object. Instead an accretion disk forms in which the material loses angular momentum and moves slowly inwards until it can be accreted onto the compact object.

2. **Wind accretion:** In the case of wind accretion the material has almost no angular momentum and hence no (or only a very small) accretion disk forms. This kind of accretion dominates in systems where the companion

star is of an early type and drives a strong stellar wind with $\dot{M}_{\rm W} \approx 10^{-6} - 10^{-5} {\rm M}_{\odot}\,{\rm yr}^{-1}$ out of which 0.01-0.1% are accreted onto the compact object (Frank et al. 1992). Although only a small part of the wind is accreted the mass accretion rate can still be sufficient to make the source radiate close to the Eddington limit. The accretion process itself is described roughly in the cylinder symmetric Bondi-Hoyle model (Bondi & Hoyle 1944): only material from within a cylindrical radius of

$$r_{\rm acc} = \frac{2GM_1}{v_W^2 + v^2} \tag{1.5}$$

is accreted by the compact object, where $v$ is the orbital velocity and $v_W$ the velocity of the stellar wind. For a typical OB supergiant system the wind velocity is $v_w \approx 1 - 2 \cdot 10^3 {\rm km\,s}^{-1}$ and therefore $r_{\rm acc} \approx 10^{10}$ cm. This value is much smaller than the distance between the star and the compact object which is usually of the order of $10^{12}$ cm. Outside this radius the kinetic energy of the gas dominates the gravitational pull of the compact object and the wind is mostly unaffected by the compact object. Behind the compact object a part of the stellar wind forms the so called "accretion wake" as is shown in Fig. 1.2.

The Bondi-Hoyle model described here is rather simple as it assumes cylinder symmetry. The real process, however, turns out to be rather asymmetric as hydrodynamical simulations show (Mauche et al. 2007, and references therein). In Fig. 1.3 typical results of a simulation for the neutron star X-ray binary Vela X-1 are shown: Coriolis and centrifugal forces cause the hot, low density, high velocity flow down to the neutron star to curve clockwise while a bow shock and two flanking shocks are formed where the wind collides with the flow.

3. **Be-star mechanism:** Be stars are a special kind of spectral type B stars showing several characteristic hydrogen emission lines. These lines originate from a disk in the equatorial plane of the star which forms due to its rapid rotation. As this disk is rather extended (up to several stellar radii) the compact object crosses it as it approaches periastron and accretes material (Fig. 1.4). This is visible as X-ray outburst. As the compact object moves on the accretion rate decreases and also the X-ray luminosity drops. However, this process does not necessarily occur at each periastron passage of the compact object as the disk of the Be star seems to be unstable at least in some sources as for example A 0535+26.

Depending on the mass of the companion star, X-ray binary (XRB) systems are divided into Low Mass XRBs (LMXBs) and High Mass XRBs (HMXBs).

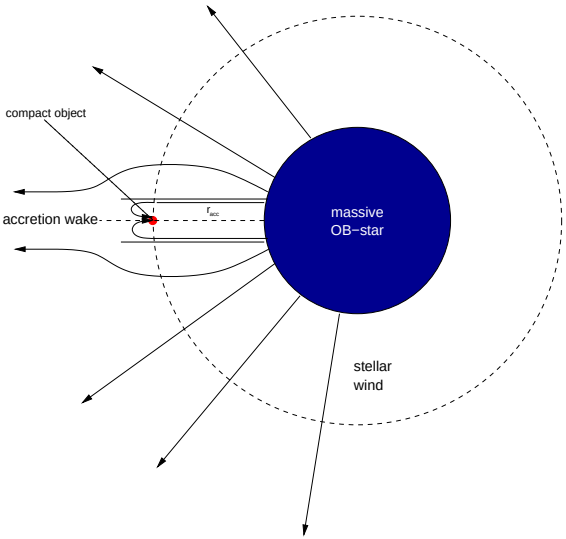


Figure 1.2: Wind accretion in the Bondi-Hoyle model: material from inside $r_{\rm acc}$ is accreted onto the compact object (Figure from Kreykenbohm et al. 2004).

Members of the first class have a companion star of the spectral type G to M with a mass of one or less solar masses. In this case the emission in X-rays exceeds the optical luminosity by a factor of $10^2$ to $10^4$. As these dwarf stars usually do not emit a strong stellar wind, the main accretion mechanism in LMXBs is Roche lobe overflow. Therefore the companion needs to be evolved and to fill its Roche lobe,

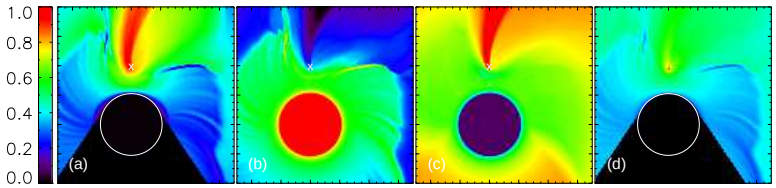


Figure 1.3: Hydrodynamical simulations of wind accretion for the Vela X-1 system (Mauche et al. 2007). Color coded are (a) the temperature $log(T)$ [K] = [4.4,8.3], (b) the density $log(n)$ [cm$^{-3}$] = [7.4,10.8], (c) the velocity $log(v)$ [km s$^{-1}$] = [1.3,3.5], and (d) the ionization parameter $log(\xi)$ [erg cm s$^{-1}$] = [1.1,7.7]. The position of the neutron star is marked by the cross.

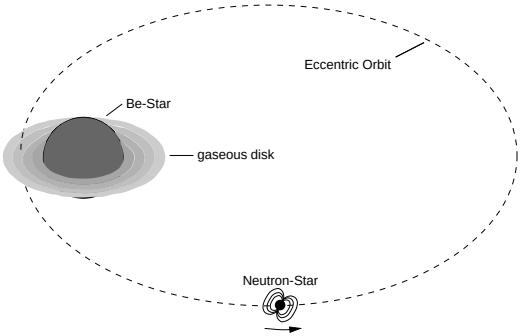


Figure 1.4: Be star accretion mechanism (Kretschmar 1996): the neutron star can cross the gaseous disk around the companion and accrete matter.

making LMXBs rather old systems with typical ages $\geq 10^9$ years. In contrast the companions of HMXBs are young OB supergiants with 10 or more solar masses. The emission of a HMXB system is dominated by the optical emission of the companion (with $L_x/L_{opt} \approx 10^{-3}...10$), which in most cases also drives a strong stellar wind and therefore allows the compact object to accrete via the second described mechanism (van den Heuvel 1975).

In total there are believed to be not more than a few hundred X-ray binary systems in the galaxy (Grimm et al. 2003; Psaltis 2006), as the evolution of a "normal" binary system to a system with an accreting compact object is rather improbable. For instance the progenitor stars of the compact object are believed to be too large to fit in the rather tight orbits and moreover the supernova explosion of this stars might disrupt most of the systems. However, there are some possible (but poorly understood) scenarios like common-envelope evolution, asymmetric supernova explosions or two- and three-star interactions in globular clusters which might explain the existence of binaries with an accreting compact object (Tauris & van den Heuvel 2006, and references therein).

After looking at binary systems as a whole the following sections now provide a closer look on the nature of the compact object. These sources are the final stages in the evolution of a star. If a star is not disrupted completely at the end of its life it ends either as white dwarf, neutron star, or black hole – depending on its mass. Fig. 1.5 shows an simplified overview of this dependency.

### *1.1.1 Neutron Star Binaries*

As shown in Fig. 1.5, neutron stars (NS) result from stars with initial masses greater than about 6 solar masses (Camenzind 2007). A comprehensive discussion

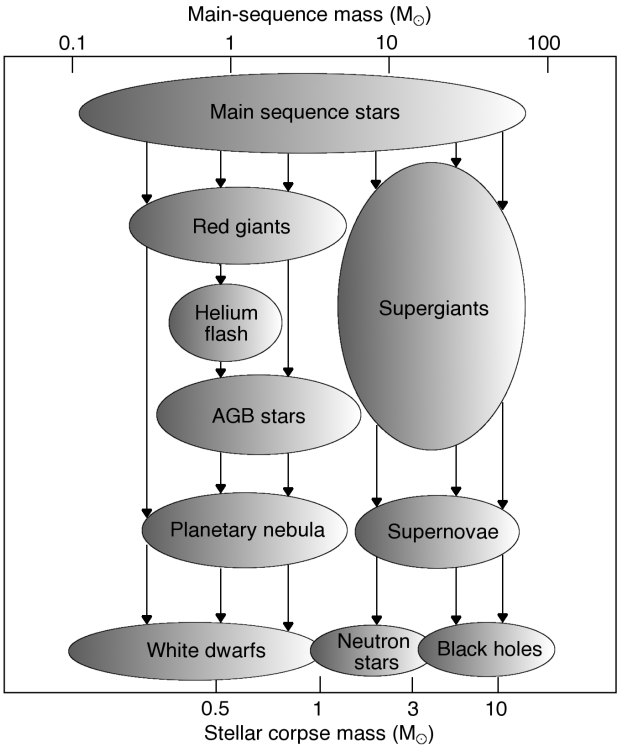


Figure 1.5: Overview of the final stages of stellar evolution shown as function of their initial mass (Figure after Camenzind 2007).

of stellar evolution, however, is beyond the scope of this thesis but can be found, e.g., in Kippenhahn & Weigert (1994). The crucial step in NS formation occurs when all of the nuclear fuel of the initial star is exhausted and the core becomes dynamically unstable and starts to collapse. Inside the core neutrons are build by the electrons and protons via inverse $\beta$-decay. The collapsed core forms a sphere with about 10 km radius and a mean density of $10^{14}\,\mathrm{g\,cm^{-3}}$ (Srinivasan 1997) that is balanced against gravity by the pressure of the degenerate neutron fluid – a neutron star is born. The envelope of the initial star is expelled due to the rebounce of the incoming shock wave on the NS surface in a supernova Type II explosion[3]. The masses of most of the NSs lie in the narrow range of 1.25

[3]A detailed description of supernovae can be found in Woosley & Weaver (1986) and Woosley et al. (2002)

– 1.44 $M_\odot$ (Camenzind 2007) but there are also more massive NSs found with masses up to 2.1 $M_\odot$ (Nice et al. 2005). As the magnetic flux of the progenitor star (which can have a magnetic field strength of $\sim 1\,\mathrm{kG}$ in the case of an O star, see Donati et al. 2006) is conserved during the collapse[4] and as the magnetic field strength is proportional to $r^{-2}$, NSs can possess some of the strongest magnetic fields that exist in nature with field strengths up to $10^{15}\,\mathrm{G}$ (so-called magnetars, see e.g. Harding & Lai 2006). The magnetic fields of the NSs in accreting X-ray binaries, however, are found to range from $\sim 10^{12} - 10^{13}\,\mathrm{G}$ (see e.g. Harding & Lai 2006, and references therein), while the magnetic fields of accreting millisecond pulsars reach values of only $B \sim 10^9\,\mathrm{G}$ (e.g. Chakrabarty 2005). An explanation of these findings – which is thought to be due to an evolution of the magnetic field with time – can be found, e.g., in Bhattacharya & Srinivasan (1995), Ruderman (2005), Reisenegger et al. (2005), or Harding & Lai (2006).

The existence of these strong fields has directly visible consequences: at a certain radius (the so called Alfvén radius) the accreted matter is forced to follow the field lines onto the magnetic poles of the NS. If the magnetic axis is not coaligned with the rotational axis of the NS the radiation from the magnetic poles can only be seen by the observer when it crosses his line of sight (like a lighthouse). The observed X-ray flux is therefore modulated with the spin frequency of the NS. However, this frequency is not necessarily constant. As the accreted material carries angular momentum the NS experiences a net torque that alters its rotation period. A more detailed description of this process can be found in chapter 6.2.

Another observational evidence of the strong magnetic fields in NS binary systems is the detection of "cyclotron resonant scattering features" or short "cyclotron lines" in their spectra. While a short introduction to this subject is provided in section 6.3, a very detailed explanation of cyclotron line formation is given for example by Schönherr (2007). Cyclotron lines provide a direct opportunity of measuring the magnetic field strength as the latter is related to the energy of the lines by the so called 12-B12-rule:

$$E_{\mathrm{cyc}} = 11.6\,\mathrm{keV} \cdot B_{12} \tag{1.6}$$

where $B_{12}$ is the magnetic field strength in units of $10^{12}\,\mathrm{G}$. Up to today there are 14 NS binaries known to exhibit cyclotron lines, with four of them showing not only a single feature but also harmonically related lines (Heindl et al. 2004; Kreykenbohm 2004; Psaltis 2006).

Several of the slow rotating accreting NS binaries show in addition to their rotational period also a number of quasi-periodic oscillations with frequencies

[4] An alternative scenario is the dynamo scenario where the magnetic field of the NS is generated by a convective dynamo in the first seconds of the proto-NS (Thompson & Duncan 1993).

ranging from $\sim 1\,\mathrm{mHz}$ to $\sim 40\,\mathrm{Hz}$ (Psaltis 2006). While the oscillations found in the several ten Hz regime can be explained by beat frequency models[5] (Finger 1998; van der Klis 2000) the low frequency oscillations might be related to a low-frequency modulation of the accretion flow for example by the presence of a precessing disk warp (Shirakawa & Lai 2002). In LMXBs with low magnetic field NSs also QPOs with kHz frequencies have been detected which can also be explained in terms of beat frequency models (for an in-depth discussion of this issue see van der Klis 2000, 2006). However, the presence of QPOs always strongly suggests the existence of an accretion disk in a system.

### *1.1.2 Black Hole Binaries*

If the initial mass of a star is large enough, the pressure exerted on the NS by the supernova explosion cannot be compensated by the pressure of the degenerate neutron fluid. The collapse therefore continues to infinity and a Black Hole (BH) forms[6]. To classify an object as BH its mass has to exceed the upper mass limit for NSs which is the so called Oppenheimer-Volkoff mass. Its exact value is unknown as it depends on the still insufficiently known equation of state for nuclear matter (which defines the internal structure of the NS[7]). New results from *XMM-Newton*, however, point at a value of $2.4\,\mathrm{M}_\odot$ (Webb & Barret 2007).

General relativity predicts that BHs – apart from their mass – can have only two other measurable properties, namely angular momentum and charge. The latter would be hardly realized in nature as the electromagnetic force is rather strong and every charged body would neutralize immediately. The size of the BH can be described in the most simple case (that of a non-rotating BH) by the Schwarzschild radius

$$R_\mathrm{S} = \frac{2GM}{c^2} = 3\,\mathrm{km}\left(\frac{M}{\mathrm{M}_\odot}\right) \tag{1.7}$$

and depends only on the mass of the BH. It is important to note that this size does not correspond to a solid surface like in the NS case. The last stable orbit a particle can enter around such a BH is the so called "innermost stable circular orbit" (ISCO) at

$$R_\mathrm{ISCO} = \frac{6GM}{c^2} = 3R_\mathrm{S} \tag{1.8}$$

[5]This means that the frequency of the oscillations corresponds to the beat frequency between the NS spin frequency and the orbital frequency of matter at the Alfvén radius.

[6]The exact masses a main sequence star needs to have to end up as a black hole are not known as there are still large uncertainties in the knowledge of the evolution of massive stars (and especially in modeling the strong mass loss of $M \geq 20\mathrm{M}_\odot$ stars) as well as in the simulation of supernova explosions.

[7]A list of the most realistic equation of states (based on non-relativistic potentials) can be found in Camenzind (2007).

which means that this is also the smallest inner radius the accretion disk can reach.

But how can BH systems be distinguished from NS systems? One secure indicator is surely the mass of the compact object. If this exceeds the Oppenheimer-Volkoff limit the object has to be a BH. A lower limit to the mass is given by the mass function

$$f(M_{\rm o}, M_{\rm X}, i) = \frac{(M_{\rm X} \sin i)^3}{(M_{\rm o} + M_{\rm X})^2} \tag{1.9}$$

with $M_{\rm o}$ being the mass of the optical companion, $M_{\rm X}$ the mass of the compact object and $i$ the inclination of the orbit. However, the exact determination of the mass is difficult or even impossible for many X-ray binaries as the uncertainty in $M_{\rm o}$ can be large and the determination of the inclination is very complex.

Hence there have been numerous suggestions for empirical tests to distinguish between NSs and BHs on basis of their X-ray properties. They include for example a characteristic spectral evolution with increasing average flux (Done & Gierliński 2003) or a significant variability power at high Fourier frequencies, i.e., >100 Hz (Sunyaev & Revnivtsev 2000). In transient systems the properties of the system allow to draw conclusions on the nature of the compact object to some extend as the outbursts of BH transients are typically rarer but longer than those of NS systems. Furthermore, NS transients in quiescence are significantly brighter compared to BH transients (Psaltis 2006). However, apart from the mass the only unequivocal proofs that a compact object is *not* a BH are the presence of signatures of a (strong) magnetic field as persistent pulsations or cyclotron lines or the confirmation of a solid surface through Type I X-ray bursts[8].

At the time of writing there were 20 BH confirmed in X-ray binaries with only three of them (Cyg X-1, LMC X-1, LMC X-3) being persistent sources (Table 1 of Remillard & McClintock 2006). However, there are 5 more candidates which contain very likely a BH due to their X-ray and radio characteristics (Table 4.3 of McClintock & Remillard 2003).

## *1.2 Instrumentation*

The objects described above emit most of their energy in the X-ray and gamma-ray band. The observation of such radiation is not straightforward like when observing in the optical band, for a major drawback is that this radiation does not penetrate down to the ground level. Therefore observing platforms in space or at

[8]The reverse – the absence of such bursts or pulsations or cyclotron lines – does not prove that the compact object *is* a BH! So accreting NSs in LMXB for example are not expected to show pulsations due to their degenerated magnetic field that allows accretion over the whole surface of the NS.

least in the upper layers of the atmosphere such as satellites, rockets, or balloons are needed.

The imaging of the high energy photons is another obstacle that has to be overcome. In a normal reflector telescope the X-rays - and especially the higher energetic $\gamma$-rays - would just be absorbed in the mirror rather than being reflected. This makes the construction of X-ray imaging devices a fairly complicated field. However, there are in principle three different successful approaches on how to build X-ray "telescopes" which are described in the following[9].

### *1.2.1 Collimator Techniques: RXTE*

The simplest way to to get at least something similar to imaging is to reduce the field of view of a detector by simply putting a static collimator in front of it like it is shown in Fig 1.6. Only X-rays from a small region of the sky can reach the detector plane while radiation from outside this region is absorbed. For this technique no position sensitive detector is required. An image is obtained by scanning across the sky with the whole instrument.

The field of view (FOV) is proportional to $d/h$ with $d$ being the width of the detector and $h$ the height of the collimator. Therefore one would need a very large collimator to gain an acceptably small FOV which is impracticable in reality. The solution to this problem is to cover the detector with a set of many short collimators with the same $d/h$ as the one long collimator (see Fig. 1.7). The most common geometries for such collimators are honeycomb structures that provide a great stability. The achievable resolution goes down to about one degree (Bradt 2004) and is restricted at higher energies by penetration of the radiation through and at lower energies by reflection of the radiation off the collimator walls (Kitchin 1984). A possible solution for the high energy photons is to use an active shielding which helps to disregard photons from high inclinations.

The collimator "imaging" technique was used for the *RXTE* satellite that will be briefly described in the following:

The 1995 launched Rossi X-ray Timing Explorer *RXTE* covers in total an energy range from 2–250 keV. Observations in the lower part of this energy band (up to 60 keV [10]) are executed with the Proportional Counter Array (PCA), while the higher energy part (starting at 15 keV) is taken over by the High Energy X-ray Timing Experiment (HEXTE). As mentioned above, the collimator technique makes the use of a position sensitive detector unnecessary, so the PCA consists of five Xenon proportional counter units (*PCUs*) which are co-aligned with an

[9] It is a nice coincidence that this thesis makes use of data from three satellites each using another of those three imaging techniques...

[10] After a voltage change to increase the lifetime of the instrument the nominal higher energy threshold increased to 100 keV.

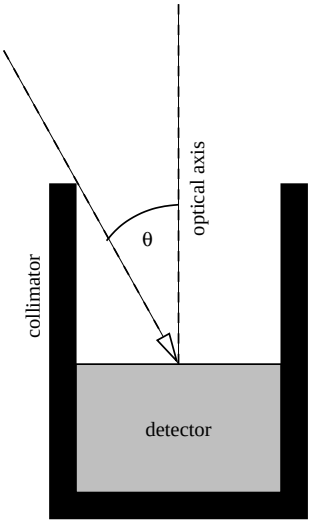


Figure 1.6: Principle of the collimator technique (Figure from lab manual, IAAT).

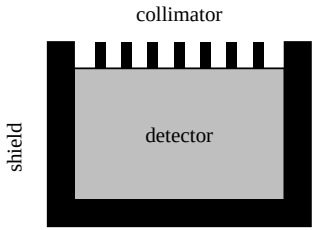


Figure 1.7: Advanced principle of the collimator technique (Figure from lab manual, IAAT).

energy resolution of 18% at 6 keV (Jahoda et al. 1996). HEXTE, which provides an energy resolution of 15% at 60 keV (Rothschild et al. 1998), also uses photon counting detectors, namely two clusters of four NaI(Tl)/CsI(Na)-Phoswich scintillation detectors, respectively. The field of view of both instruments is limited by the collimators to 1 degree. The spacecraft is completed by the All Sky Monitor ASM (Levine et al. 1996) that provides a daily scan of about 80% of the whole X-ray sky in the 2–12 keV band. Fig. 1.8 shows a sketch of the spacecraft with the three instruments. The main instrument characteristics are listed in Table 1.1.

### *1.2.2 Coded Mask Techniques: INTEGRAL*

A more evolved method of imaging is the coded mask technique. It is based on the principle of a pinhole camera, meaning the “light”-rays are not deflected but – in case of the coded mask technology – encoded. The pattern recorded on the detector has therefore to be decoded again to reconstruct the image of the sky. For this is a two-step approach, the coded mask techniques are often referred to as multiplexing techniques. Contrary to the collimator approach, the detector needed in coded mask cameras has to be position sensitive with a spatial resolution sufficient to match the mask-pattern grid size. The mask itself has to consist of

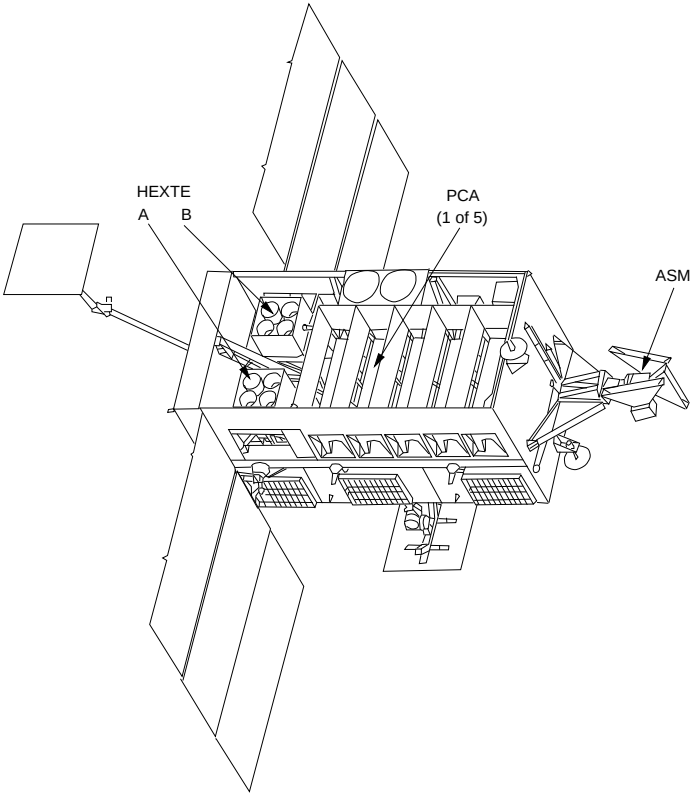


Figure 1.8: The *RXTE* spacecraft. On the left the two HEXTE clusters can be seen, on the right are the five Proportional Counter Units of the PCA. The All Sky Monitor (ASM) is mounted outside the main satellite bus (Figure from Wilms 1998).

transparent and opaque areas which are all equal-sized and arranged in a specific pattern.

Fig. 1.9 shows the working principle of a coded mask camera: photons coming from a specific source (or rather from a specific sky region) project a shadow image of the mask on the detector. Photons that arrive from another direction produce a shifted image of the same pattern with the shift being correspondent to the in-falling direction of the photons. The strength of the pattern recorded by the detector encodes the luminosity of the source (the sky region). To properly decode the image it is necessary that each sky position is encoded in a unique way. This encoding can be achieved by a mask pattern that uses a perfect cyclic

Table 1.1: RXTE instrument characteristics (`http://heasarc.nasa.gov/docs/xte/xhp/xhp_geninfo.html`)

| | PCA | HEXTE | ASM |
|---|---|---|---|
| energy range | 2–60 keV | 15–250 keV | 2–10 keV |
| energy resolution | <18% @ 6keV | 15% @ 60keV | – |
| time resolution | 1 $\mu$s | 8 $\mu$s | 80% of the sky every 90 min |
| spatial resolution | 1° | 1° | $3' \times 15'$ |
| detectors | 5 proportional counters | 2 clusters of 4 scintillation counters | position sensitive proportional counter |
| collecting area | 6500 cm$^2$ | $2 \times 800$cm$^2$ | 90 cm$^2$ |

difference set (Baumert 1971; Gunson & Polychronopulos 1976). Hereby masks with a transparency $f < 50\%$ have a slight signal to noise ratio advantage when the signal is comparable with the detector background (Gunson & Polychronopulos 1976; Fenimore et al. 1979). To gain ideal imaging properties it is furthermore necessary that the recorded shadowgram contains a complete cycle of the basic mask pattern. Therefore two basic telescope geometries can be thought of (Proctor et al. 1979; in 't Zand et al. 1994):

- the detector is larger than the mask (for a two dimensional system the detector has to be four times the area of the mask pattern!)
- the mask is larger than the detector (in this case the basic pattern of the mask has to be repeated several times over, therefore also called "cyclic" configuration)

In most practical applications the choice was made for the cyclic type (due to preservation of collecting area) or to a compromise consisting of the so called "box configuration" in which the mask and the detector are of the same size. The mask contains only one cycle of the basic pattern and therefore only on-axis sources are fully coded, off-axis sources will cause false peaks in the reconstructed image which have to be eliminated in the data-processing (`http://astrophysics.gsfc.nasa.gov/cai/coded_intr.html`).

The cyclic configuration was also realized for *INTEGRAL* which will be described in the following:

The International Gamma-Ray Astrophysics Laboratory (*INTEGRAL*; Winkler et al. 2003) was launched in October 2002. The two main instruments IBIS

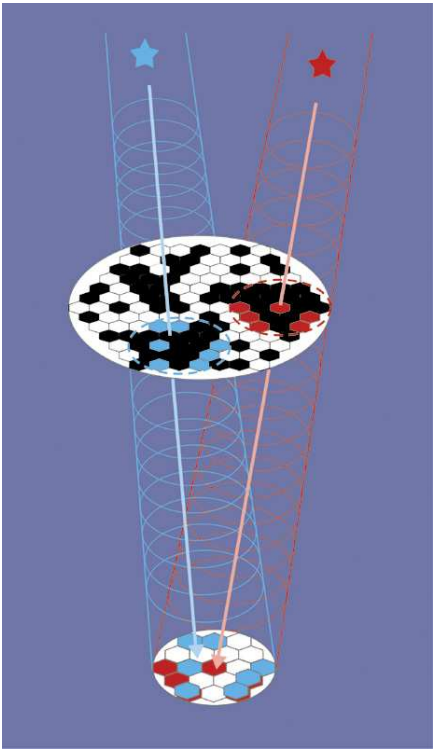

Figure 1.9: The Principle of coded mask imaging: each source produces an unambiguous shadow pattern on the detector. This detector image can afterwards be decoded again to get an image of the sky (Figure from `http://astro.estec.esa.nl/Integral/`).

(15 keV–10 MeV; Ubertini et al. 2003) and SPI (20 keV–8 MeV; Vedrenne et al. 2003) are supplemented in the X-rays by an auxiliary instrument with a smaller field of view, the X-ray monitor JEM-X (3 keV–35 keV; Lund et al. 2003). The Imager on board the *INTEGRAL* Satellite (IBIS) is a coded mask telescope with a fully coded field of view (FCFOV) of $9^\circ \times 9^\circ$ and $12\farcm9$ full width at half maximum (FWHM) angular resolution (Ubertini et al. 2003; Brandt et al. 2003). For this thesis only data from its upper layer, the *INTEGRAL* Soft Gamma-Ray Imager (ISGRI) – a CdTe detector – were used, which covers an energy range from 15 keV–1 MeV with an energy resolution of ~8% at 60 keV (Lebrun et al. 2003; Gros et al. 2003). SPI, the SPectrometer on-board *INTEGRAL*, uses also the coded mask technique. Due to its limited pixel number of only 19 Ge detectors the angular resolution is not very high ($2\fdg5$) but the energy resolution of 2.5 keV at 1.33 MeV is outstanding. The Joint European X-ray Monitor (JEM-X) consists of two identical coded mask instruments with a FCFOV of $4\fdg8$ diameter and $3\farcm35$ angular resolution (FWHM), each (Lund et al. 2003). Due to erosion of the micro-

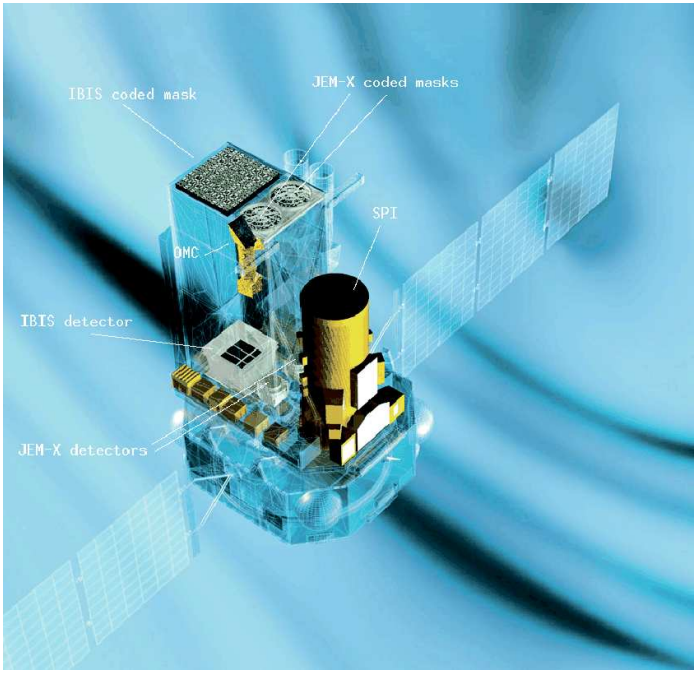


Figure 1.10: The *INTEGRAL* spacecraft with the four instruments (Figure from ESA).

strip anodes inside the JEM-X detectors which leads to a loss in sensitivity, only one of the two JEM-X detectors is operating at any given time while the other is switched off. The main parameters of the three X-ray instruments are summarized in Table 1.2. As shown in Fig. 1.10, *INTEGRAL* also carries an Optical Monitoring Camera (OMC) to extend the observed energy range to the optical band.

### *1.2.3 Wolter Telescopes: XMM-Newton*

Below $\sim 15\,\mathrm{keV}$ it is possible to focus X-rays. This is feasible through grazing incidence reflection. As the index of refraction $n$ for X-rays can be written as[11] $n = (1-\omega_\mathrm{p}^2/\omega^2)^{1/2}$ with $\omega_p \propto Z$ being the electron plasma frequency and $\omega$ being the frequency of the X-rays, Snell's law becomes $\sin\theta_\mathrm{i} = n\sin\theta_\mathrm{r} = (1-\omega_p^2/\omega^2)^{1/2}\sin\theta_\mathrm{r}$. As $n$ is slightly less than unity the X-rays are bent away from the normal. If the incidence angle is larger than the critical value $\sin\theta_\mathrm{crit} =$

[11] Following derivation from `http://web.mit.edu/8.282/www/handouts/xray-ref.pdf`

Table 1.2: *INTEGRAL* instrument characteristics, the optical monitor is not listed (`http://integral.esac.esa.int`)

| | IBIS (ISGRI) | SPI | JEM-X |
|---|---|---|---|
| energy range | 15 keV– 1 MeV | 18 keV– 8 MeV | 3–35 keV |
| energy resolution | 8% @ 100keV<br>10% @ 1MeV | 0.2% @ 1.33MeV | 13% @ 10keV |
| time resolution | 61 $\mu$s | 129 $\mu$s | 122 $\mu$s |
| angular resolution | 12′ FWHM | 2.5° FWHM | 3′ |
| pointing accuracy | 30″ @100 keV (50$\sigma$ src.) | 10′ | $<1'$ (90% confidence) |
| field of view | $9^\circ \times 9^\circ$ (fully coded) | 16° (fully coded) | 4.8° dia. (fully coded) |
| collecting area | 2600 cm$^2$ (ISGRI) | 500 cm$^2$ | $2\times 500$cm$^2$ |

$(1-\omega_p^2/\omega^2)^{1/2}$, respectively if the grazing angle $\beta_{crit} = 90^\circ - \theta_i$ is smaller than the critical value, total internal reflection occurs. A Taylor expansion leads to $\beta_{crit} \approx \omega_p/\omega$, hence the value of $\beta_{crit}$ depends on the frequency of the X-rays as well as on the material used for the mirror. Material with high atomic number Z reflect X-rays more efficiently as low Z materials. Typical values for the grazing incident angles are of the order of 1 degree.

To really use this technique for focusing X-rays in telescopes it is necessary to have a combination of a paraboloidal and hyperboloidal surface (Wolter 1952a,b) as it is shown in Fig. 1.11. A simple parabolic surface is not working because it does not satisfy Abbe's sine condition and therefore only par-axial rays are focused into one point. Another layout that also satisfies the condition would be for example a set of two orthogonal parabolas (Kirkpatrick-Baez design). To increase the effective reflective area it is further necessary to nest several mirrors inside one another, for example for the *XMM-Newton* telescopes 58 mirrors of the classical Wolter I design have been combined.

*XMM-Newton*, the last X-ray satellite to be mentioned here, has been in orbit since 1999. As it uses three co-aligned Wolter Telescopes to focus the X-rays on the detectors, the upper energy threshold is at 15 keV. The angular resolution of the 7.5m focal length telescopes is 6″ (FWHM) in a 30′ field of view. Two of the telescopes are equipped with grating arrays, about 50% of the X-rays passing through this telescopes are intercepted by the grating arrays which form together with their CCD detectors the Reflection Grating Spectrometers (RGS). RGS provides a very high spectral resolution of $E/\Delta E = 200 - 800$ (Ehle et al. 2005).

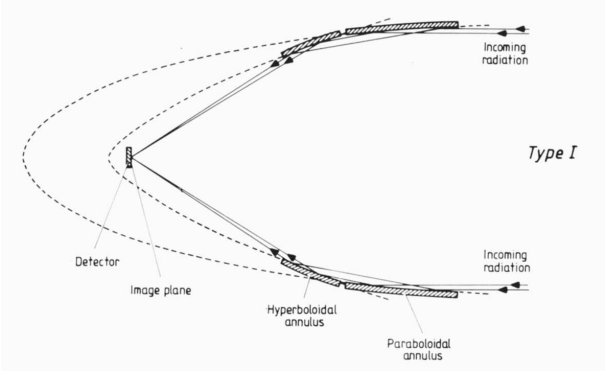


Figure 1.11: The principle of Wolter telescopes: the incoming X-rays are first reflected by a paraboloid and afterwards focused by a hyperboloid (Figure from `http://www.src.le.ac.uk/projects/lobster/ov_optics.htm`).

The other 50% of the infalling X-rays from those two telescopes are focused on the EPIC (European Photon Imaging Camera)-MOS, which consist of two front-illuminated X-ray CCD detectors. The third telescope focuses the X-rays on the EPIC-pn camera, a back-illuminated p-n CCD. The energy resolution of the EPIC CCDs at 1 keV are 70 eV and 80 eV for the MOS and the pn, respectively (Ehle et al. 2005). More details about the MOS can be found in Turner et al. (2001), the pn is described in Strüder et al. (2001). Fig. 1.12 shows an sketch of the *XMM-Newton* payload. Like *INTEGRAL*, *XMM-Newton* carries also an optical monitor that is co-aligned with the X-ray instruments. Table 1.3 lists the main parameters of the X-ray detectors of *XMM-Newton*.

## *1.3 Thesis outline*

The topic of this thesis is the analysis of X-ray observations of the stellar mass black hole system Cygnus X-1 as well as of the neutron star binary 4U 1907+09. Therefore I split the thesis in two parts:

The first part is dedicated to the black hole systems and starts with a short introduction to the relevant radiation processes in these sources in chapter 2. At the end of this chapter the most important Comptonization models used in this work are described. Before reporting the actual results of the broadband analysis (using the Comptonization models as well as a simple phenomenological description of the data by a Broken Power Law), Cyg X-1 is introduced in Chapter 3. Also given

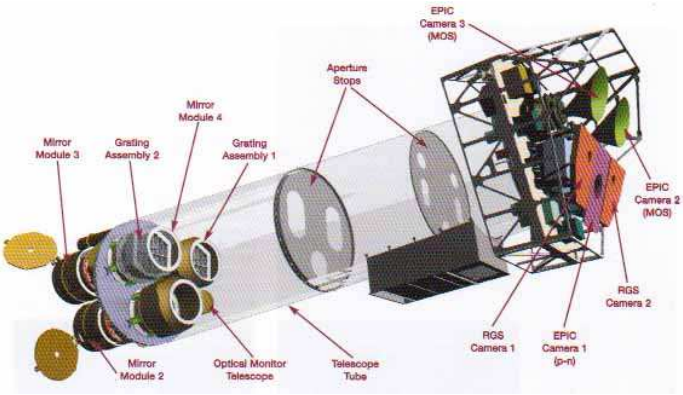


Figure 1.12: The *XMM-Newton* spacecraft with the instruments shown on the right (Figure from `http://www-dapnia.cea.fr/Phocea/Vie_des_labos/Ast/ast_visu.php?id_ast=1397`.

in this chapter is a general description of the states black holes can be found in. Another important point of this thesis is the analysis of the relativistically broadened iron line seen in Cyg X-1. As Cyg X-1 is a very bright source our group had to develop a new observing mode for the *XMM-Newton* EPIC-pn CCD to obtain spectra with the required signal to noise ratio. Chapter 4 summarizes the

Table 1.3: *XMM-Newton* instrument characteristics for the X-ray instruments (Ehle et al. 2005)

| | EPIC-pn | EPIC-MOS | RGS |
|---|---|---|---|
| energy range | 0.15 – 15 keV | 0.15 – 12 keV | 0.35–2.5 keV |
| energy resolution | 7% @ 1keV | 8% @ 1keV | 0.32% @ 1keV (-1. order) |
| | 2.3% @ 6.4keV | 2.3% @ 6.4keV | 0.2% @ 1keV (-2. order) |
| time resolution* | 0.03 ms | 1.5 ms | 16 ms |
| PSF | 6″ FWHM | 5″ FWHM | – |
| | 15″ HEW | 14″ HEW | |
| field of view | 30′ | 30′ | $\sim 5'$ |
| pixel size | 150 $\mu$m (4.1″) | 40 $\mu$m (1.1″) | 81 $\mu$m ($9\times10^{-3}$Å) |

* in fast data acquisition mode (i.e. Timing mode for EPIC, high time resolution mode for RGS)

work which has been been done for the calibration of this new observing mode and describes the physics of relativistically broadened iron lines. The results of the analysis of the iron line region of the spectrum are reported in Chapter 5.

The topic of the second part is the accreting High Mass X-ray Binary system 4U 1907+09. In chapter 6 I first summarize the main observational properties of neutron star binaries like pulse periods and cyclotron lines. 4U 1907+09 is one of the few sources known to show a steady spin-down trend for the last 20 years. Our *INTEGRAL* observations revealed a change in this behavior and show a complete torque reversal. The results of this analysis are presented in chapter 7. I then conclude the thesis with a short summary and an outlook on current and future work on both sources (chapter 8).

# Part I

# Black Hole Binaries: Cygnus X-1

# Chapter 2

# Radiation Processes in Black Hole Systems

As already outlined in the previous chapter, in binary systems the accreted matter cannot fall directly onto the black hole due to its angular momentum. It therefore forms an accretion disk in which it slowly spirals inwards while the angular momentum is transferred outwards. In the vicinity of the accretion disk a corona is formed out of a hot ($\sim 100\,\mathrm{keV}$) electron plasma, although the exact formation process and geometry of this corona are still unknown. Close to the black hole, some fraction of the accreted matter can be ejected outwards at relativistic speeds in a jet. Fig. 2.1 shows the whole scenario for the example of an Active Galactic Nuclei and an X-ray Binary – which show in principle exactly the same accretion scenario, despite the difference of $10^6$–$10^9$ in scale.

The keys for the understanding of the environment around black holes are their spectra and their timing properties. The spectra of black hole systems – a power-law continuum with or without cutoff at higher energies depending on the state – have been explained by multiple Compton scattering of soft photons in a hot medium (Sunyaev & Trümper 1979). As it lies in the nature of the black hole to emit no radiation by itself[1] the contributors to the X- and $\gamma$-ray part of the spectrum are the accretion disk and the corona. The disk dominates the soft X-ray band with a multicolor black body emission (which will be explained in more detail in Section 2.1) providing the photons which are upscattered in the hot corona via inverse Compton scattering up to $\gamma$-ray energies (see Section 2.2). However, the exact geometry of the disk-corona-system is still unclear.

Another feature that is observed in the power-law spectra of black hole systems is a hardening at $\sim 10\,\mathrm{keV}$. This feature can be assigned to Compton reflection of the hard photons off the cold accretion disk (as explained in Section 2.3). This reprocessed hard radiation can again form a significant fraction of the soft seed photons available for Comptonization.

A similar problem occurs when photons are upscattered to energies above ap-

[1] I will not go into details of Hawking radiation or extraction of energy from the black hole due to the presence of magnetic fields in the accretion disk here.

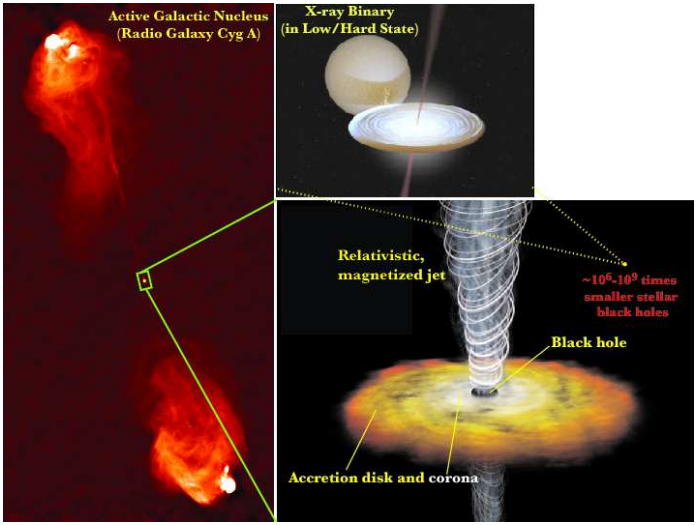


Figure 2.1: *Left panel:* Radio image of the galaxy Cygnus A . *Lower right panel:* Sketch of a zoom into the inner region of Cygnus A with an accretion disk (yellow) and corona (white) as well as a relativistic jet outflow. *Upper right panel:* Sketch of an X-ray Binary which shows the same properties as the innermost regions of Cygnus A but on a $10^6 - 10^9$ times smaller size (Figure courtesy VLA/NRAO).

proximately 510 keV as this is the threshold for $e^{\pm}$ pair production (see Section 2.4). These pairs will then also be part of the Comptonizing medium, so the radiation has direct influence on the optical depth of the plasma - which in turn has produced this radiation.

In this chapter the underlying physics of these processes are explained (for a more thorough illustration see, e.g., Rybicki & Lightman 1979) and in Sections 2.5.1 and 2.5.2 a description of the models which are used to fit the spectra of Cyg X-1 is given.

## *2.1 Black body Radiation*

The spectrum emerging from the relatively cold accretion disk can be described by the superposition of several black body spectra of a certain temperature distribution which happens to be $T(r) \propto r^{-3/4}$ in the case of a simple Shakura-Sunyaev

disk[2] (Shakura & Syunyaev 1973), however, this proportionality does not hold at the inner edge of the disk where advection becomes dominant – here the profile flattens to $T(r) \propto r^{-1/2}$ (see e.g. Watarai et al. 2000). Furthermore black body radiation is of course one of the most fundamental radiation processes as in general every body emits electromagnetic radiation only due to its temperature. To describe this radiation analytically one assumes a perfect absorbing body which emits radiation in all wavelengths. The emitted spectrum depends only on the temperature $T$ of the black body. While it can be described at low frequencies by the Rayleigh-Jeans law

$$B_\nu = \frac{2\nu^2}{c^2} kT \tag{2.1}$$

this solution does not hold for the high frequency part of the spectrum. As can clearly be seen from Eq. 2.1 the intensity $B_\nu$ increases strongly with the frequency (so called "ultraviolet catastrophe"). This behavior is due to the discrete quantum nature of the photons which is not taken into account by the Rayleigh-Jeans law as it is independent of Planck's constant. In the case of high frequencies the spectrum drops exponentially according to Wien's law

$$B_\nu = \frac{2h\nu^3}{c^2} \cdot \exp\left(-\frac{h\nu}{kT}\right) \quad . \tag{2.2}$$

The solution for the whole spectral band was found by Planck at the end of the 19th century when he discovered the concept of the quantization of light and is given by

$$B_\nu = \frac{2h\nu^3}{c^2} \cdot \frac{1}{\exp\left(-\frac{h\nu}{kT}\right) - 1} \quad . \tag{2.3}$$

Planck's law comprises both the Rayleigh-Jeans law and Wien's law as asymptotic solutions (see Fig. 2.2). The derivative with respect to the frequency $\nu$ shows that the frequency, at which the maximum of the black body radiation is emitted, increases linearly with temperature

$$\nu_{\max} = 2.82\frac{kT}{h} \approx 5.88 \cdot 10^{10}\,\mathrm{Hz}\left(\frac{T}{1\mathrm{K}}\right) \quad . \tag{2.4}$$

Fig. 2.3 shows this Wien displacement law for several different black body temperatures.

[2]The temperature profile $r^{-3/4}$ is also realized in the `diskbb` model used later (Mitsuda et al. 1984; Makishima et al. 1986).

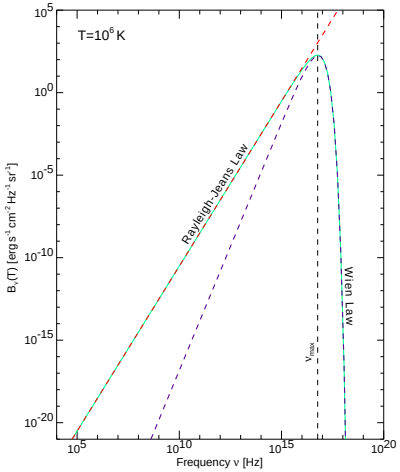


Figure 2.2: Spectrum of black body radiation with the asymptotic solutions of Rayleigh-Jeans and Wien (Wilms 2001).

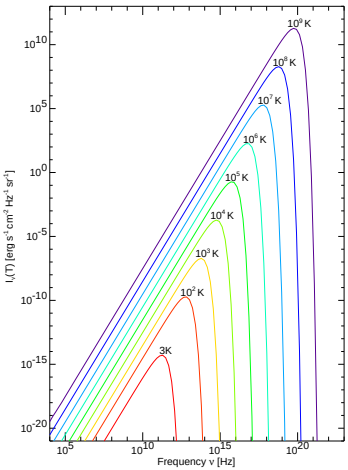


Figure 2.3: Wien's displacement law: the emitted radiation maximum increases with temperature to higher frequencies (Wilms 2001).

## 2.2 Comptonization

After emerging from the relatively cool accretion disk the soft black body photons are up-scattered to energies of several 100 keV in the hot corona via inverse Compton scattering.

In the original process of Compton scattering a photon is scattered off a stationary electron, thereby decreasing its energy from E to

$$E_1 = \frac{E}{1 + \frac{E}{m_e c^2}(1 - \cos\theta)} \tag{2.5}$$

as it transfers kinetic energy to the electron. $\theta$ is the angle between the old and the new direction of the photon as can be seen in Fig. 2.4. As was shown by Klein & Nishina (1929) the differential cross section for this process is given by

$$\frac{\mathrm{d}\sigma_{\mathrm{es}}}{\mathrm{d}\Omega} = \frac{3}{16\pi}\sigma_{\mathrm{T}}\left(\frac{E_1}{E}\right)^2\left(\frac{E}{E_1} + \frac{E_1}{E} - \sin\theta^2\right) \tag{2.6}$$

with $\sigma_{\mathrm{T}} = \frac{8\pi}{3}r_0^2 = 6.652\times10^{-25}\,\mathrm{cm}^2$ being the Thomson cross section. Substituting $x = E/mc^2$ and integrating equation 2.6 over all scattering angles leads to the

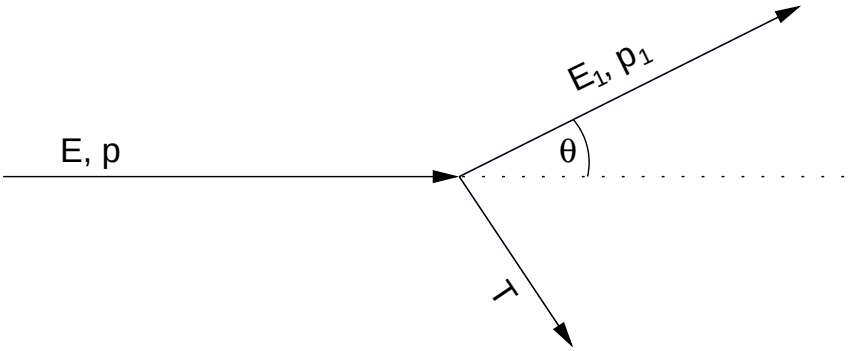


Figure 2.4: Compton scattering (Wilms 1998)

Klein-Nishina formula describing the total cross section (Rybicki & Lightman 1979; Longair 1992):

$$\sigma_{\rm es} = \sigma_{\rm T}\frac{3}{4}\left[\frac{1+x}{x^3}\left(\frac{2x(1+x)}{1+2x} - \ln 1+2x\right) + \frac{1}{2x}\ln 1+2x - \frac{1+3x}{(1+2x)^2}\right] \tag{2.7}$$

Note that this cross section still describes the scattering process for a stationary electron. The electrons in the corona of a black hole are not stationary at all such that the reverse process of the one described above is at work: during the scattering process net energy is transferred from the electron to the photon. This process is called *inverse Compton scattering*.

To calculate the average fractional energy change per scattering, the corona is assumed to be thermal in most approaches, i.e., the electrons have a Maxwellian distribution. This distribution can be characterized by its temperature $T_{\rm e}$. If this temperature is small compared to the rest mass energy of the electrons, the average relative energy change for a photon undergoing the inverse Compton scattering process is given by (Rybicki & Lightman 1979)

$$\frac{\Delta E}{E} = \frac{4kT_{\rm e} - E}{m_{\rm e}c^2} \tag{2.8}$$

The photons gain energy from this process as long as the electron temperature is high enough. Thereby the electron plasma is cooled very efficiently. For $E > 4kT_{\rm e}$ the situation changes again and energy is transferred from the photons to the electrons.

When a photon is traversing a medium it will undergo several scattering events. To determine if the photon significantly changes its energy due to these scatterings

one can define the so-called Compton *y* parameter (Rybicki & Lightman 1979)

$$y = \left(\text{average fractional energy change per scattering}\right) \times \left(\text{mean number of scatterings}\right) \tag{2.9}$$

When $y > 1$ the photon undergoes a significant energy change while for $y \ll 1$ the initial energy is not not changed much.

The mean number of scatterings for regions of large optical depth ($\tau \gg 1$) is approximately given by the square of the optical depth $N \approx \tau^2$. In the case of small optical depth media the mean number of scatterings is of order $1 - e^{-\tau}$ and therefore small compared to the optical thick case. So for $\tau \ll 1$ the average number of scatterings can be approximated by $N \approx \tau$ (Rybicki & Lightman 1979). Combining these two limits with the average fractional energy change per scattering (Eq. 2.8), it is possible to obtain an analytical expression for the Compton *y* as defined in "equation" 2.9:

$$y = \frac{4kT_\mathrm{e}}{m_\mathrm{e}c^2} \max(\tau, \tau^2) \quad . \tag{2.10}$$

The calculation of the emerging spectra after multiple scatterings is a non-trivial problem as the energy change $\Delta E$ depends on the energy $E$ of the photon itself. For the simplified case of non-relativistic electrons with a thermal energy distribution the time-dependent spectral distribution of the Comptonized photons is given by the Kompaneets equation (Rybicki & Lightman 1979)

$$\frac{\partial n}{\partial t_c} = \left(\frac{kT_e}{m_e c^2}\right) \frac{1}{x^2} \frac{\partial}{\partial x} \left[ x^4 \left( n + n^2 + \frac{\partial n}{\partial x} \right) \right] \tag{2.11}$$

with $x = \hbar\omega / kT$ and $t_c$ being the time measured in units of the mean time between two scatterings. To solve the Kompaneets equation mainly Monte Carlo approaches are used as analytical solutions are hard or even impossible to find. A more detailed description of these Monte Carlo simulations as well as example spectra can be found in Wilms (1998).

## 2.3 Compton Reflection

Contrary to the corona, the electrons in the disk are rather cold, such that according to Eq. 2.8 hard photons can not gain energy in the scattering process but lose energy and get softer. Fig. 2.5 shows the effective cross section for Compton scattering per H atom and the cross section for photo ionization $\sigma_\mathrm{bf}$. Due to $\sigma_\mathrm{bf} \propto E^{-3}$ photo absorption is way more important than Compton scattering for energies below ~15 keV while for energies much larger than 15 keV the photons

will Compton scatter and thereby lose energy. These high energy photons will undergo scattering processes until their energy is low enough to be photo absorbed or until they leave the plasma. In the spectrum this processes can be seen as a broad hump with its maximum around 30 keV (Lightman & White 1988).

The mathematical description of this process can be done in the Green's functions formalism. If one sets $x = E/m_e c^2$ and $\mu = \cos\theta$ with $\theta$ being the angle between the line of sight and the disk normal, the reflected spectrum can be written as

$$I_{\mathrm{ref}}(x;\mu) = \int_0^\infty G_{\mathrm{ref}}(\mu, x, x_0) I_{\mathrm{inc}}(x_0) \mathrm{d}x_0 \quad . \tag{2.12}$$

As the analytical derivation of $G$ is very difficult there have been mainly solutions using Monte Carlo methods, for example by White et al. (1988, angle averaged Green's functions). Important in the scope of this thesis is the method of Magdziarz & Zdziarski (1995) which is used in the *XSPEC* model `reflect`, as these authors give analytical angle dependent Green's functions. This model was used to describe the reflection component in the spectra of Cyg X-1.

In black hole Binaries the incident X-ray radiation is so intense that it determines the ionization state of the disk matter (Ross & Fabian 1993, 2005, and references therein). This ionized reflection leads to an additional bump in the soft (0.2–2 keV) X-ray spectrum due to bremsstrahlung and line emission from the hot surface layers which can be described by an 150 eV black body component.

Another signature of reflection is the presence of an iron fluorescence line in the observed spectra. As said above the incident photons from the corona are energetic enough to ionize the atoms in the accretion disk. If the expelled electron originates from an inner orbital of the atom, the "hole" can be filled by an electron from an outer shell. This transition of an electron leads to the emission of radiation with a characteristic frequency (namely the difference between the two orbitals involved) which yields an emission line in the spectrum[3]. The exact energy of the emission line depends on the ionization stage of the element, as the bond energy of the inner atomic shells is shifted towards higher energies with increasing ionization.

A more in depth explanation of Compton reflection and related processes can be found in Wilms (1996), a more detailed description of the iron line in black hole systems is given in chapter 4.

[3]The emitted photon might also deposit its energy to eject another electron from an outer shell of the atom (Auger effect). In this case the ejected electron becomes part of the disk plasma and the atom is left behind double ionized. Another way to fill the "hole" in the inner shell is the capture of a free electron from the plasma (free-bound transition).

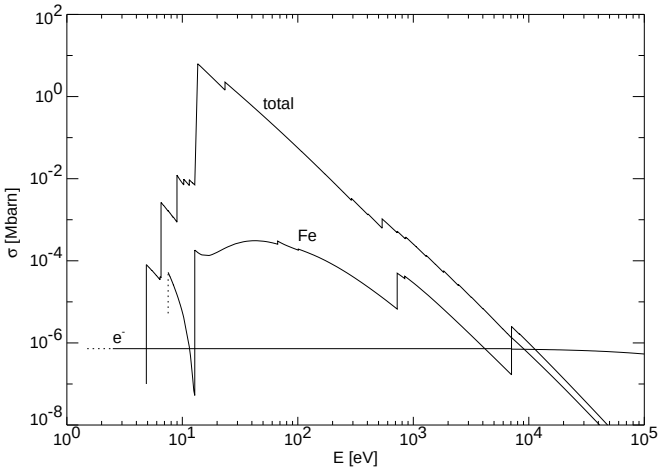


Figure 2.5: From top to bottom: total cross section for photo absorption per hydrogen atom, contribution of Fe total cross section, and Klein-Nishina cross section. All cross section computed for a gas with solar abundances (Figure from Wilms 1998).

## 2.4 Pair production

Electron-positron pairs can in principle be produced by the following four processes if the center of mass energy of the particles exceeds $E = 2m_e c^2$=1.022 MeV:

$$\gamma + \gamma \longrightarrow e^+ + e^- \tag{2.13}$$

$$\gamma + e^- \longrightarrow e^- + e^- + e^+ \tag{2.14}$$

$$e^- + p \longrightarrow e^- + p + e^- + e^+ \tag{2.15}$$

$$e^- + e^- \longrightarrow e^- + e^- + e^- + e^+ \tag{2.16}$$

The first of those four processes is referred to as photon-photon pair production. It is the most important pair production process as Svensson (1982) showed that the pair production rate of Eq. 2.13 is more than one order of magnitude larger than the production rate of the second process and even three orders of magnitude larger than those of the other two processes mentioned.

The cross section of photon-photon pair production is given by (Akhiezer & Berestetskii 1965; Berestetzki et al. 1989)

$$\sigma_{\gamma\gamma} = \frac{\pi r_0^2}{x^2}\left[\left(2 + \frac{2}{x^2} - \frac{1}{x^4}\right)\ln\left(x + \sqrt{x^2-1}\right) - \sqrt{1 - \frac{1}{x^2}}\left(1 + \frac{1}{x^2}\right)\right] \tag{2.17}$$

with $x = E/m_e c^2$ being the center of mass energy of the photons.

Of similar importance is the inverse process which is called pair annihilation:

$$e^+ + e^- \longrightarrow \gamma + \gamma \tag{2.18}$$

The cross section

$$\sigma_{e^+e^-} = \pi r_0^2 \left( \frac{1-\beta_{CM}^2}{4\beta_{CM}} \right) \left[ \frac{3-\beta_{CM}^4}{\beta_{CM}} \ln\left( \frac{1+\beta_{CM}}{1-\beta_{CM}} \right) + 2(\beta_{CM}^2 - 2) \right] \tag{2.19}$$

(Berestetzki et al. 1989) of this process is highest at small center of mass velocities $\beta_{CM}$ of the $e^-$ and tends to be zero as the velocity reaches high values. This behavior is due to the decreasing interaction timescale between the pairs with increasing velocities.

Pair production is the limiting factor of the minimum total optical depth and therefore the maximum possible temperature of the coronal plasma around a BH (Haardt & Maraschi 1991, 1993; Malzac & Jourdain 1998). This maximum temperature is independent of the seed opacity of the corona (which does not take into account the contribution of the pairs). Models which are pair-dominated reach the maximum temperature with a much lower coronal compactness parameter[4] for a given total opacity than non-pair-dominated models (Dove et al. 1997).

## *2.5 Models*

To describe the observed broadband continuum spectra of black holes models are needed which treat all of the basic physical processes ongoing in the systems simultaneously, as most of the radiation processes described above interact directly. Within the X-ray fitting package *XSPEC* there are various implementations of so-called "Comptonization spectra" as for example the Comptonized black body model `compbb` (Nishimura et al. 1986), the `compps` model of Poutanen & Svensson (1996), the Monte Carlo based model `kotelp` (Dove et al. 1997), the `compst`/`compTT` models by Sunyaev & Titarchuk (1980) and Titarchuk (1994) respectively, or the thermal/non-thermal plasma model `eqpair` (Coppi 1992, 1999). The latter two will be described in more detail in the following as they have been used in this thesis to model the broadband spectrum of Cyg X-1.

[4] Dove et al. (1997) define the local coronal compactness parameter for a slab geometry as $l_c = \sigma_T/(m_e c^3) z_0 \Psi_c$ with $\sigma_T$ being the Thomson cross section, $m_e$ the electron mass, $z_0$ the scale height of the corona, and $\Psi_c$ the rate of energy dissipation per unit area into the corona.

### 2.5.1 The XSPEC model compTT

compTT (Titarchuk 1994; Titarchuk & Lyubarskij 1995; Titarchuk & Hua 1995) is an analytical model for the description of Comptonized spectra from a soft Wien law input spectrum. The approximations made in this model are chosen in a way that it works for the optically thin and thick regimes equally well. compTT includes relativistic effects and is an extension of the compst model (Sunyaev & Titarchuk 1980).

In a certain range of plasma temperatures and geometry parameters the emergent spectra depend only on the two parameters $kT$ (which is the plasma temperature) and $\beta$, which defines the photon distribution over the number of scatterings the soft photons pass through before leaving the plasma (Hua & Titarchuk 1995). The parameter $\beta$ is no direct input parameter in the *XSPEC* implementation but the way it is calculated can be determined by the *approx* parameter of compTT [5]. The optical depth $\tau$ is then calculated as a function of $\beta$. One drawback of compTT is that it is not valid for simultaneously high optical depth and high plasma temperature or low optical depth and low temperature (see also Fig. 7 of Hua & Titarchuk, 1995, for the range of valid parameters).

### 2.5.2 The XSPEC model eqpair

The main advantage of eqpair (Coppi 1992) compared to other Comptonization models (especially to the previously described compTT) is its ability of treating hybrid thermal/non-thermal pair plasmas instead of purely thermal ones. A specified seed photon distribution (which might be according to the diskbb or the diskpn model) is Comptonized in a spherical plasma cloud by thermal electrons (with Maxwellian distribution) as well as by non-thermal electrons (with a power-law distribution). The temperature of the medium is calculated by balancing Compton cooling with external heating. Therefore eqpair treats all micro physics self-consistently and without any significant approximations. It includes Compton scattering (with all Klein-Nishina corrections), $p - e^{\pm}$ and $e^{\pm} - e^{\pm}$ thermal and non-thermal bremsstrahlung, and $e^{\pm}$ pair production and annihilation. The energy exchange between the non-thermal and thermal part of the plasma occurs through Coulomb scattering (Coppi 1992, 1999; Gierliński et al. 1999). The properties of the Comptonizing plasma are specified by the dimensionless compactness param-

[5] The sign of this parameter defines the approximation technique with values $\geq 0$ leading to an analytic approximation of $\beta$ from $\tau$ while $\beta$ is interpolated from a set of calculated pairs of $\beta$ and $\tau$ for values $<0$. The magnitude of this parameter switches between the disk ($\leq 1$) and sphere ($>1$) geometry. This parameter has to be frozen (in the case of this thesis it was frozen to 1).

eter $\ell$, which in case of the `eqpair` model is defined as

$$\ell = \frac{L\sigma_{\mathrm{T}}}{rm_{\mathrm{e}}c^3} \tag{2.20}$$

where $L$ is the source luminosity, $\sigma_{\mathrm{T}}$ the Thomson cross section, and $r$ the radius of the Comptonizing medium. It defines the power which is supplied to the different components in the plasma, e.g., $\ell_{\mathrm{s}}$ is the power supplied in form of the soft seed photons and $\ell_{\mathrm{h}}$ is the power supplied to the electrons ($\ell_{\mathrm{h}}$ is further split into direct electron heating $\ell_{\mathrm{th}}$ and electron acceleration $\ell_{\mathrm{nth}}$ with $\ell_{\mathrm{h}} = \ell_{\mathrm{th}} + \ell_{\mathrm{nth}}$). `eqpair` also takes relativistic line smearing and ionized Compton reflection into account as after the Comptonization a fraction of the photons is scattered back and reflected off the disk.

The main parameters (in the scope of this thesis) of the `eqpair` model are[6]

- the **hard to soft compactness** $\ell_{\mathrm{h}}/\ell_{\mathrm{s}}$, which gives the ratio of the power supplied to the accelerated electrons/pairs to the luminosity of the soft photons which enter the source region. Therefore $\ell_{\mathrm{h}}/\ell_{\mathrm{s}}$ defines the overall hardness of the upscattered photon spectrum.
- the **soft compactness** $\ell_{\mathrm{s}}$, which describes the importance of photon-photon pair production, as for values $\gg 1$ the source is optically thick for gamma rays and therefore pair production is very important and the dominant cooling process is Compton cooling. If $\ell_{\mathrm{s}} \ll 1$ the main cooling mechanism changes to Coulomb and bremsstrahlung cooling and the spectrum gets distorted at lower energies.
- the **temperature of the disk black body** $T_{\mathrm{bb}}$, giving the opportunity to distinguish between two different incident photon distributions as `eqpair` will use a multicolor disk black body like `diskbb` (Mitsuda et al. 1984; Makishima et al. 1986) when the parameter value is positive whereas it will use the pseudo-Newtonian disk-model `diskpn` [7] (Gierliński et al. 1999) when the parameter value is negative.
- $\ell_{\mathrm{nth}}/\ell_{\mathrm{h}}$, the **non-thermal to hard compactness ratio**, describing the fraction of the total power that is supplied to the non-thermal acceleration of the electrons
- the **Thomson scattering depth** $\tau_{\mathrm{p}}$ from the ionized electrons in the background plasma of the scattering region. In case of a purely thermal model with no pair production these electrons produce a thermal Comptonization

[6] adapted from `http://www.astro.yale.edu/coppi/eqpair/eqpap4.ps`

[7] The main difference between the `diskbb` and the `diskpn` model is the torque-free boundary condition assumed in `diskpn`, which yields a more accurate description of the temperature distribution in the innermost part of the accretion disk. `diskpn` also allows the calculation of an accretion rate from the derived temperature.

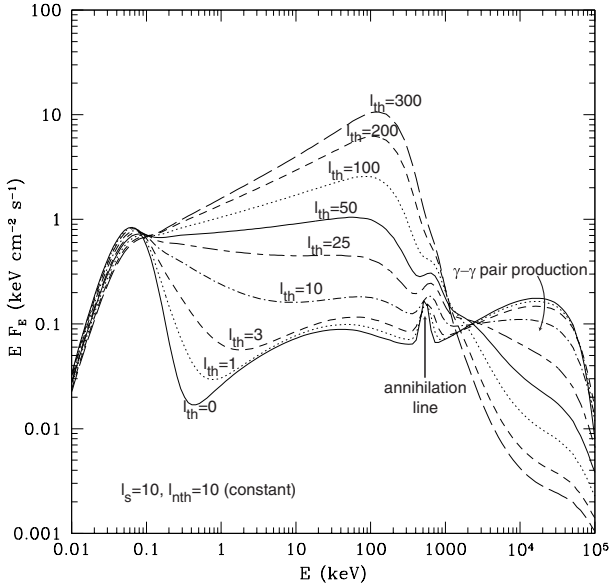


Figure 2.6: Differences between a thermally dominated ($\ell_{\rm th}$=300) and a non-thermal ($\ell_{\rm th}$=0) plasma. The other parameters of this model are $\tau_{\rm p}$=0.1, $R = 10^{14}$ cm, and $T_{\rm bb}$=15 eV (Coppi 1999).

spectrum with optical depth $\tau_{\rm T} = \tau_{\rm p}$, in case of pair production the Thomson optical depth will be $\geq \tau_{\rm p}$.

- the **fraction of the scattering region's emission that is intercepted by reflecting material** $R = \Omega_{\rm ref}/2\pi$, with $\Omega_{\rm ref}$ being the solid angle subtended by the reflector as viewed from the scattering region. This parameter is normalized to 1 for isotropic emission over an infinite slab.
- the **ionization parameter** $\xi$ of the reflector, which should be set to $\xi = 4\pi F_{\rm ion}/n$ (with $n$ being the density of the reflecting material and $F_{\rm ion}$ the 0.005–20 keV ionizing flux seen by the reflector).

Apart from these parameters there are several other parameters that could be modeled with `eqpair` such as the power law injection index for the accelerated electrons/pairs, the physical size of the scattering region, the inclination of the reflecting material, or the inner and outer radius of the reflecting material. Furthermore it is possible to distinguish between a pure electron and a pair plasma via the *pairinj* parameter.

Although `eqpair` is more elaborated than `compTT`, the latter one was also used

in this thesis to describe the broadband spectrum of Cyg X-1. This decision is motivated on the one hand by its speed in fitting the data (as compared to, e.g., `eqpair`) and on the other hand by its large historical success which allows comparison with earlier fits. The results of the accordant fits can be found in sections 3.4.2 (`compTT`) and 3.4.3 (`eqpair`).

# Chapter 3

# The broadband spectrum of Cygnus X-1

Being one of the first X-ray sources discovered, Cygnus X-1 has also become one of the best studied. This is mainly due to its persistent nature (as already mentioned only three out of the known 20 black hole systems are persistent, with Cyg X-1 being the brightest of the three by far) that makes it an ideal target for almost all X-ray missions. However, Cyg X-1 has not only been studied in the X-rays, the broadband coverage ranges from radio data (e.g., Stirling et al. 1998, 2001; Gallo et al. 2005; Fender et al. 2006) up to a detection in the TeV range with the MAGIC telescope (Albert et al. 2007).

In this chapter a short introduction to the Cygnus X-1 system is given, followed by an overview of the spectral states of BHs in general (section 3.2). After this paragraph the observations analyzed in this chapter of the thesis are described. Section 3.4 focuses on the results of the analysis of the broadband spectrum.

## *3.1 The Cygnus X-1 system*

Cygnus X-1 was discovered in 1964 during a rocket flight (Bowyer et al. 1965) and is nowadays known to have a distance of 2.5 kpc (Ninkov et al. 1987). The system consists of a compact object orbiting the O9.7 Iab supergiant HDE 226868 which was found to have a mass of $17.8\,M_{\odot}$ and a radius of approximately $17\,R_{\odot}$ (Herrero et al. 1995). Therefore this system ranks among the High Mass X-ray Binary systems. HDE 226868 drives a strong wind with a mass loss rate of $\approx 3\times10^{-6}\,M_{\odot}\,a^{-1}$, out of which 0.01–0.1% are accreted onto the compact object (Herrero et al. 1995). As HDE 226868 almost fills its Roche lobe, the wind is focused and strongly asymmetric with a mass loss rate of 4.5 times the minimum value towards the compact object (Friend & Castor 1982; Gies & Bolton 1986; Gies et al. 2003; Vrtilek et al. 2007).

The mass values quoted for the compact object in Cygnus X-1 differ signifi-

cantly: while Ziółkowski (2005) found $20 \pm 5\,M_\odot$ using evolutionary models[1], the most recent mass value for Cyg X-1 is $8.7 \pm 0.8\,M_\odot$ (Shaposhnikov & Titarchuk 2007). Previous to those relatively new mass determinations the most common value found in literature was $10\,M_\odot$ (Herrero et al. 1995). Even though these values are not consistent, they all lie well above the Oppenheimer-Volkoff limit for neutron star masses, so the object can be classified as black hole unequivocally.

The main source of uncertainty in mass determination arises from the still debated orbital inclination of the system. The inclination has been determined via optical polarization measurements (making use of the fact that HDE 226868 is not a sphere any more because it almost fills its Roche lobe) to lie in the range between 26° and 67° (see, e.g., Bochkarev et al. 1986; Ninkov et al. 1987; Dolan 1992). More recently, Abubekerov et al. (2004) used the orbital variability of the absorption line profiles of HDE 226868 to refine this range to $31° < i < 44°$.

The orbital period of $\sim 5.6$ d of the system can be deduced from radial velocity measurements (Gies & Bolton 1982; Brocksopp et al. 1999b). It is also visible in the soft X-ray flux as the X-ray emission due to the accretion onto the BH is photo absorbed in the focused accretion stream at the superior conjunction of the system (e.g., Kitamoto et al. 1984; Bałucińska-Church et al. 1997; Brocksopp et al. 1999a). Besides the orbital period there is also a super-orbital period of roughly 150 d reported which is attributed to the precession of the accretion disk[2] (Brocksopp et al. 1999a; Pooley et al. 1999; Benlloch et al. 2004; Lachowicz et al. 2006; Ibragimov et al. 2007).

Of course the overview given here makes no claim to be complete. More in depth reviews of the system as well as compilations of the system parameters are given, e.g., by Oda (1977), Liang & Nolan (1984), and Pottschmidt (2002). The most interesting system parameters are summarized in Table 3.1.

Fig 3.1 (Gierliński et al. 1999) shows three spectra of Cyg X-1 observed in the years 1991 (hard state) and 1996 (intermediate and soft state). This changing of spectral appearance is a typical behavior of BHs and will be the subject of the following section.

## *3.2 The states of black holes*

Depending on the dominant source of radiation – disk or corona – black hole systems can be observed in different spectral states as shown in Fig. 3.1 for the case of Cyg X-1. But not only the spectral shape changes, also the timing properties

[1] Ziółkowski (2005) also finds a significantly higher value for the mass of HDE 226868, which according to his calculations lies in the range 29–50 $M_\odot$.

[2] More about this issue can be found in section 5.2.1.1

Table 3.1: System parameters of the Cygnus X-1 binary system.

| | Cyg X-1 | HDE 226868 | references |
|---|---|---|---|
| **stellar parameters** | | | |
| Luminosity [$L_\odot$] | $10^4$ | $10^{5.4}$ | Herrero et al. (1995); Liang & Nolan (1984) |
| Luminosity [$erg\,s^{-1}$] | $4 \cdot 10^{37}$ | $10^{39}$ | |
| Mass Function [$M_\odot$] | 0.252(10) | | Gies & Bolton (1982) |
| Mass [$M_\odot$] | 8.7(8) | 17.8 | Shaposhnikov & Titarchuk (2007); Herrero et al. (1995) |
| Radius | 30 km | 17 $R_\odot$ | Herrero et al. (1995) |
| Mass loss rate [$M_\odot a^{-1}$] | | $3 \times 10^{-6}$ | Herrero et al. (1995) |
| Wind velocity [$km\,s^{-1}$] | | 2100 | Herrero et al. (1995) |
| spectral type | | O9.7 Iab | Walborn (1973) |
| $T_{\rm eff}$ [K] | | 32 000 | Herrero et al. (1995) |
| **orbital parameters** | | | |
| orbital period [d] | 5.59974(8) | | Gies & Bolton (1982) |
| $a \sin i$ [km] | $5.82(8) \times 10^6$ | | Gies & Bolton (1982) |
| inclination | $31° < i < 44°$ | | Abubekerov et al. (2004) |
| $v \sin i$ [$km\,s^{-1}$] | | 75.6(10) | Gies & Bolton (1982) |
| **position** | | | |
| J2000.0: $\alpha$, $\delta$ | $19^h58^m21\overset{s}{.}700$, $+35°12'05\overset{''}{.}82$ | | Turon et al. (1992) |
| galactic: $l_{II}$, $b_{II}$ | $71\overset{\circ}{.}33$, $+3\overset{\circ}{.}07$ | | Turon et al. (1992) |
| Distance [ kpc] | 2.5(3) | | Ninkov et al. (1987) |

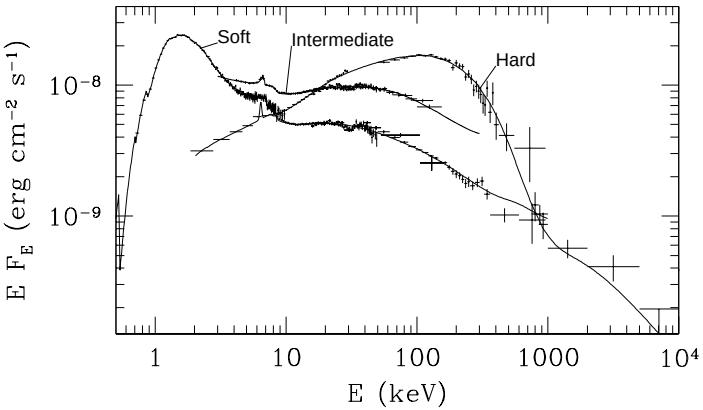


Figure 3.1: The states of black hole binaries as seen in Cyg X-1 (Gierliński et al. 1999).

and the luminosity of the systems show different behavior. Most black hole systems undergo transitions between the states which are associated with a change in the accretion geometry. While there has been a classification in only two clearly defined states, namely the Hard/Low and High/Soft state (with a Intermediate and Quiescent state to complete the picture) that lasted for years, the increasing knowledge of the high energy emission of black hole systems has recently led to a more detailed re-definition of the states. I will concentrate in the following on the classification proposed by Belloni (2005), however, there have been other attempts for a re-definition of the states, e.g., by McClintock & Remillard (2006).

The classification of Belloni (2005) comprises four basic states: Hard, Hard Intermediate, Soft Intermediate, and Soft that are based on the presence of sharp state transitions. In addition to those four states is the Quiescent state. The basic characteristics of the four states are:

Low/Hard state (LS):

- relatively low values of accretion rate
- hard energy spectrum
- fast time variability dominated by strong band-limited noise (∼30% fractional rms)
- sometimes low frequency QPOs
- characteristic frequencies in power spectra follow broad-range correlations (see Belloni et al. 2002)
- compact jet ejection, observable as flat-spectrum radio emission (see Gallo et al. 2003; Fender et al. 2004)

Hard Intermediate state (HIMS):

- energy spectrum softer than in LS with evidence for soft thermal disk component
- power spectra show band-limited noise with characteristic frequency higher than in the LS
- usually rather strong 0.1–15 Hz type-C QPO[3] (Casella et al. 2005)
- slightly steeper radio spectrum

Soft Intermediate state (SIMS):

- energy spectrum systematically softer than in the HIMS
- flux dominated by disk component
- no strong band-limited noise in the power spectrum
- transient type-A and type-B QPOs with limited frequency range
- no core radio emission

High/Soft state (HS):

- very soft energy spectrum, strongly dominated by thermal disk component
- only weak power-law noise in the power spectrum
- no core radio emission (Fender et al. 1999; Fender 2006)

The physical picture that underlies this classification is as follows: The thermal thin accretion disk is the dominant emission component in the HS as well as in the SIMS. The innermost radius of this disk is small (probably coincident with the innermost stable orbit) in the HS and increases to larger values in the HIMS and LS, in which the disk temperature is in most cases too low to be observable (Frontera et al. 2001b; McClintock et al. 2001). The dominant radiation process in the LS is thermal Comptonization from $\sim$100 keV electrons. This component is responsible for the power-law continuum with high energy cutoff shape of the spectrum as well as for the strong band-limited noise observed in the power spectrum. As this thermal Comptonization component is not observed in the HS, Markoff et al. (2003) proposed that it originates directly from the jet. In the HS and HIMS instead a third component is present in the spectrum that could be modeled by a steep power law. This component originates from non-thermal Comptonization. There are indications that this component might also be present in the SIMS. So the high energy part of the spectrum shows an evolution from thermal Comptonization in the LS, over the HIMS with both components present to a non-thermal Comptonization in the HS.

[3]Type-C QPOs are defined by variable, narrow ($\Delta\nu/\nu \sim 7-12$), strong (up to $\sim$ 16% rms) peak that is superposed on a flat-top noise, often there are also a subharmonic and a second peak present. The flat-top noise steepens above a frequency that is comparable to the QPO frequency. The QPO rms increases with energy until $\sim$ 10 keV where it flattens. Phase lags are strongly dependend on the frequency of the QPO (Casella et al. 2005, and references therein).

Fig. 3.2 summarizes the state transition scenario for the example of a transient source: in the center a hardness-intensity diagram (HID) is shown, the intensity increases upwards and the hardness from the left to the right. The black hole system starts (in the bottom right corner) in the Hard state at a low luminosity but with a hard spectral shape. In this stage a jet is present. As the outburst goes on the source moves up in the HID to higher luminosities but keeping the hardness. At a certain point the luminosity does not increase any more and the source moves horizontal through the Hard Intermediate state towards the Soft Intermediate state. The spectrum gets softer but the jet persists until the system approaches the so called "jet line". Shortly before this point the jet is most powerful and has the highest Lorenz factor, which leads to the formation of an internal shock. After the black hole system has crossed the jet line, the jet disappears. The source is now in the Soft Intermediate state or even in the Soft state where the spectrum is dominated by the soft disk emission. Some sources perform repeated excursions back towards the jet line. Most sources, however, show a decreasing luminosity with remaining hardness (now in the Soft state) and afterwards a horizontal transition back to the Hard state.

As mentioned above, Fig. 3.2 shows the example of a transient source which undergoes huge luminosity variations. Cygnus X-1 is a persistent source and therefore shows no such dramatic luminosity changes. In fact Cyg X-1 is established in the upper region of the diagram as pointed out by Wilms et al. (2007). "Historically" Cygnus X-1 was found most of the time in the hard state, which can be quantified for the time of the *RXTE* monitoring campaign[4] in the way that 90% of the observations up to MJD 51300 were hard state observations, 4% soft state observations and 6% were in between. However, this behavior changed after MJD 51300 with the soft and intermediate state intervals increasing since then to 34% of the observations (Wilms et al. 2006). The reason of this change in behavior might be related to changes in the mass loss rate of HDE 226868 (Gies et al. 2003).

## *3.3 Observations and data reduction*

The observations analyzed in this thesis were executed in 2004 when Cyg X-1 was observed simultaneously by *INTEGRAL*, *RXTE*, and *XMM-Newton* on November 14/15 (hereafter called obs1), 20/21 (obs2), 26/27 (obs3), and December 2/3 (obs4). The total observation time was ∼320 ksec for the *INTEGRAL* observation, ∼152 ksec for *RXTE*, and ∼40 ksec for *XMM-Newton*. Tables 3.2 (*INTEGRAL*) and 3.3 (*RXTE*) summarize the observations and give details about the effective

[4]The values quoted here span the range from 1996–2004 as given in (Wilms et al. 2006).

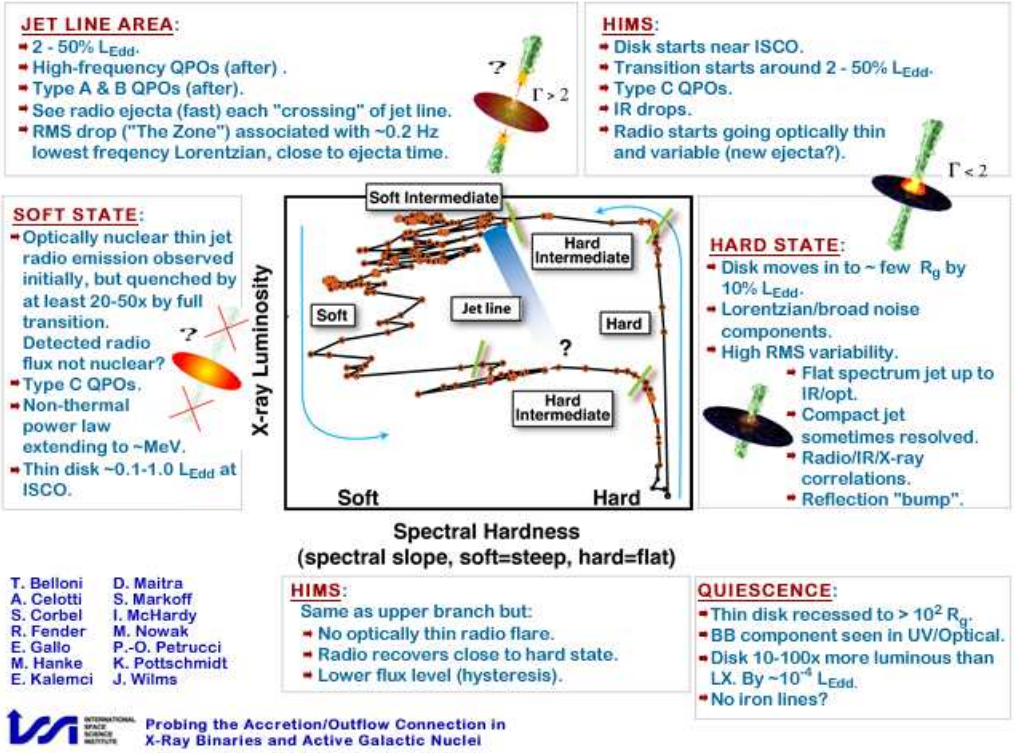


Figure 3.2: Jet-disk coupling and state transitions (Figure courtesy of ISSI team on black holes 2008, `http://www.sternwarte.uni-erlangen.de/proaccretion/`).

Table 3.2: Observational parameters for the *INTEGRAL* observations

| | | Effective Exposure | | |
|---|---|---|---|---|
| Observation | Date (MJD) | IBIS (ks) | SPI (ks) | Jem-X (ks) |
| obs1 | 53323.297 – 53324.260 | 56.072 | 22.310* | 77.611 |
| obs2 | 53329.459 – 53330.422 | 56.176 | 62.037 | 79.540 |
| obs3 | 53335.748 – 53336.731 | 55.459 | 62.170 | 76.907 |
| obs4 | 53341.674 – 53342.674 | 56.896 | 50.954 | 82.930 |

* this low exposure is due to 18 pointings marked bad for SPI by the Saclay team

Table 3.3: Observational parameters for the *RXTE* observations

| | | Effective Exposure | |
|---|---|---|---|
| Observation | Date (MJD) | PCA (ks) | HEXTE (ks) |
| obs1 | 53323.474 – 53324.219 | 12.432 | 12.820 |
| obs2 | 53329.905 – 53330.321 | 16.704 | 12.750 |
| obs3 | 53335.878 – 53336.244 | 16.000 | 10.871 |
| obs4 | 53341.862 – 53342.256 | 15.648 | 10.837 |

observation time per instrument. For the details of the *XMM-Newton* observations see chapter 5.1 in which the analysis of the iron line is described. Fig. 3.3 shows the *RXTE*/ASM light curve of Cyg X-1 with the four observations indicated by vertical bars. As one can already see from this light curve, Cyg X-1 was highly variable during the observations, indicating that the source was observed in none of the canonical hard or soft states.

The *INTEGRAL* data were extracted using the standard Offline Scientific Analysis (OSA) version 6 and comprises information of the three instruments JEM-X, IBIS (ISGRI), and SPI, including energies up to 1 MeV. The creation of the SPI catalog was done setting the minimum flux of the catalog extraction task to $0.001\,\mathrm{photons\,cm^{-2}\,s^{-1}}$. For the extraction of the IBIS (ISGRI) and JEM-X data we took the presence of two other sources in the field of view into account, namely EXO 2030+375 and Cyg X-3. The presence of the transient source 3A 1954+319 in some of our observations has no influence on the spectrum obtained, so it was not included in the final extraction catalog. We applied systematic uncertainties of 3% for IBIS (ISGRI) and 5% for JEM-X [5].

[5] There is no official guideline on how much systematics should be used for OSA 6. However, as the official cross calibration report provided for OSA 5.1 (Lubiński et al. 2005) recommends 5% for IBIS (ISGRI) data taken after revolution 255, 3% seem to be appropriate for OSA 6. For JEM-X we stick to the 5% quoted in the report as there have been no major calibration improvements between OSA 5.1 and OSA 6.

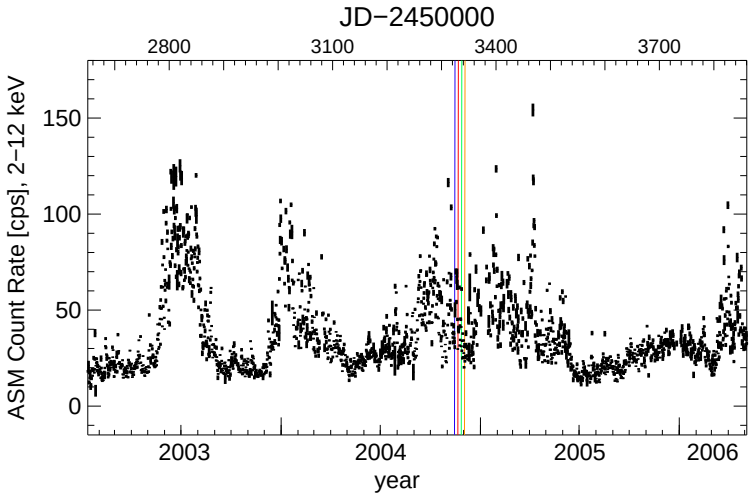


Figure 3.3: *RXTE* ASM light curve of Cyg X-1. The vertical lines mark the times of our observations (blue: obs1, red: obs2, green: obs3, yellow: obs4).

For *RXTE* we used data from the PCA and HEXTE, covering an energy range from 3 keV to 120 keV. The data extraction was done using HEASOFT 5.3.1. We only used data for which the source was at elevations higher than 10° and the time elapsed since the last passing of the South Atlantic Anomaly (SAA) was greater than 10 minutes. For the PCA we applied systematic errors of 0.5%.

Fig. 3.4 shows the light curves of all our observations. The binning is 40 s and all four observations are plotted in the same count rate range to achieve comparability. Taking only *RXTE* and *INTEGRAL* into account, obs1 had on average the lowest count rate and least fluctuations, while obs3 was the brightest observation of the four. The strongest "activity" is seen in obs2 which shows the highest variation coefficient as can be seen in Table 3.4. For *XMM-Newton* the picture is different: here obs2 is the smoothest one with the smallest variation coefficient as well as the lowest count rate. This effect is due to the shorter observing time in *XMM-Newton* which ends just before Cyg X-1 starts to become brighter.

## *3.4 Comparison with the long term monitoring campaign*

Despite the complexity of the underlying radiation processes (as described in Chapter 2) there are in principle two different approaches to model the broadband

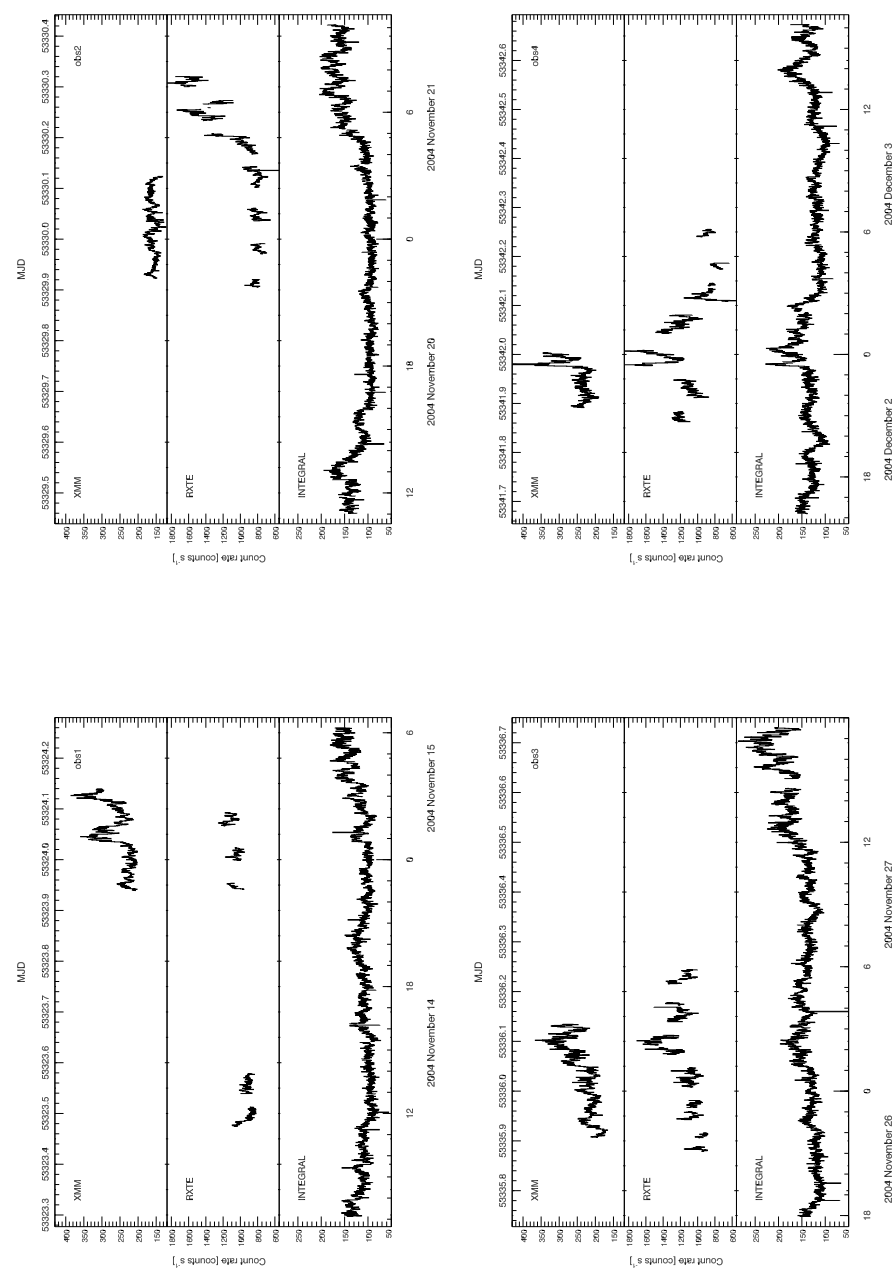


Figure 3.4: Light curves of the four observations (bin time: 40 s).

Table 3.4: Some statistical properties of the light curves.

| | obs1 | obs2 | obs3 | obs4 |
|---|---|---|---|---|
| ***XMM-Newton*** | | | | |
| mean [cts s$^{-1}$] | 254 | 160 | 235 | 249 |
| standard deviation [cts s$^{-1}$] | 41 | 12 | 39 | 42 |
| variation coefficient | 0.16 | 0.07 | 0.16 | 0.16 |
| ***RXTE*** | | | | |
| mean [cts s$^{-1}$] | 993 | 1015 | 1158 | 1102 |
| standard deviation [cts s$^{-1}$] | 104 | 296 | 163 | 229 |
| variation coefficient | 0.10 | 0.29 | 0.14 | 0.21 |
| ***INTEGRAL*** | | | | |
| mean [cts s$^{-1}$] | 113 | 120 | 148 | 131 |
| standard deviation [cts s$^{-1}$] | 18 | 30 | 31 | 22 |
| variation coefficient | 0.16 | 0.25 | 0.21 | 0.17 |

continuum spectra of BHs. The first one is a simple phenomenological description of the data by a broken power law with an exponential cutoff. In most cases (and especially for Cyg X-1) it is necessary to add a Gaussian line to describe the iron K$\alpha$ emission[6] and a component to account for the photoabsorption.

The second approach is more physically motivated and makes use of Comptonization models which treat all of the basic physical processes ongoing in the system. Two of them – `compTT` and `eqpair`– have already been described in sections 2.5.1 and 2.5.2.

The first aim of our analysis was to check if the parameters found to model the 3–120 keV energy range covered by the long term *RXTE* monitoring campaign (Wilms et al. 2006, and references therein) could also fit the data up to 1 MeV. Therefore we first fitted our data with the same three models (broken power law, `compTT`, and `eqpair`) used by these authors. The fits were done for all four observations individually.

### *3.4.1 Broken power law Fits*

The first model we applied to our data was a broken power law with an exponential cutoff. This model is known to describe the spectra of BHs phenomenologically

[6]The iron line itself needs a more in-depth consideration as it is skewed and broadened by relativistic effects. In Chapter 4 the theory as well as the analysis of the iron line in Cyg X-1 are described.

(Nowak et al. 2005):

$$C(E) = \left\{ \begin{array}{ll} K \cdot (E/1\,\mathrm{keV})^{-\Gamma_1} & \text{for } E < E_{\mathrm{break}} \\ K \cdot E_{\mathrm{break}}^{\Gamma_2-\Gamma_1} \cdot (E/1\,\mathrm{keV})^{-\Gamma_2} & \text{for } E > E_{\mathrm{break}} \end{array} \right\} \times \exp((E_{\mathrm{cut}} - E)/E_{\mathrm{fold}}) \tag{3.1}$$

In addition to this continuum we fitted the Fe K$\alpha$ line as a Gaussian centered at ~6.4 keV and the photoabsorption was modeled using the *XSPEC* model `phabs` (Bałucińska-Church & McCammon 1992; Verner & Yakovlev 1995).

The best fit parameters are $\Gamma_1 \approx 2.0$, $E_{\mathrm{break}} \approx 10$ keV, $\Gamma_2 \approx 1.6$, and a folding energy ranging from 121 keV (obs1) to 146 keV (obs3). The iron line was found to have a width $\sigma$ around 0.5 keV indicating the presence of a broadened line. It is noticeable that the broken power law fits can reproduce the spectrum equally well as the more complex `eqpair` model, the $\chi^2_{\mathrm{red}}$ values obtained range from 1.78 (obs3) to 1.35 (obs4).

Fig. 3.5 shows the strong linear correlation found between the soft power law index $\Gamma_1$ and the hard power law index $\Gamma_2$ in the *RXTE* monitoring campaign. This correlation is especially interesting, as it shows the hardening of the underlying continuum due to Compton reflection. All *RXTE* monitoring observations with $\Gamma_1$<2.1 are defined as hard state observations (Wilms et al. 2006). A comparison of our results (colored symbols in Fig. 3.5) with the results of the monitoring campaign shows that the values found for $\Gamma_1$ and $\Gamma_2$ agree very well with the strong linear correlation. Also the other parameters found for the extended energy range agree well with the previous results, for example the iron line is almost consistent with 6.4 keV as in the majority of the monitoring campaign fits. Another example for the consistence is the cutoff energy $E_{\mathrm{cut}}$ of the exponential cutoff which was found between 15 and 40 keV in the *RXTE* campaign and lies between 22 and 26 keV in our fits.

### *3.4.2 `compTT` Fits*

`compTT` is the first Comptonization model we used. For the soft emission we added a `diskbb` component which provides the seed photons for the Comptonization. We set the temperature of the seed photons equal to $kT_{\mathrm{in}}$, the temperature at the inner edge of the disk. This continuum is partly reflected off the accretion disk. To model this reflection we use the *XSPEC* model `reflect` (Magdziarz & Zdziarski 1995) with the inclination of the disk assumed to be 40°. We also took the presence of interstellar absorption into account and modeled the iron line again as a Gaussian. The position of the line, however, could not be constrained by the data, so we fixed it to 6.40 keV.

The parameters derived from these fits are consistent with earlier results like it was the case for the broken power law fits. The values for the electron temperature

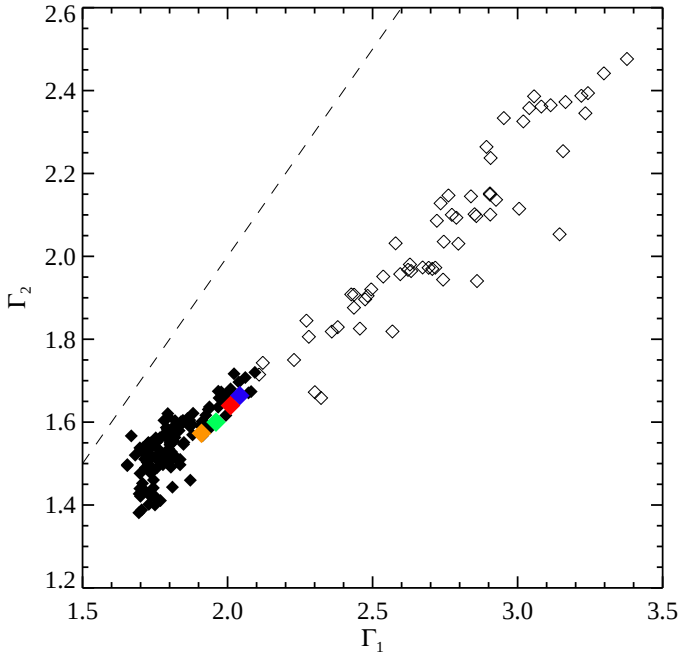


Figure 3.5: Correlation between the soft power law index $\Gamma_1$ and the hard power law index $\Gamma_2$. The filled symbols mark hard state observations (defined by $\Gamma_1$<2.1) from the *RXTE* monitoring campaign, the open ones are soft and intermediate state observations (also from the *RXTE* monitoring campaign), and the colored symbols show the values obtained in this analysis.

of the plasma $kT_e$ – which lie in the range between 51 keV and 70 keV– and the optical depth $\tau$ (which ranges from 0.64 to 0.92) lead to a Compton $y$ parameter $y = 4kT_e/m_ec^2 \max\left(\tau, \tau^2\right) \approx 0.37 \pm 0.07$. This value differs from $y = 0.5$ found in the *RXTE* monitoring data for about 70% of the observations (with virtually all of them being hard state observations). This deviation is indicative for the transitional or intermediate state of the source. Furthermore the values for the reflection covering factor are higher than in previous hard state results, which is also consistent with the conclusion that Cyg X-1 was observed in a transitional/intermediate state (see also Fig. 3.6).

The $\chi^2_{\rm red}$ values we obtained from the `compTT` fits are very similar to those we achieve by using the phenomenological model, they range from 1.75 (obs3)

Table 3.5: Best fit parameters for the broken power law fits.

| | **obs1** | **obs2** | **obs3** | **obs4** |
|---|---|---|---|---|
| $N_{\rm H}[10^{22}{\rm cm}^{-2}]$ | $0.16^{+0.50}_{-0.16}$ | $0.75^{+0.47}_{-0.49}$ | $0.47^{+0.43}_{-0.47}$ | $0.63^{+0.48}_{-0.54}$ |
| $E_{{\rm K}\alpha}$ [keV ] | $6.34^{+0.09}_{-0.08}$ | $6.29^{+0.10}_{-0.11}$ | $6.28^{+0.10}_{-0.11}$ | $6.27^{+0.11}_{-0.13}$ |
| $\sigma_{{\rm K}\alpha}$ [keV ] | $0.57^{+0.11}_{-0.12}$ | $0.53^{+0.14}_{-0.14}$ | $0.48^{+0.16}_{-0.15}$ | $0.52^{+0.16}_{-0.16}$ |
| ${\rm norm}_{\rm line}$ $[10^{-3}]$ | $16^{+3}_{-3}$ | $13^{+4}_{-3}$ | $13^{+4}_{-3}$ | $13^{+5}_{-3}$ |
| $\Gamma_1$ | $2.04^{+0.04}_{-0.02}$ | $2.01^{+0.03}_{-0.04}$ | $1.96^{+0.03}_{-0.04}$ | $1.91^{+0.03}_{-0.04}$ |
| $E_{\rm break}$ | $10.14^{+0.20}_{-0.19}$ | $10.02^{+0.18}_{-0.20}$ | $10.00^{+0.19}_{-0.19}$ | $10.02^{+0.20}_{-0.22}$ |
| $\Gamma_2$ | $1.66^{+0.01}_{-0.01}$ | $1.64^{+0.01}_{-0.01}$ | $1.60^{+0.08}_{-0.09}$ | $1.57^{+0.01}_{-0.01}$ |
| $K$ | $3.59^{+0.32}_{-0.14}$ | $3.53^{+0.30}_{-0.30}$ | $3.51^{+0.27}_{-0.29}$ | $3.30^{+0.28}_{-0.31}$ |
| $E_{\rm cut}$ | $22^{+1}_{-1}$ | $24^{+1}_{-1}$ | $26^{+1}_{-1}$ | $24^{+1}_{-1}$ |
| $E_{\rm fold}$ | $121^{+3}_{-3}$ | $136^{+3}_{-3}$ | $143^{+3}_{-3}$ | $146^{+4}_{-3}$ |
| $A_{\rm HEXTE}$ | $1.173^{+0.004}_{-0.004}$ | $1.070^{+0.004}_{-0.003}$ | $1.037^{+0.003}_{-0.003}$ | $1.012^{+0.003}_{-0.003}$ |
| $A_{\rm ISGRI}$ | $1.05^{+0.01}_{-0.01}$ | $0.94^{+0.01}_{-0.01}$ | $0.96^{+0.01}_{-0.01}$ | $0.85^{+0.01}_{-0.01}$ |
| $A_{\rm JEM\text{-}X}$ | $1.12^{+0.01}_{-0.01}$ | $1.01^{+0.01}_{-0.01}$ | $1.062^{+0.009}_{-0.009}$ | $0.918^{+0.009}_{-0.008}$ |
| $A_{\rm SPI}$ | $1.36^{+0.01}_{-0.01}$ | $1.14^{+0.01}_{-0.01}$ | $1.18^{+0.01}_{-0.01}$ | $1.02^{+0.01}_{-0.01}$ |
| $\chi^2_{\rm red}$ / dof | 1.418/251 | 1.371/243 | 1.775/268 | 1.352/258 |

to 1.41 (obs2 and obs4) although the `compTT` model describes the data by really calculating the physical processes in the system while the broken power law is only an empirical description.

### *3.4.3 `eqpair` Fits*

The last model we used in this first analysis is the hybrid thermal/non-thermal Comptonization code `eqpair`. Unlike the `compTT` model the temperature of the Comptonizing medium is computed self-consistently in `eqpair`. The seed photon distribution is again defined by a disk black body, the model to be used in `eqpair` was chosen to be pseudo-Newtonian (`diskpn`), whereas the soft excess was mod-

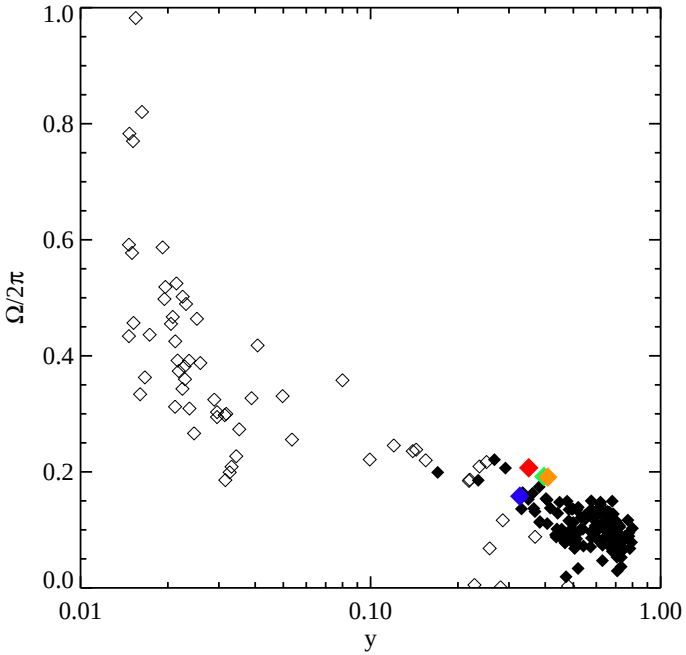


Figure 3.6: Correlation between the Compton y parameter and the covering factor for the reflection $\Omega/2\pi$.

eled by an additional `diskbb` model. This choice mimics the shape of (saturated) Comptonization better than the `diskpn` model and therefore works better (more details can be found in Wilms et al. 2006, and references therein). The plasma was assumed to be purely thermal by fixing the non-thermal to hard compactness ratio $\ell_{\rm nth}/\ell_{\rm h}$ to 0.001 and the soft compactness was kept to a value of $\ell_{\rm s}$=1 as in Wilms et al. (2006)[7]. The photoabsorption and the Fe K$\alpha$ line are treated as in the models described above.

The parameters describing the hard spectral component, namely the compactness ratio $\ell_{\rm h}/\ell_{\rm s}$ and the optical depth $\tau$, are in good agreement with the previous results. Fig.3.7 shows that our values for the compactness ratio also go very well with the correlations found between this parameter and the parameters of the bro-

[7]The value of $\ell_{\rm s}$=10 quoted in Wilms et al. (2006) is a typo, however changing this value to 10 makes almost no difference in the obtained parameters (in fact only the 4th decimal place of $\ell_{\rm h}/\ell_{\rm s}$ changes).

Table 3.6: Best fit parameters for the `compTT` model.

| | **obs1** | **obs2** | **obs3** | **obs4** |
|---|---|---|---|---|
| $N_{\rm H}[10^{22}{\rm cm}^{-2}]$ | $4^{+2}_{-2}$ | $0^{+0.6}_{-0}$ | $0^{+0.2}_{-0}$ | $0^{+0.4}_{-0}$ |
| $E_{{\rm K}\alpha}$ [keV] | 6.40 (fixed) | 6.40 (fixed) | 6.40 (fixed) | 6.40 (fixed) |
| $\sigma$ [keV] | $1.18^{+0.12}_{-0.08}$ | $0.71^{+0.15}_{-0.08}$ | $0.71^{+0.12}_{-0.08}$ | $0.64^{+0.13}_{-0.12}$ |
| ${\rm norm}_{\rm line}$ $[10^{-3}]$ | $45^{+12}_{-13}$ | $22^{+4}_{-3}$ | $17^{+4}_{-3}$ | $17^{+3}_{-3}$ |
| $kT_{\rm in}$ [keV] | $0.72^{+0.06}_{-0.04}$ | $0.92^{+0.03}_{-0.05}$ | $0.95^{+0.04}_{-0.05}$ | $0.94^{+0.04}_{-0.04}$ |
| ${\rm norm}_{\rm bb}$ | $2602^{+2917}_{-1478}$ | $330^{+134}_{-49}$ | $322^{+66}_{-48}$ | $305^{+83}_{-43}$ |
| $kT$ [keV] | $51^{+6}_{-4}$ | $70^{+16}_{-9}$ | $55^{+4}_{-4}$ | $62^{+9}_{-6}$ |
| $\tau_p$ | $0.82^{+0.08}_{-0.08}$ | $0.64^{+0.12}_{-0.15}$ | $0.92^{+0.08}_{-0.07}$ | $0.84^{+0.10}_{-0.13}$ |
| ${\rm norm}_{\texttt{compTT}}$ $[10^{-3}]$ | $35^{+4}_{-5}$ | $22^{+4}_{-10}$ | $30^{+3}_{-2}$ | $29^{+3}_{4}$ |
| $\Omega/2\pi$ | $0.16^{+0.02}_{-0.02}$ | $0.21^{+0.01}_{-0.01}$ | $0.19^{+0.01}_{-0.01}$ | $0.19^{+0.01}_{-0.01}$ |
| $A_{\rm HEXTE}$ | $1.168^{+0.004}_{-0.004}$ | $1.062^{+0.010}_{-0.004}$ | $1.028^{+0.004}_{-0.004}$ | $1.004^{+0.003}_{-0.003}$ |
| $A_{\rm ISGRI}$ | $1.05^{+0.01}_{-0.01}$ | $0.93^{+0.01}_{-0.01}$ | $0.95^{+0.01}_{-0.01}$ | $0.84^{+0.01}_{-0.01}$ |
| $A_{\rm JEM\text{-}X}$ | $1.11^{+0.01}_{-0.01}$ | $1.01^{+0.01}_{-0.01}$ | $1.08^{+0.01}_{-0.01}$ | $0.92^{+0.01}_{-0.01}$ |
| $A_{\rm SPI}$ | $1.35^{+0.01}_{-0.01}$ | $1.13^{+0.01}_{-0.01}$ | $1.17^{+0.01}_{-0.01}$ | $1.01^{+0.01}_{-0.01}$ |
| $\chi^2_{\rm red}$ / dof | 1.574 / 252 | 1.414 / 244 | 1.753 / 252 | 1.412 / 263 |

ken power law fits in the *RXTE* monitoring.

The reflection covering factor of the `compTT` fits is found around 0.2 while it is around 0.3 in the `eqpair` fits. The same behavior was also found in the *RXTE* monitoring with exactly the same difference of $\sim 0.1$ between the two $\Omega/2\pi$ values. This difference is most probably due to the fact that – contrary to the `compTT` fits – relativistic smearing of the reflection component is taken into account in the `eqpair` model. As already indicated in Fig. 3.6 for the `compTT` fits, the absolute values of $\Omega/2\pi$ are found on the upper limit compared to observations from the monitoring with similar shape of the Comptonized continuum. Due to the same $\Delta\Omega/2\pi$ the according behavior can be seen in the `eqpair` fits (Fig. 3.8) where it

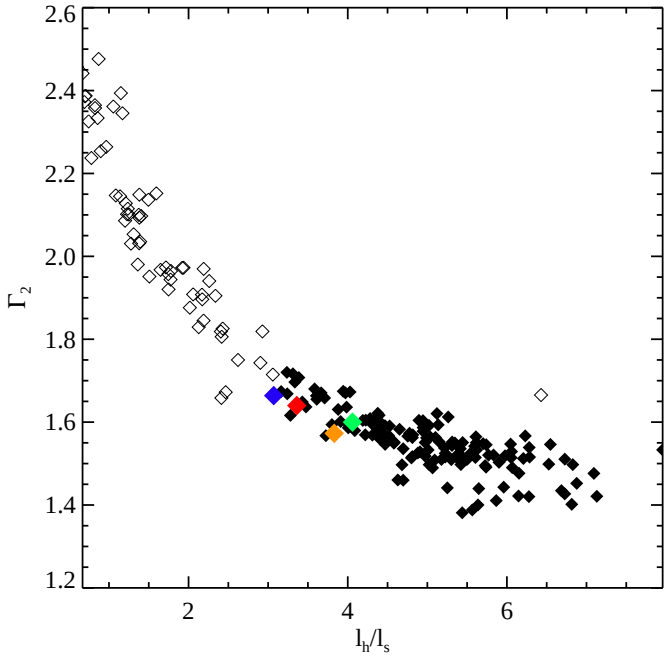


Figure 3.7: Relationship between $\Gamma_2$ and the compactness ratio $\ell_h/\ell_s$ of the Comptonizing medium.

is even more pronounced.

### *3.4.4 Time averaged broad band spectra*

The `eqpair` fits described in the previous section showed slight indications of a spectral hardening above $\sim 300$ keV which could be a sign for the presence of a non-thermal electron component in the plasma. We therefore decided to sum up a time averaged spectrum comprising all observations in order to get better statistics for SPI in the crucial energy range although Cyg X-1 was highly variable during our observations.

Again we first considered a pure thermal plasma and fixed $\ell_s = 1$. The disk parameters we obtain are $T_{in} = 1.15^{+0.02}_{-0.03}$ keV, and a normalization of $37^{+3}_{-3}$. This latter value is significantly lower than the values we got by analyzing the four observations independently which is due to the increased statistics that allow a better determination of the disk parameters. The compactness ($\ell_h/\ell_s = 3.28^{+0.01}_{-0.02}$), the op-

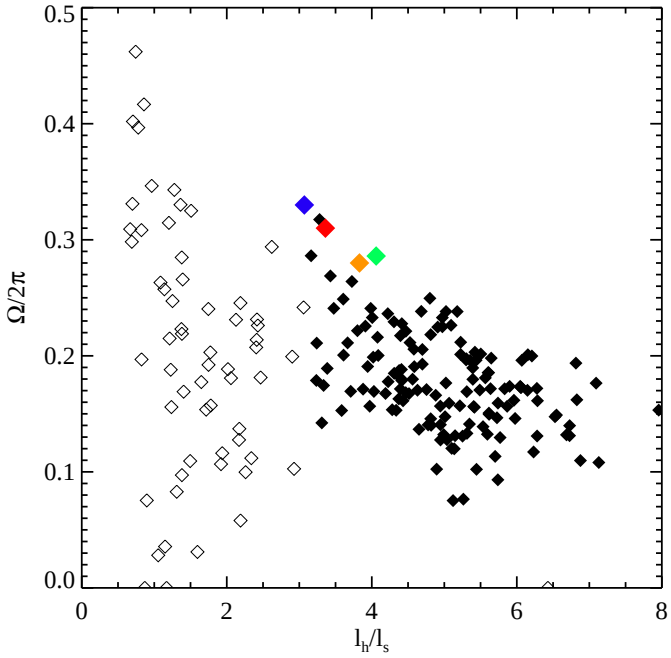


Figure 3.8: Relationship between the reflection covering factor $\Omega/2\pi$ and the compactness ratio $\ell_h/\ell_s$.

tical depth ($\tau = 1.24^{+0.01}_{-0.02}$), and the reflection covering factor ($\Omega/2\pi = 0.299^{+0.004}_{-0.006}$) are consistent with our previous results. Also the iron line parameters match the values obtained before. The $\chi^2_{\rm red}$ yields a value of 1.66 for 324 dof. The deviation between the data points and this pure thermal model is clearly visible above 300 keV in the time averaged spectrum (Fig. 3.9, top). To exclude instrumental effects we also extracted the SPI data with different energy binnings and different background models, however, the deviation remained visible in all our fits.

Therefore we added a non-thermal component in the `eqpair` model by allowing the parameter $\ell_{\rm nth}/\ell_{\rm h}$ to vary (see lower panel of Fig. 3.9). We found that 67% of the power supplied to the electrons in the plasma is used for the non-thermal acceleration of the electrons ($\ell_{\rm nth}/\ell_{\rm h} = 0.67$). This additional component improves the $\chi^2_{\rm red}$ to 1.39 (323 dof). The dimensionless parameter $\ell_{\rm h}/\ell_{\rm s}$ increases to $4.74^{+0.02}_{-0.03}$, the optical depth $\tau = 1.420^{+0.008}_{-0.007}$, and the reflection covering factor

Table 3.7: Best fit parameters for the `eqpair` model.

| | **obs1** | **obs2** | **obs3** | **obs4** |
|---|---|---|---|---|
| $N_{\rm H}$ [$10^{22}$cm$^{-2}$] | $1.12^{+0.39}_{-0.44}$ | $0.53^{+0.08}_{-0.12}$ | $0.01^{+0.12}_{-0.01}$ | $0^{+0.22}_{-0}$ |
| $E_{{\rm K}\alpha}$ [keV] | $6.23^{+0.08}_{-0.07}$ | $6.00^{+0.05}_{-0.01}$ | $6.00^{+0.03*}_{-\infty}$ | $6.25^{+0.06}_{-0.13}$ |
| $\sigma$ [keV] | $0.41^{+0.10}_{-0.10}$ | $1.08^{+0.10}_{-0.04}$ | $1.04^{+0.06}_{-0.82}$ | $0.77^{+0.15}_{-0.06}$ |
| norm$_{\rm line}$ [$10^{-3}$] | $13^{+2}_{-2}$ | $37^{+3}_{-1}$ | $38^{+1}_{-2}$ | $21^{+3}_{-2}$ |
| $kT_{\rm in}$ [keV] | $0.82^{+0.01}_{-0.05}$ | $0.85^{+0.02}_{-0.01}$ | $0.80^{+0.01}_{-0.01}$ | $1.10^{+0.07}_{-0.10}$ |
| norm$_{\rm bb}$ | $421^{+33}_{-116}$ | $212^{+17}_{-14}$ | $288^{+23}_{-16}$ | $33^{+8}_{-4}$ |
| $\ell_{\rm h}/\ell_{\rm s}$ | $3.07^{+0.01}_{-0.04}$ | $3.36^{+0.02}_{-0.01}$ | $4.06^{+0.03}_{-0.02}$ | $3.83^{+0.02}_{-0.05}$ |
| $\tau_p$ | $1.24^{+0.01}_{-0.03}$ | $1.14^{+0.03}_{-0.01}$ | $1.30^{+0.01}_{-0.01}$ | $1.28^{+0.04}_{-0.03}$ |
| $\Omega/2\pi$ | $0.33^{+0.01}_{-0.01}$ | $0.31^{+0.01}_{-0.01}$ | $0.29^{+0.01}_{-0.01}$ | $0.28^{+0.01}_{-0.01}$ |
| $\xi$ | $798^{+103}_{-139}$ | $0^{+5}_{-0}$ | $1^{+3}_{-1}$ | $3^{+7}_{-3}$ |
| norm$_{\texttt{eqpair}}$ [$10^{-3}$] | $11.0^{+1.0}_{-0.1}$ | $10.0^{+0.6}_{-2.0}$ | $13.0^{+0.1}_{-0.9}$ | $4.0^{+0.6}_{-1.0}$ |
| A$_{\rm HEXTE}$ | $1.173^{+0.003}_{-0.004}$ | $1.071^{+0.003}_{-0.002}$ | $1.040^{+0.002}_{-0.003}$ | $1.013^{+0.003}_{-0.002}$ |
| A$_{\rm ISGRI}$ | $1.05^{+0.01}_{-0.01}$ | $0.94^{+0.01}_{-0.01}$ | $0.96^{+0.01}_{-0.01}$ | $0.85^{+0.01}_{-0.01}$ |
| A$_{\rm JEM\text{-}X}$ | $1.12^{+0.01}_{-0.01}$ | $1.00^{+0.01}_{-0.01}$ | $1.06^{+0.01}_{-0.01}$ | $0.92^{+0.01}_{-0.01}$ |
| A$_{\rm SPI}$ | $1.36^{+0.01}_{-0.01}$ | $1.14^{+0.01}_{-0.01}$ | $1.19^{+0.01}_{-0.01}$ | $1.03^{+0.01}_{-0.01}$ |
| $\chi^2_{\rm red}$ / dof | 1.370/350 | 1.471/242 | 2.038/267 | 1.528/257 |

* parameter could not be constrained so lower limit was set to 6.00 keV

$\Omega/2\pi = 0.356^{+0.005}_{-0.007}$ are also higher than in the pure thermal model. While the inner disk temperature decreases to $1.02^{+0.01}_{-0.03}$ keV and the disk normalization increases to $56^{+10}_{-7}$, the values found for the Fe K$\alpha$ line do not change significantly with respect to the thermal model.

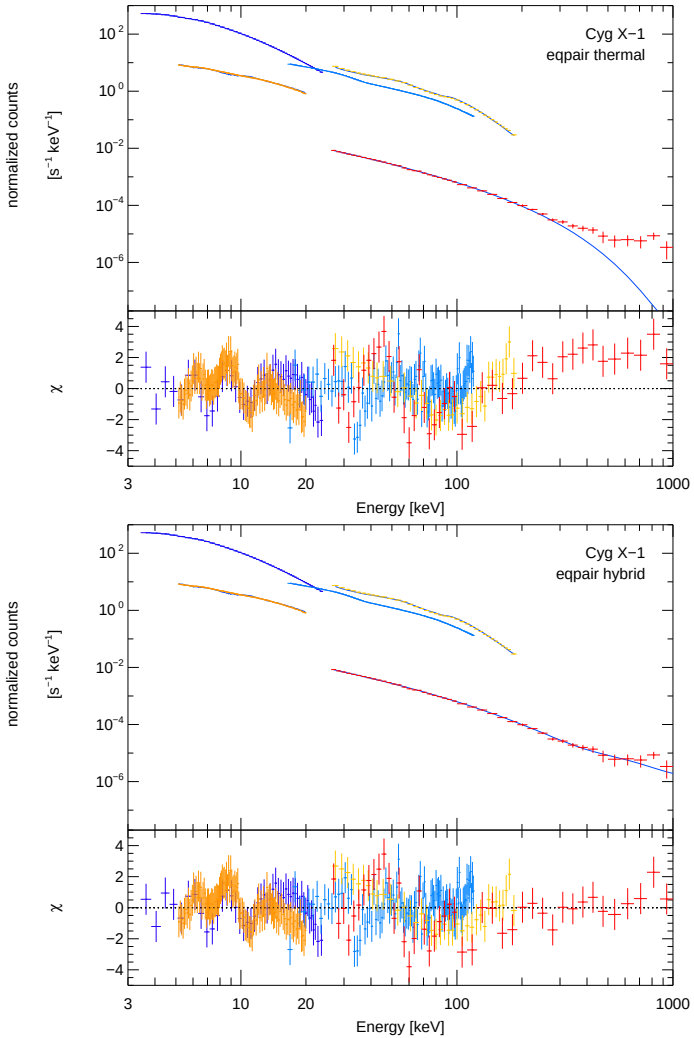


Figure 3.9: Top: Thermal `eqpair` model (time average over all observations). Bottom: Hybrid `eqpair` model.

## *3.5 Summary and Discussion*

We have modeled the 3 keV–1 MeV broadband spectrum of Cyg X-1 based on a pure phenomenological basis with a broken power law model as well as with

Table 3.8: Best fit parameters for the time averaged `eqpair` model.

| | `eqpair` (thermal) | `eqpair` (hybrid) |
|---|---|---|
| $N_{\rm H}$ [$10^{22}$cm$^{-2}$] | $0^{+0.07}_{-0}$ | $0^{+0.19}_{-0}$ |
| $E_{{\rm K}\alpha}$ [keV ] | $6.37^{+0.03}_{-0.12}$ | $6.30^{+0.04}_{-0.13}$ |
| $\sigma_{{\rm K}\alpha}$ [keV ] | $0.71^{+0.10}_{-0.05}$ | $0.77^{+0.14}_{-0.05}$ |
| norm$_{\rm line}$ [$10^{-3}$] | $19^{+1}_{-2}$ | $21^{+3}_{-1}$ |
| $kT_{\rm in}$ [keV ] | $1.15^{+0.02}_{-0.03}$ | $1.02^{+0.01}_{-0.03}$ |
| norm$_{\rm bb}$ | $37^{+3}_{-3}$ | $56^{+10}_{-7}$ |
| $\ell_{\rm h}/\ell_{\rm s}$ | $3.28^{+0.01}_{-0.02}$ | $4.74^{+0.02}_{-0.03}$ |
| $\ell_{\rm nth}/\ell_{\rm h}$ | – | $0.67^{+0.01}_{-0.17}$ |
| $\tau$ | $1.235^{+0.010}_{-0.018}$ | $1.420^{+0.008}_{-0.007}$ |
| $\Omega/2\pi$ | $0.299^{+0.004}_{-0.006}$ | $0.356^{+0.005}_{-0.007}$ |
| $\xi$ | $0^{+14}_{-0}$ | $0^{+8}_{-0}$ |
| norm$_{\texttt{eqpair}}$ [$10^{-3}$] | $3.10^{+0.04}_{-0.01}$ | $5.00^{+0.07}_{-1.00}$ |
| A$_{\rm HEXTE}$ | $1.065^{+0.002}_{-0.002}$ | $1.065^{+0.002}_{-0.002}$ |
| A$_{\rm ISGRI}$ | $0.948^{+0.008}_{-0.008}$ | $0.946^{+0.008}_{-0.008}$ |
| A$_{\rm JEM\text{-}X}$ | $1.025^{+0.008}_{-0.008}$ | $1.025^{+0.008}_{-0.008}$ |
| A$_{\rm SPI}$ | $1.138^{+0.003}_{-0.003}$ | $1.139^{+0.003}_{-0.004}$ |
| $\chi^2_{\rm red}$ / dof | 1.656 / 324 | 1.387 / 323 |

the more sophisticated Comptonization models `compTT` and `eqpair`. The fits resulted in an equally good description of the data in terms of the $\chi^2_{\rm red}$. Our results are in good accordance with the long *RXTE* monitoring campaign, showing that the main parameters of the models do not change much when the energy range is extended from 120 keV to 1 MeV. However, while a simple thermal `eqpair` model was sufficient to describe the data in the 3–120 keV *RXTE* range, the *INTEGRAL* data showed evidence for the presence of a hard tail in the high energy part of the

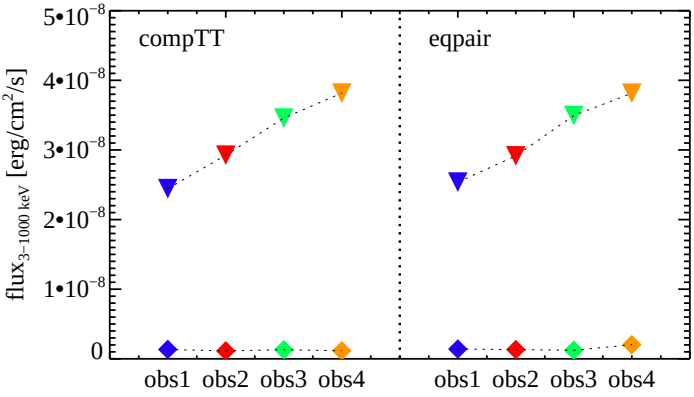


Figure 3.10: Strength of spectral components in the `compTT` and `eqpair` model. The diamonds mark the disk component, the triangles the Comptonization component of the spectra.

spectrum. We therefore applied a hybrid thermal/non-thermal `eqpair` model to the time averaged spectrum which turned out to give a better description of the high energy range. A hard tail has been reported before for Cygnus X-1 in the Soft state by Gierliński et al. (1999) and McConnell et al. (2002, who also report a weak tail above ~1 MeV in the hard state) and in the Intermediate state by Cadolle Bel et al. (2006).

As was already indicated from the ASM light curve, we observed Cyg X-1 not in one of its canonical Hard or Soft states but in an Intermediate state. The comparison with the *RXTE* monitoring results leads to the assumption that the source was caught in the Hard Intermediate state. This assertion can be further quantified based on the definition by Belloni (2005) as there is clearly a soft disk component present. The overall spectrum, however, is dominated by the hard Comptonization component as is shown in Fig. 3.10: the diamonds show the 3 keV– 1 MeV flux of the disk component of the spectrum, the triangles the flux of Comptonization component[8] (on the left for the `compTT` fits, on the right for the `eqpair` ones). Note also that both models show very similar results with a clear increase in the strength of the Comptonization from obs1 to obs4, indicating that the later observations are closer to the hard state than the first observations. This behavior can also be seen in Figs. 3.5 to 3.8.

[8]The fluxes shown in Fig. 3.10 are PCA 3 keV– 1 MeV fluxes. To calculate them the PCA response was extended accordingly.

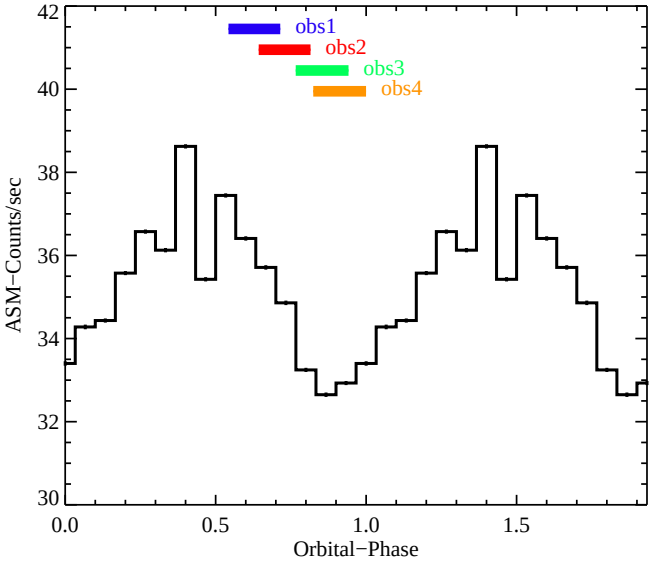


Figure 3.11: ASM light curve folded with the orbital period of 5.599829 d. The colored bars mark the phases of our *INTEGRAL* observations.

Another feature observed in both Comptonization models is $N_{\rm H}$ showing a clearly higher value in obs1 than in the three other observations. As shown in Fig. 3.11, obs1 corresponds to an orbital phase $\Phi \approx 0.54 - 0.71$. It has been previously reported by Wen et al. (1999) and Bałucińska-Church et al. (2000) that Cyg X-1 shows an orbital phase dependence of the absorption column with an increased absorption near superior conjunction at phase 0.95 (due to absorption in the wind of HDE 226868) and around phase 0.6 (due to absorption in the accretion stream). Therefore this increased absorption in obs1 is consistent with previous results. Based on this previous findings there should also be an increase in absorption be visible in obs4 which completely covers phase 0.95. However, there is no indication of such an increase in the two models used.

The iron line is found to have a rather large line width $\sigma$ in all models, indicating the presence of a relativistically broadened line[9]. This result is consistent with previous results not only from from the *RXTE* monitoring but also from Frontera et al. (2001b) and Ibragimov et al. (2005). The line parameters themselves, however, can only be well constrained in the Broken Power law fits. Here

[9]The PCA is able to resolve lines down to $\sigma \sim 0.3$ keV (Wilms et al. 2006).

the line energy and the width as well as the normalization are consistent for all four observations. On the contrary, all the fits with the Comptonization models show problems in constraining either the energy of the line (as is the case for the `compTT` models where the line energy had to be fixed to 6.40 keV) or show a huge variation in $\sigma$. An example for a very large disagreement in $\sigma$ is given in the `eqpair` fits of obs1 and obs2 with a $\Delta\sigma$ of 0.53 keV even if applying the error ranges.

A comparison of our time averaged spectral parameters with the Intermediate state observation from MJD 52797–52801 by Cadolle Bel et al. (2006) which covers nearly the same energy range (5 keV– 1 MeV) shows in principle a good agreement, however, there are some differences. While their overall spectrum also favors a hybrid thermal/non-thermal model with $\ell_\mathrm{h}/\ell_\mathrm{s} = 4.57^{+0.04}_{-0.87}$ (which is very similar to $\ell_\mathrm{h}/\ell_\mathrm{s} = 4.74^{+0.02}_{-0.03}$ obtained in our fits), the fraction of power supplied to the non-thermal acceleration of electrons is significantly smaller in their case ($\ell_\mathrm{nth}/\ell_\mathrm{h} = 0.16^{+0.11}_{-0.08}$ compared to $\ell_\mathrm{nth}/\ell_\mathrm{h} = 0.67^{+0.01}_{-0.17}$). Also the values of the reflection covering factor ($\Omega/2\pi = 0.63^{+0.08}_{-0.08}$ compared to $\Omega/2\pi = 0.356^{+0.005}_{-0.007}$) and the pair optical depth ($\tau_\mathrm{p} = 0.49^{+0.24}_{-0.02}$ versus $\tau_\mathrm{p} = 1.14^{+0.03}_{-0.01}$) differ significantly. There are also differences in the normalization of the `diskbb` model, as these authors obtain $250^{+89}_{-59}$ which is much larger than the normalization of $56^{+10}_{-7}$ in our case[10]. All these differences can most probably be attributed to the fact that Cyg X-1 was in a softer state in the Cadolle Bel et al. (2006) observation than in our observation. The larger normalization value of the `diskbb` model shows the presence of a stronger disk component in the spectrum (as expected in the Soft state). This assumption is further confirmed by the `compTT` fits of Cadolle Bel et al. (2006), which reveal a Compton $y$ of only 0.19 which differs significantly from the 0.5 found for the hard state by Wilms et al. (2006) (and also from the $y = 0.37$ found in our `compTT` fits).

As already mentioned some of the spectral parameters of Cadolle Bel et al. (2006) differ significantly from our time averaged values. Moreover, when trying to place the results of Cadolle Bel et al. (2006) in the *RXTE* monitoring campaign to constrain our assertion of a softer state in their observation further, we noticed that their parameters do also not fit the correlations found in the campaign. Fig. 3.12 shows the compactness / optical depth correlation with the fit results of Cadolle Bel et al. (2006) indicated by violet triangles and the spectral parameters of the time averaged spectrum of this work marked with orange diamonds (pure thermal as well as hybrid `eqpair` model). The optical depth found by Cadolle Bel et al. (2006) is much smaller than the corresponding values of the campaign.

[10]The disk temperatures are comparable in both observations with $kT_\mathrm{in} = 1.16^{+0.07}_{-0.07}$ keV and $kT_\mathrm{in} = 1.02^{+0.01}_{-0.03}$ keV, respectively.

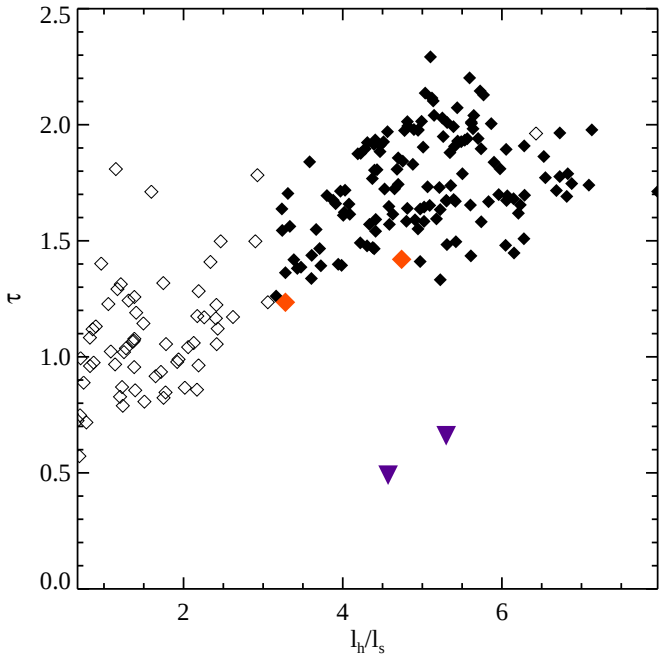


Figure 3.12: Relationship between the optical depth $\tau$ and the compactness ratio $\ell_h/\ell_s$. The violet triangles indicate the values quoted by Cadolle Bel et al. (2006) for their thermal and hybrid `eqpair` model, respectively, the orange diamonds the values obtained in this work for the time averaged spectrum.

This low optical depth is counterbalanced by the high reflection covering factor of $\sim 0.7$ found by these authors (which is much higher than the values found in the *RXTE* campaign). The differences in the spectral parameters are most likely due to the rather high lower energy threshold of the *INTEGRAL* observations: the JEM-X data start only at 5 keV which makes the determination of the disk parameters – and therefore the seed photon temperature – difficult. This example clearly shows how the whole spectrum is influenced by the low energy part and emphasizes the need for good broadband data.

# Chapter 4

# The Relativistic Iron Line – Techniques

The study of the K$\alpha$ fluorescent line of iron is one of the most powerful tools in the analysis of black holes. The line originates from rotating material which is just a few gravitational radii away from the black hole and therefore it is broadened by gravitational redshift effects as well as by Doppler shifts. Hence an analysis of the line shape is essential for the understanding of the accretion geometry and for the estimation of the black hole spin.

In this chapter an introduction to relativistically broadened iron lines is given, followed by a short description of the *XSPEC* models used in this thesis to describe the line profiles. The second part of this chapter is dedicated to the Modified Timing Mode, a new observing mode developed by our group for the EPIC-pn camera of *XMM-Newton*.

## *4.1 Relativistically broadened Iron lines*

The Fe K$\alpha$ line from disks around black holes is intrinsically narrow (the natural width is of the order of 1 eV, Pozdnyakov et al. 1979) with a rest frame energy of 6.4 – 6.97 keV, depending on the ionization state. It originates from material which is just a few gravitational radii away from the black hole and therefore it is broadened by gravitational redshift as well as by Doppler shifts. If one takes a symmetric double-peaked profile from a rotating non-relativistic Newtonian disk as starting point, as it is shown in the first panel of Fig. 4.1, and then first “turns on” the effects of special relativity, relativistic beaming enhances the blue peak and the transverse Doppler shift lead to a reddening of the whole profile (second panel). Finally the gravitational redshift, an effect of general relativity, reduces the strength of the blue peak and shifts the profile to lower energies (i.e., the "red" side of the energy spectrum). This effect is shown in the third panel, while the forth panel shows the integrated line profile of the whole disk.

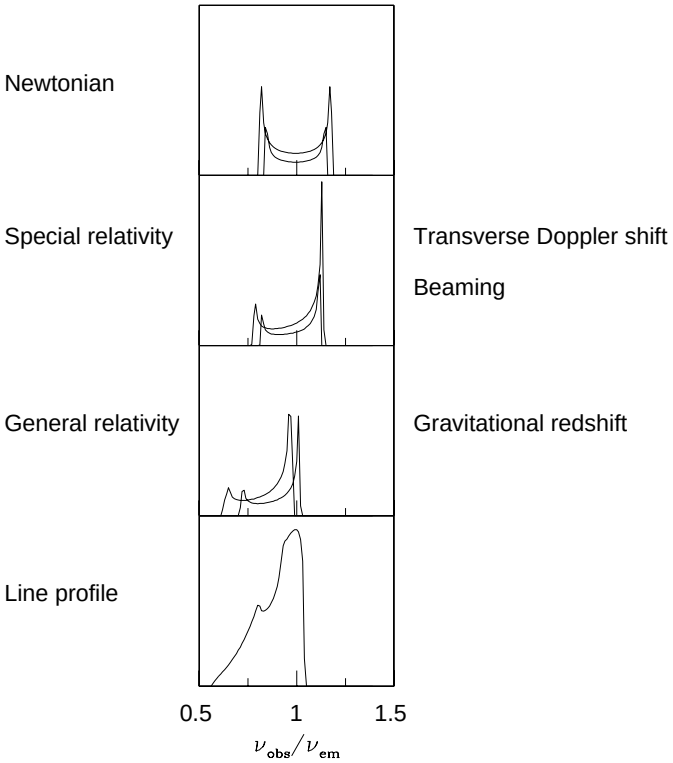


Figure 4.1: The modification of an intrinsically narrow iron line by the effects of special and general relativity (Fabian 2006).

The exact shape of the line depends on several input parameters[1]:

- the accretion geometry,
- the Fe K$\alpha$ emissivity of the disk (parametrized by the disk emissivity index $\beta$), and
- the observer's viewing angle (parametrized by the disk inclination $i$).

The most important point of the **accretion geometry** is the position of the innermost radius of the disk. If one assumes that this radius is located at the innermost

[1]The following explanations are based on the review on relativistically broadened iron lines by Reynolds & Nowak (2003).

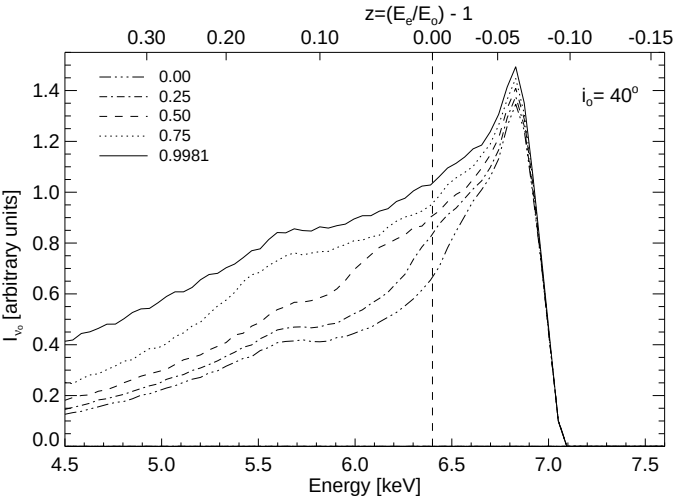


Figure 4.2: The dependence of the iron line profile of different spin parameters (Wilms et al. 1998). The disk emissivity index $\beta$ and the inclination $i$ are fixed. The emitting part of the disk is assumed to extend from $R_{\rm out} = 50GMc^{-2}$ to $R_{\rm ISCO}$.

stable circular orbit $R_{\rm ISCO}$, the shape of the line is directly linked to the spin of the BH. In case of a non-rotating BH this radius is located at $6GMc^{-2}$, for a maximally rotating BH it moves further inward to $1.23GMc^{-2}$ (note that this value quotes the position of $R_{\rm ISCO}$ for a co-rotating BH; in case of a counter-rotating BH $R_{\rm ISCO} = 9GMc^{-2}$, which means that the disk is truncated even further away from the BH than in the non-rotating case). Fig. 4.2 shows the emitted line profiles for different spin parameters $a$ while keeping the inclination fixed to 40° and the disk emissivity index $\beta$ to 3. With increasing spin parameter the inner edge of the disk moves closer to the BH, and the velocity of the gas increases. This results in a larger range of Doppler shifts and the red wing of the line extends further down to lower energies while the blue wings are almost indistinguishable.

The local **emissivity of the disk** can be parametrized as

$$I_{\nu_e}(r_{\rm e}, i_{\rm e}) \propto f(i_{\rm e}) r_{\rm e}^{-\beta} \quad , \tag{4.1}$$

which means that the emissivity varies with the radius as a power law. For large values of the emissivity index $\beta$, most of the radiation is emitted near $R_{\rm ISCO}$, hence the profile becomes broader with increasing $\beta$. This effect can clearly be seen in Fig. 4.3. For $\beta > 2$ the red wing becomes very weak until it is almost undetectable. Another point to note is that the outer radius of the disk becomes more and more

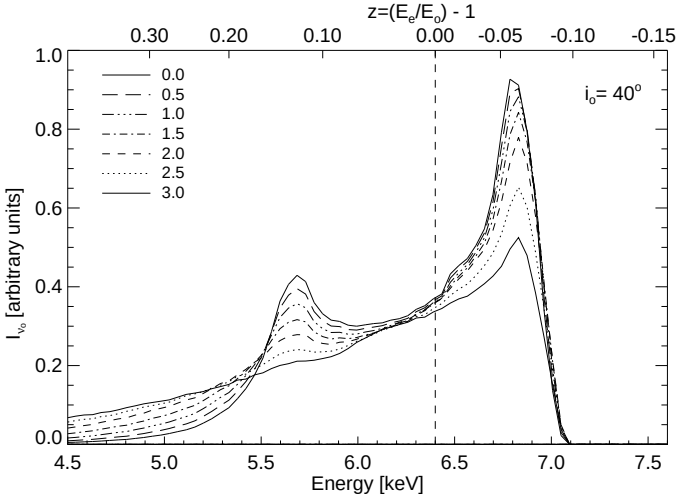


Figure 4.3: The variation of the iron line profile depending on the emissivity index $\beta$ (Wilms et al. 1998). The BH is assumed to rotate with a spin parameter of $a = 0.5$ and the inclination $i$ is fixed at 40°. The emitting part of the disk is assumed to extend from $R_{\rm out} = 50GMc^{-2}$ to $R_{\rm ISCO}$.

unimportant for $\beta > 2$ while it is relatively important for small values of $\beta$, as most of the emission then comes from the outer regions of the disk.

Finally Fig. 4.4 shows that the shape of the profile depends strongly on the **observers viewing angle**. For large values of the inclination $i$ the Doppler effect dominates over the gravitational redshift and the profile becomes broader. If the disk is seen more face-on – which means $i$ decreasing to 0 – the gravitational redshift dominates, the line profile becomes rather narrow, but even at $i = 0$ the line is still broader than in the non-relativistic case.

## *4.2 Models*

There are several *XSPEC* models to describe the profiles of relativistically broadened iron lines. In the scope of this thesis the two models `diskline` and `laor` were used. The `diskline` model (Fabian et al. 1989) describes the lines emitted from a Schwarzschild BH, meaning $a = 0$. It does not include the effects of light bending which leads to an inaccurate calculation of the relativistic effects near the BH ($r < 20GMc^{-2}$, Beckwith & Done 2004). The other model, `laor`, accounts

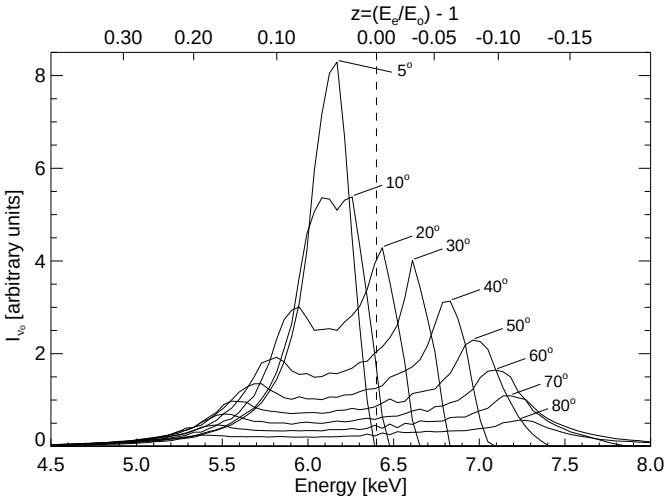


Figure 4.4: Iron line profiles as a function of the inclination angle $i$ (Wilms et al. 1998). The disk emissivity index $\beta = 0.5$ and the spin parameter $a = 0.998$ are fixed. The emitting part of the disk is assumed to extend from $R_{\rm out} = 50GMc^{-2}$ to $R_{\rm ISCO} \approx 1.23GMc^{-2}$.

for the opposite case of a maximally spinning BH ($a = 0.998$). It calculates the line profiles numerically and also includes light bending. Unfortunately the accuracy of this model is limited by the rather small number of tabulated transfer functions used (Beckwith & Done 2004).

In addition to these two relativistic line models, the iron line profile was modeled using a "normal" Gaussian emission line which was afterwards relativistically blurred with the *XSPEC* model `kdblur`.

### *4.2.1 The XSPEC model* `diskline`

The `diskline` model (Fabian et al. 1989) assumes a thin axis-symmetric disk which is observed under the inclination angle $i$ and extends from $r_0$ down to $r_{\rm i}$. The specific flux carried to the observer can be written as

$$dF_{E_{\rm obs}} = (1+z)^{-3} I_{E_{\rm em}} \left[ \frac{\partial \Omega}{\partial(r,\Phi)} \right] r_{\rm em} dr_{\rm em} d\Phi_{\rm em} \tag{4.2}$$

with $(1+z) = E_{\rm em}/E_{\rm obs}$. In the case of a narrow line with rest energy $E_0$ the specific intensity $I_{E_{\rm em}}$ can be approximated by a delta function $I_{E_{\rm em}} = \epsilon\delta(E_{\rm em} - E_0)$ with the surface emissivity function $\epsilon$, which in the `diskline` model is assumed

to be isotropic and to have a power-law form $\epsilon \propto (r_{\rm em}/M)^{-\beta}$. After some simplifications due to the Schwarzschild metric (where the photon geodesics are planar), the observed flux is calculated by integrating equation 4.2 over all $r_{\rm em}$ and $\Phi_{\rm em}$.

### 4.2.2 The XSPEC model `laor`

In the `laor` model (Laor 1991) the line profiles are calculated numerically by following the trajectories of the photons from the rest frame of the matter in the disk to the rest frame of an observer at infinity. To do this calculation, a transfer function $T$ is created out of the observed photon inclination angle and energy shift. Assuming a standard limb-darkening law of $I(\cos\theta_{\rm e}) \propto 1 + 2.067\cos\theta_{\rm e}$ leads to a line profile of the form

$$F_{\rm o}(\theta_{\rm o}, \nu_{\rm o}) = \int T(\theta_{\rm o}, r_{\rm e}, \nu_{\rm o}/\nu_{\rm e}) J(r_{\rm e}) dr_{\rm e} \tag{4.3}$$

where $J(r_{\rm e})$ is the line-emissivity law. As already said above the transfer functions are tabulated[2].

### 4.2.3 The XSPEC model `kdblur`

The models described above are physically "incomplete" as one would expect the line as well as the continuum being blurred by relativistic effects due to the vicinity of the strong gravitational field of the black hole. This blurring can formally be understood in the Green's functions formalism which acts on the continuum flux and on a delta shaped line in such a way that

$$F_{\rm obs}(\epsilon) = \int_0^\infty G_{\rm kdblur}(\vec{x}, \epsilon, E) F_{\rm em}(E) {\rm d}E \quad . \tag{4.4}$$

A way to "combine" the disk reflection spectrum with the line emission in *XSPEC* is to convolve both with the relativistic blurring kernel `kdblur` which is derived from the `laor` code (Fabian et al. 2002). Thereby the line gets broadened and the reflection continuum gets smoothed. This `kdblur` model was already successfully used to describe the line emission in AGN (e.g., Fabian et al. 2002; Longinotti et al. 2004) and has also been applied to galactic black holes (i.e., GX 339−4, Tomsick et al. 2008; Reis et al. 2008).

[2]The grid of transfer functions includes 31 values of $\theta_{\rm o}$, 35 values of $r_{\rm e}$ (with $r_{\rm e}$<400 as the energy shift for larger $r_{\rm e}$ is less than 4%) and 300 values of $\nu_{\rm o}/\nu_{\rm e}$ (with $0.1 \leq \nu_{\rm o}/\nu_{\rm e} \leq 1.7$ which corresponds to an energy resolution of $\nu_{\rm o}/\Delta\nu_{\rm o} = 105$).

## *4.3 The Modified Timing mode of XMM-Newton*

The first report of a broadened iron line line in Cyg X-1 was given by Barr et al. (1985) based on *EXOSAT* data. Since then the energy resolution of the instruments has improved significantly, so that it is nowadays possible to study the line shape in great detail like it was done, e.g., by Miller et al. (2002) using the Chandra observatory. For this thesis observations from the *XMM-Newton* satellite were used to analyze the structure of the iron line. Actually Cyg X-1 is too bright to be observable by this instrument with a satisfying signal to noise ratio in its standard observing modes. Our group, however, developed a new observing mode for the EPIC-pn camera which allows the observation of sources with a luminosity of up to $\sim 1$ Crab. The details about this new observing mode and its calibration are given in the following sections.

### *4.3.1 Observation of bright sources with XMM-Newton*

The telemetry allocated to the EPIC-pn is restricted to 16 kbit $s^{-1}$ (nominal rate, the maximal rate is 40 kbit $s^{-1}$, Kendziorra et al. 1999) therefore it is not always trivial to study bright sources with the maximum possible time resolution in combination with a satisfying signal to noise ratio using the standard modes of *XMM-Newton*. On one hand in the EPIC-pn burst mode (which is foreseen for very bright sources) only 3% of all detected photons are transmitted resulting in an enormous reduction of the signal to noise ratio[3], on the other hand the EPIC-pn Timing mode – which would have an effective exposure time of 99.5% – can be used only up to 250 events $s^{-1}$ in the standard telemetry allocation (Kendziorra et al. 2004).

For sources like Cyg X-1 with about 300 mCrab ($\sim 3000$ counts $s^{-1}$) an alternative approach is needed. Switching off the EPIC-MOS camera – which is appropriate since for the MOS cameras there is no data mode available which can handle sources as bright as Cyg X-1– increases the maximum processable EPIC-pn count rate to 1050 counts $s^{-1}$, as the full telemetry of 40 kbit $s^{-1}$ is allocated to the EPIC-pn.

Furthermore the EPIC-pn is operated in a Modified Timing mode (Kendziorra et al. 2004): In this mode the lower energy threshold is increased to 2.8 keV (the standard value is 200 eV), resulting in a reduced count rate of about 500–800 counts $s^{-1}$ which is well within the technical limits. This modification of the lower energy threshold, however, implies that a re-calibration of the instrument is required because the recombination of split events[4] is not performed on-board

[3] Another drawback of using the burst mode for the special case of our Cyg X-1 observation is its inappropriateness for PSD studies (Kuster et al. 1999).

[4] Split events are events which do not deposit their whole energy in one pixel (which would be

Table 4.1: Observation modes that are available for the EPIC cameras. Actually only the burst mode is usable for the observation of bright sources, but a major drawback is the very restricted life time of 3% (Ehle et al. 2005).

| | Time res. | Live time [%] | Max. cps | mCrab |
|---|---|---|---|---|
| EPIC-MOS | | | | |
| Full frame (600×600) | 2.6 s | 100.0 | 0.70 | 0.24 |
| Large window (300×300) | 900 ms | 99.5 | 1.8 | 0.6 |
| Small window (100×100) | 300 ms | 97.5 | 5 | 1.7 |
| Timing uncomp. (100×600) | 1.5 ms | 100.0 | 100 | 35 |
| EPIC-pn | | | | |
| Full frame (376×384) | 73.4 ms | 99.9 | 6 | 0.7 |
| Ext. full frame (376×384) | 200 ms | 100.0 | 2 | 0.25 |
| Large window (198×384) | 48 ms | 94.9 | 10 | 1.1 |
| Small window (63×64) | 6 ms | 71.0 | 100 | 11 |
| Timing (64×200) | 0.03 ms | 99.5 | 800* | 85 |
| Burst (64×180) | 7 $\mu$s | 3.0 | 60000 | 6300 |

* The actual limiting count rate is 250 cts $s^{-1}$, for a higher count rate the counting mode is triggered

but during the first step of the EPIC-pn data analysis. Due to the increased lower threshold a large fraction of the split partners is not transmitted and therefore the spectrum appears to be softer as the events are wrongly recorded as single events with lower energy as it is shown in Fig. 4.5.

### *4.3.2 Calibration of the Modified Timing mode – The new response matrix*

The basic idea for the calculation of a new response matrix, which is able to account for the apparent spectral softening described in the section above, is to use the standard Timing mode response matrix as a basis and then adapt it to the Modified Timing mode by multiplying it with a second redistribution matrix which describes the difference between the standard Timing mode and the Modified Timing mode. This redistribution matrix assigns each PI channel of the original matrix a detection probability in the Modified Timing mode (see Fig. 4.6). To derive this detection probability, the Modified Timing mode has been simulated by taking standard Timing mode observations and discard all events with energies below 2.8 keV. Afterwards it is possible to compare the respective events on a time- and position basis and select those events which are single events for the redistribution

called "single events") but in two or even three or four neighboring pixels (see, e.g., Dennerl et al. 1999).

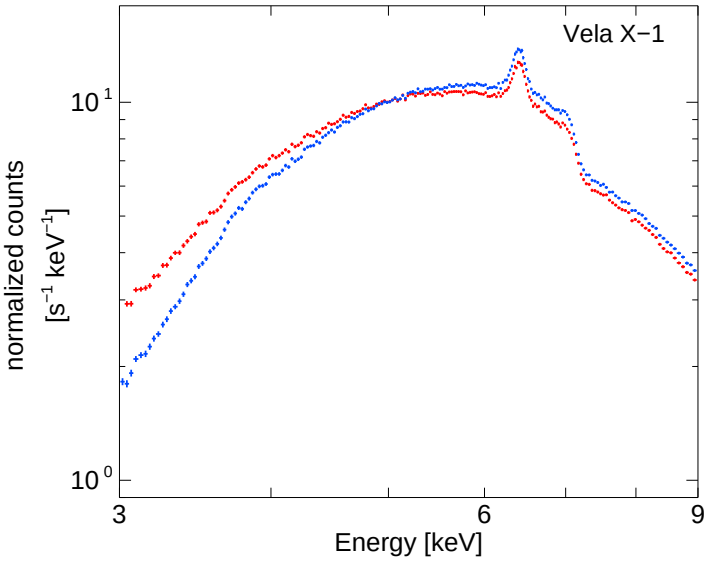


Figure 4.5: Comparison of a simulated Modified Timing mode observation (blue) of Vela X-1 and its standard Timing mode Observation counterpart (red). The spectrum appears to be softer as split events with partners below the new lower threshold of 2.8 keV are wrongly recorded as single events.

matrix.

To calculate the new response matrix we used all public available Timing mode observations. In a first step we studied the pattern plots created with the SAS tool *epatplot* of all individual observations and selected those satisfying the two conditions

1. the observation is not affected too much by pile-up
2. the source is at least measured with 3 cts s$^{-1}$

After this selection 66 out of 115 observations remained for the calculation of the new response. A full list of the observations can be found in Appendix A. Furthermore the remaining observations had to be sorted according to the filter used for the respective observation. This further selection was necessary as optically generated electrons shift the measured X-ray energy by $n_{\rm op} \times 3.68\,$eV (Kendziorra et al. 1999). As the number of the optically generated electrons, $n_{\rm op}$, depends on the filter used, the matrix calculation has to be done for each filter individually.

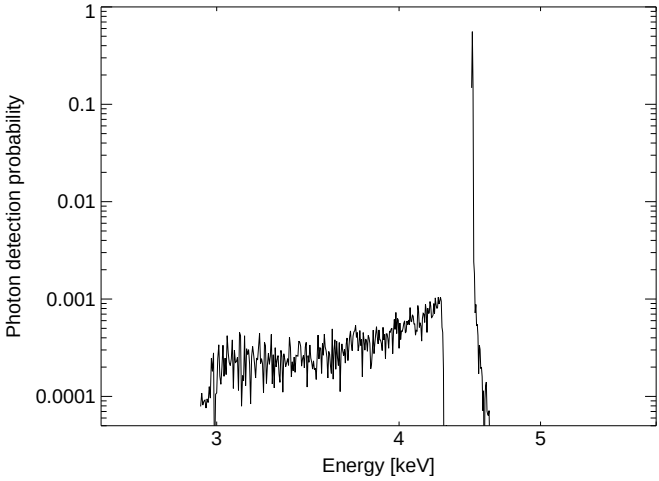


Figure 4.6: Cut through the Modified Timing mode redistribution matrix at channel 900 (to increase statistics 21 channels have been added up for the plot). Photons with an energy of 4.5 keV have a probability of ~55% to be detected at exactly this energy in the Modified Timing mode, but they might also be detected at lower energies as the split events can be wrongly recorded as single events with lower energy due to the increased lower energy threshold. The gap between the peak of the "correct" recorded photons and the redistributed ones is due the 0.2 keV lower energy threshold of the standard Timing mode.

The 66 observations were extracted using SAS 7.0.0 once in a normal manner, and then a second time, filtering out all events with energies less than 2.8 keV to simulate the conditions of the Modified Timing mode. Afterwards the data sets are processed through a series of three IDL routines (written originally by J. Wilms) which are described in the following[5].

**patdist.pro** is a tool for the calculation of the single/double distribution by comparison of the filtered data with the original data. The program loops over all observations and performs the following steps:

- read event file of original Timing mode observation in *orig*
- read event file of filtered Timing mode observation in *filt*
- select events from columns needed for matrix generation (according to source extraction region)

[5]In the description of the IDL routines the words printed in *italics* refer to variable names used in the code.

- build histogram (= spectrum) of original event file (*inputpi*)
- build histogram (= spectrum) of filtered event file (*modifpi*)
- loop over all events in *filt* to find matching original event by
  1. searching for first event in *orig* that has the same time and then
  2. searching for the event in *orig* that also has the same rawx position
- write array *filtpi* containing a histogram of the energies of the found events (first index: original PI, second index: PI in the filtered file) → the main diagonal contains all single events whereas the multiple events are scattered around the diagonal
- build histogram (=spectrum) of the not found original events (*notfoundpi*)
- build histogram (=spectrum) of the not found filtered events (*filtnotfoundpi*)
- plot histograms
- save all relevant data (*filtpi,inputpi,modifpi,notfoundpi,filtnotfoundpi*)

To summarize: The main output of this first program is the *filtpi* array for all of the observations which allows a direct identification of the single events.

The second step towards the calculation of the new matrix is done in the program **makedist.pro**. Here the pattern distributions are converted into a photon detection probability as a function of the PI energy of the standard Timing mode (for initial photon energies in a certain range). In this procedure the user has to define the observations that should be ignored for the calculation of the matrix (due to pile-up or other reasons as described above). This routine is usually called from the last program, makematrix.pro, with the two variables *emin* and *emax*. To simplify the description of makematrix.pro later on, the steps executed by makedist.pro are already explained here:

- loop over all observations (specify those to be ignored first!) and read in *filtpi* and *inputpi*
- sum up all *filtpi* into one new *filtpi*
- sum up all *inputpi* into one new *inputpi*
- calculate the channels (=columns) corresponding to *emin* and *emax* in *filtpi*
- pick the channel corresponding to *emin* (*filtsum*)
- check if *filtsum* contains entries with value "1" and if yes set them to "0" (to reduce the noise)
- shift the entries of all following channels up to the channel corresponding to *emax* in such manner that all single events (that means entries from the diagonal) end up in the same line
- check for those channels also if they contain entries with value "1" and if yes set them to "0"
- sum up the channels (new *filtsum*) to calculate the distribution of photons detected in the Modified Timing mode in the range from *emin* to *emax*

- sum up the corresponding entries of *inputpi* (*totph*) to calculate the total input photons in the standard Timing mode in the range from *emin* to *emax*
- normalize *filtsum* to a detection probability through dividing by *totph* and write in in *dist*
- calculate output energies

To summarize: the main return parameter of this step is the *dist* array which contains the detection probabilities for the energy range defined by *emin* and *emax*.

The final routine needed is **makematrix.pro**. In this last step the calculated probability distributions are merged with an available standard Timing mode RMF and ARF[6]. The RMF and ARF of the standard Timing mode have been multiplied before to get an .rsp file. The program makematrix.pro runs as follows:

- loop over all 4096 PI channels
  1. calculate values of *emin* and *emax* from channel number and given energy resolution *de* (*de* = 10 in this case, corresponding to 50 eV bins as 1 channel would have to bad statistics)
  2. call makedist.pro for the current values of *emin* and *emax*
  3. write resulting *dist* in that column of *redist* that corresponds to the current channel
- read in matrix/matrices of standard Timing mode for multiplication (*matrix*)
- multiply the matrix with the redistribution probabilities *redist*
- write out the new modified matrix/matrices

Using these programs, matrices have been calculated for all three filters available for the EPIC cameras. Fig. 4.7 shows example spectra of standard and corresponding simulated Modified Timing mode observations. The spectra have been fitted using the standard rmf and arf files for both observations (upper residual panel) showing a clear deviation. The bottom panel shows a fit using the newly calculated matrices for the Modified Timing mode. The residuals are now very similar, showing that the new response matrix is able to account for the effects of spectral softening as described in section 4.3.1. Respective plots for the "thin1" and "medium" filter can be found in Appendix A.

### *4.3.3 Calibration of the Modified Timing mode – CTE effects*

One unwanted side effect that occurs in the pn-CCD is an intrinsic charge transfer loss. This loss is due to contamination of the silicon with titanium, causing traps that are responsible for up to 20% loss of the total generated signal charge over

[6]Note that due to an bug in the SAS tool arfgen it is not possible to create correct ARF files for extraction regions containing gaps. The solution to this problem is to create an ARF for the whole detector and one for the region to be left out and to subtract this one from the first.

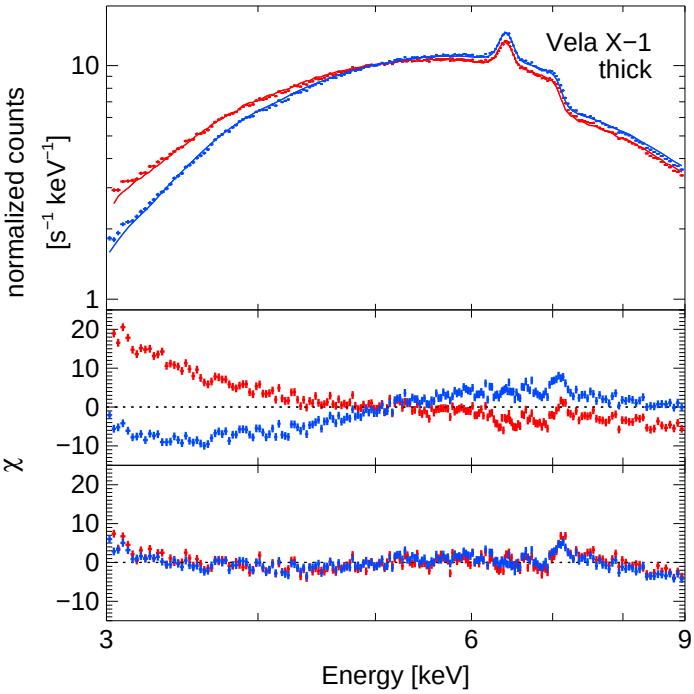


Figure 4.7: Comparison of the standard Timing mode response matrix and the newly calculated response matrix for the Modified Timing mode for the "thick" filter. The red spectrum again is the simulated Modified Timing mode observation of Vela X-1 already described in the previous section, whereas the blue one again shows the standard Timing mode observation. The upper panel displays the residuals for a fit to the data just using the standard rmf and arf files for both observations, resulting in strong differences in the residuals. The bottom panel shows the same but using the correct response matrix for the Modified Timing mode. The residuals are now very similar, showing that the response accounts for the effects of spectral softening as described in the text.

the maximum transfer length of 3 cm (Krause et al. 1999). The effect depends on several parameters like the device temperature, the precursor signal charge, the time elapsed between the signal and its precursor, and of course of the generated signal charge itself. This last mentioned point implies that the charge transfer efficiency (CTE) depends on the surface brightness on the CCD, as the signal charge created for luminous sources is high. The traps are therefore filled sooner the more luminous the source, and the charge loss decreases accordingly.

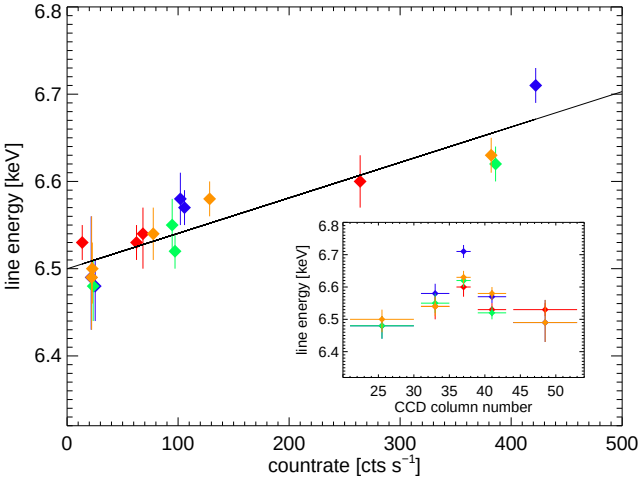


Figure 4.8: Shift of the energy of the narrow core of the iron line with luminosity. The inset shows the dependence of the energy on the position on the CCD – the source position around column 37 is clearly visible.

The response matrix of *XMM-Newton* corrects for these CTE effects routinely. However, as Cyg X-1 is a very bright source, the data are over-corrected due to the rapid filling of the traps by the high signal charge. This over-correction results in too high energy values as shown in Fig. 4.8. The plot shows the position of the narrow core of the iron line measured as function of luminosity. The values have been obtained by extracting spectra of different column combinations (21–30, 31–35, 36–38, 39–43, 44-53, the inset of Fig. 4.8 shows the position of the line as function of the position on the CCD) and fitting them respectively with a disk black body and power-law to model the continuum and a narrow and broad iron line (using the `diskline` model in this case). As shown in this plot, it must be stated that the energy values obtained for the iron line have an uncertainty of +150–200 eV due to the over-correction of the CTE effects.

It is known that the CTE is not only a function of luminosity, but also energy (as there is less charge loss for higher energies like it is the case for luminous sources), and column (see, e.g., Kirsch 1998). However, we considered a correction of the above described effects by a simple shift of the response matrix entries to match the position of the narrow core of the iron line at 6.4 keV. As we also have simultaneous *RXTE* observations, we used them for cross calibration: with

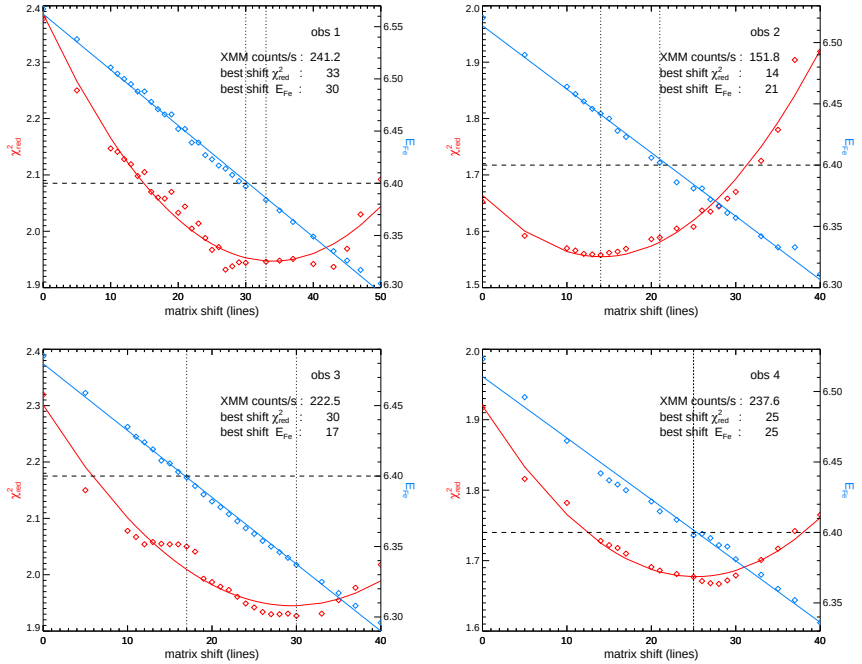


Figure 4.9: $\chi^2_{red}$ values (left y-axis) of the combined *XMM-Newton* + *RXTE* fits / measured position of the Fe K$\alpha$ line (right y-axis) vs. matrix shift in channels.

the shift of the *XMM-Newton* response, the overall $\chi^2_{red}$ of a combined fit should reach a minimum when the iron lines measured by both instruments coincide. Fig. 4.9 shows this attempt for the four observations. For obs4 both methods – the condition of iron line to be found at 6.4 keV as well as the best simultaneous fit – lead to a matrix shift of 25 lines (corresponding to about 125 eV). For all other observations the results are not so unambiguously. The shifts obtained for the both methods differ significantly (with up to a difference of 13 lines or 65 eV in obs3). This result shows that the applied method of a simple matrix shift cannot easily be used to correct for the CTE effects. At this point more work is needed to include all dependencies of the CTE into the calibration, which is beyond the scope of this thesis.

# Chapter 5

# The Relativistic Iron Line – Analysis

After its discovery in *EXOSAT* data in 1985 (Barr et al. 1985), the Fe K$\alpha$ line in Cyg X-1 has been studied intensively. These studies were of course always limited by the achievable energy resolution. Therefore in the first analysis by Barr et al. (1985) the line was not interpreted as having a relativistic line profile but rather explained as broadening of a narrow line due to Compton scattering in a moderately optically thick corona. In a reanalysis by Fabian et al. (1989), however, the same data were interpreted to show relativistic line broadening with the characteristic "double horned" features being smeared out due to the bad energy resolution of *EXOSAT* ($\sim 20\%@6\,\mathrm{keV}$, Peacock 1984).

Already in 1983 a weaker and narrower line was observed in Cyg X-1 with the *Tenma* satellite, but the results have been published only in 1990 by Kitamoto et al.. These authors claimed the line to originate from the surface of the companion star as also a dependence on the binary phase was observed. However, a broader component originating from the disk was not ruled out by the data.

This explanation by Kitamoto et al. (1990) was the only attempt to assign the iron line to the companion star. A new reanalysis of the *EXOSAT* data by Done et al. (1992) as well as observations by *BBXRT* (Marshall et al. 1993) and *ASCA* data (Ebisawa et al. 1996) were interpreted in terms of a narrow Gaussian line with additional edge component and reflection in the underlying continuum. A similar model was assumed by Gierliński et al. (1997) for simultaneous *Ginga* and *OSSE* data.

The idea of a broad line was reborn with new satellites with better energy resolution like *RXTE*, BeppoSAX, *Chandra*, or *XMM-Newton* (see, e.g., Gilfanov et al. 1999; Frontera et al. 2001a; Miller et al. 2002). The *Chandra* observations revealed that the line in fact is composed of a broad component (originating from the inner regions of the accretion disk) as well as of a narrow core (originating from the cooler outer parts of the disk). This conclusion was possible due to the good energy resolution which enabled Miller et al. (2002) to resolve both components clearly for the first time.

Table 5.1: Observational parameters for the *XMM-Newton* observations

| Observation | Date (MJD) | Effective Exposure EPIC-pn (ks) |
|---|---|---|
| obs1 | 53323.938 – 53324.139 | 17.076 |
| obs2 | 53329.923 – 53330.124 | 17.186 |
| obs3 | 53335.906 – 53336.135 | 19.456 |
| obs4 | 53341.891 – 53342.004 | 9.555 |

With the Modified Timing mode of *XMM-Newton* we obtained spectra with an even better signal to noise ratio and resolution than the *Chandra* data. The results of the analysis of these *XMM-Newton* observations are presented in this chapter.

## *5.1 Observations and data reduction*

As already mentioned in section 3.3, the *XMM-Newton* observations were executed simultaneously with the *INTEGRAL* and *RXTE* observations in November/December 2004. Table 5.1 summarizes the key parameters. As the observations were carried out in the Modified Timing mode, there are no EPIC-MOS but only EPIC-pn, RGS, and OM data. Data from the latter two instruments have not been analyzed in this thesis, therefore no detailed information is given about them. For all four observations the "thick" filter was used.

The data have been extracted using SAS 7.0.0. To avoid problems due to pile-up in the center of the point spread function, we excluded the innermost three CCD columns (numbers 36–38) from the extraction. The response matrix for the Modified Timing mode has been calculated as outlined in the previous section, taking care of the special extraction region used. Due to the increased lower threshold of 2.8 keV used for the Modified Timing mode and the shape of the energy dependent effective area, the *XMM-Newton* spectra have been analyzed in the 3.5–9.5 keV range.

## *5.2 Structure of the line*

Contrary to Seyfert AGN (in which the continuum can be described by a simple power-law throughout the X-ray band and only in some cases a soft excess is observed), the soft X-ray spectrum of galactic black holes is known to be rather complex. This is due to the fact that the disk as well as the non-thermal corona can contribute – depending on the state – to a different extent. So besides the

line which itself can be composed of a broad component as well as a narrow component , also the continuum must be modeled as a combination of a black body, power-law, and reflection component as it has been outlined in Chapter 3. The main aim of this chapter, however, is the analysis of the structure of the Fe K complex, so there are a couple of questions to be addressed in the following concerning this topic:

- Does the line consist of a broad and a narrow component?
- Is the Fe K absorption edge, which is expected to accompany the fluorescent line, seen in the spectrum?
- Might the data even be explained without an relativistic line but with a narrow line plus smeared edge only as it had been suggested previously?
- Is the broad line – if existing – best described by the `laor` or the `diskline` model, and what are the conclusion for the spin of Cyg X-1?
- How do the new results compare to previous line studies, e.g., by the *Chandra* satellite (Miller et al. 2002)?

### *5.2.1 Composition of the XSPEC model*

To answer the question if the line is indeed composed of a broad and a narrow component we started the analysis first with a simple absorbed power-law and disk black body[1] fit to the data outside the 5–8 keV range, as it is shown in Fig. 5.1a for the second *XMM-Newton* observation. This fit reveals strong residuals in the Fe K$\alpha$ region ($\chi^2_{\rm red} \approx 35$ / 84 dof). Adding a narrow line (with $\sigma = 50$ eV fixed in all models described in this chapter) only to model the Fe K$\alpha$ fluorescence line, as shown in panel b, improves the residuals but the fit is still far from being acceptable with $\chi^2_{\rm red} = 7.9$. Only after adding a relativistically broadened line, the data are described satisfactorily with $\chi^2_{\rm red} = 1.9$ (Fig. 5.1c).

We therefore decided to fit all four *XMM-Newton* observations with a model composed of the *XSPEC* models `phabs`, `diskbb`, `powerlaw`, `gaussian`, and `diskline` / `laor`. The results of these fits are listed in Tables 5.2 and 5.3. All fits gave acceptable $\chi^2_{\rm red}$ in the range of 1.95 (obs2) – 1.41 (obs4) for the `diskline` model and 2.20 (obs1) – 1.53 (obs4) for the `laor` model respectively. However, there are still structures left in the residuals as shown in the upper panel of Fig. 5.2. Adding a smeared edge component (*XSPEC* model `smedge` (Ebisawa et al. 1994), see Tables 5.4 and 5.5) clearly improves this situation with $\chi^2_{\rm red}$decreasing for all

[1] For the disk black body the multicolor model `diskbb` was used (Mitsuda et al. 1984; Makishima et al. 1986).

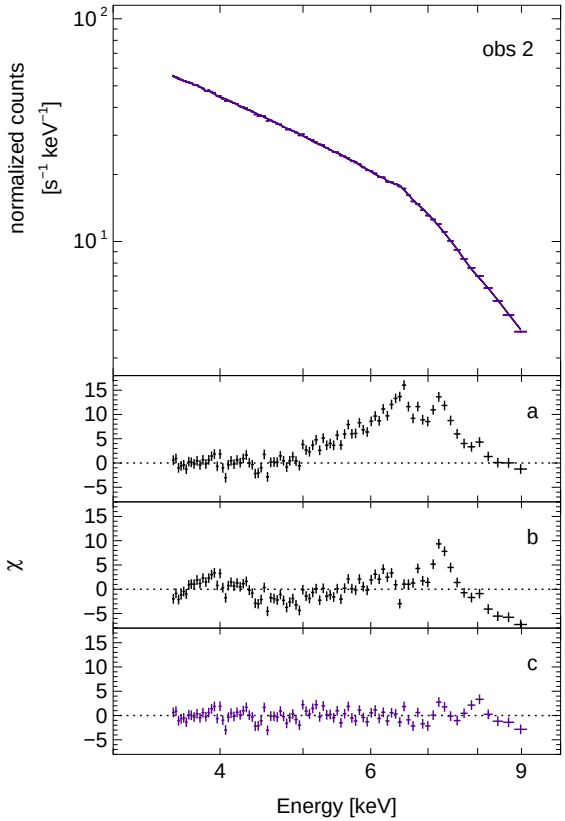


Figure 5.1: Fit to the obs2 *XMM-Newton* data. `a:` Power-law fit to the data outside the 5–8 keV band. There are strong residuals remaining in the Fe K$\alpha$ region. `b:` Fit to the whole band using a power-law and a narrow gaussian line. `c:` Fit to the whole band using a power-law, a narrow line, and a relativistic line (using the `diskline` model).

single observations to 1.82 (obs1) – 1.40 (obs4) for the `diskline` fits and 1.79 (obs3) – 1.42 (obs4) for the `laor` fits. The residuals for the `diskline` model with additional `smedge` component are shown in the lower panel of Fig. 5.2. Hence only the models including the edge are discussed in the following.

The energy of the narrow core of the iron line is very well constrained in all observations as it is independent of the model used for the broad component. It is found to have an energy of 6.51 – 6.58 keV. Note, however, that due to the over-correction of the CTE effects, these values must be taken with an intrinsic error of 0.15–0.2 keV, such that the corrected values are consistent with 6.4 keV, i.e., neutral or only moderately ionized iron. The energy of the broad line, however, shows a dependency on the model even though the uncertainties are significantly larger (especially for the `laor` fits). In all observations but obs3 the energy found

Table 5.2: Fits using the `diskline` model. $\sigma_{\mathrm{K}\alpha,\mathrm{narr}}$ has been fixed to 50 eV.

| | **obs1** | **obs2** | **obs3** | **obs4** |
|---|---|---|---|---|
| $N_{\mathrm{H}}$ $[10^{22}\mathrm{cm}^{-2}]$ | $0.13^{+0.20}_{-0.13}$ | $0.65^{+0.19}_{-0.33}$ | $0.61^{+0.21}_{-0.11}$ | $0.36^{+0.20}_{-0.20}$ |
| $kT_{\mathrm{in}}$ [keV ] | $0.081^{+0.001}_{-0.008}$ | $0.013^{+0.175}_{-0.013}$ | $0.099^{+0.009}_{-0.008}$ | $0.017^{+0.132}_{-0.017}$ |
| $\mathrm{norm}_{\mathrm{bb}}$ | $\left(1.6^{+3.1}_{-1.2}\right)10^{19}$ | $\left(5.2^{+\infty}_{-5.2}\right)10^{7}$ | $\left(4.0^{+2.3}_{-2.0}\right)10^{15}$ | $\left(1.3^{+\infty}_{-1.3}\right)10^{9}$ |
| $\Gamma$ | $2.10^{+0.02}_{-0.02}$ | $1.96^{+0.02}_{-0.02}$ | $1.97^{+0.02}_{-0.01}$ | $1.93^{+0.02}_{-0.02}$ |
| $\mathrm{norm}_{\mathrm{pl}}$ | $1.67^{+0.06}_{-0.05}$ | $0.88^{+0.03}_{-0.04}$ | $1.30^{+0.06}_{-0.05}$ | $1.27^{+0.05}_{-0.05}$ |
| $E_{\mathrm{K}\alpha,\mathrm{narr}}$ [keV ] | $6.58^{+0.02}_{-0.02}$ | $6.52^{+0.03}_{-0.03}$ | $6.51^{+0.04}_{-0.03}$ | $6.56^{+0.02}_{-0.02}$ |
| $\mathrm{norm}_{\mathrm{K}\alpha,\mathrm{narr}}$ $[10^{-4}]$ | $3.9^{+0.7}_{-1.0}$ | $1.9^{+0.6}_{-0.5}$ | $1.7^{+0.7}_{-0.7}$ | $4.9^{+0.9}_{-1.2}$ |
| $E_{\mathrm{K}\alpha,\mathrm{diskl}}$ [keV ] | $6.21^{+0.06}_{-0.06}$ | $5.99^{+0.05}_{-0.05}$ | $6.08^{+0.06}_{-0.02}$ | $6.10^{+0.11}_{-0.09}$ |
| $\mathrm{norm}_{\mathrm{K}\alpha,\mathrm{diskl}}$ $[10^{-3}]$ | $8.2^{+0.5}_{-0.4}$ | $5.3^{+0.3}_{-0.3}$ | $7.1^{+0.3}_{-0.4}$ | $7.1^{+0.5}_{-0.6}$ |
| $\beta$ | $2.65^{+0.06}_{-0.06}$ | $2.75^{+0.04}_{-0.07}$ | $2.62^{+0.06}_{-0.06}$ | $2.69^{+0.09}_{-0.07}$ |
| $i$ [deg] | $75.3^{+7.1}_{-4.2}$ | $90.0^{+0.0}_{-8.7}$ | $90.0^{+0.0}_{-8.2}$ | $90.0^{+0.0}_{-10.5}$ |
| $\chi^2_{\mathrm{red}}$/dof | 1.856 / 78 | 1.950 / 78 | 1.895 / 78 | 1.411 / 78 |

Table 5.3: Fits using the `laor` model. $\sigma_{\mathrm{K}\alpha,\mathrm{narr}}$ has been fixed to 50 eV.

| | **obs1** | **obs2** | **obs3** | **obs4** |
|---|---|---|---|---|
| $N_{\mathrm{H}}$ [$10^{22}\mathrm{cm}^{-2}$] | $1.75^{+0.52}_{-0.49}$ | $1.23^{+0.46}_{-0.41}$ | $1.12^{+0.18}_{-0.16}$ | $0.68^{+0.26}_{-0.25}$ |
| $kT_{\mathrm{in}}$ [keV ] | $0.337^{+0.012}_{-0.013}$ | $0.247^{+0.016}_{-0.247}$ | $0.107^{+0.001}_{-0.002}$ | $0.094^{+0.002}_{-0.094}$ |
| $\mathrm{norm}_{\mathrm{bb}}$ | $\left(1.0^{+5.5}_{-0.9}\right)10^{5}$ | $\left(7.4^{+940}_{-7.4}\right)10^{5}$ | $\left(4.9^{+62}_{-4.9}\right)10^{14}$ | $\left(1.5^{+6.3}_{-1.5}\right)10^{16}$ |
| $\Gamma$ | $2.16^{+0.02}_{-0.02}$ | $1.99^{+0.03}_{-0.03}$ | $2.01^{+0.02}_{-0.01}$ | $1.94^{+0.02}_{-0.02}$ |
| $\mathrm{norm}_{\mathrm{pl}}$ | $1.96^{+0.10}_{-0.11}$ | $0.95^{+0.05}_{-0.05}$ | $1.41^{+0.03}_{-0.04}$ | $1.33^{+0.06}_{-0.06}$ |
| $E_{\mathrm{K}\alpha,\mathrm{narr}}$ [keV ] | $6.52^{+0.06}_{-0.03}$ | $6.53^{+0.03}_{-0.02}$ | $6.13^{+0.06}_{-0.07}$ | $6.58^{+0.03}_{-0.04}$ |
| $\mathrm{norm}_{\mathrm{K}\alpha,\mathrm{narr}}$ [$10^{-4}$] | $3.3^{+0.9}_{-0.8}$ | $2.7^{+82}_{-0.4}$ | $1.2^{+0.6}_{-0.7}$ | $5.2^{+0.8}_{-1.5}$ |
| $E_{\mathrm{K}\alpha,\mathrm{laor}}$ [keV ] | $6.32^{+0.06}_{-0.10}$ | $5.90^{+0.04}_{-0.04}$ | $6.14^{+0.04}_{-0.04}$ | $6.05^{+0.08}_{-0.11}$ |
| $\mathrm{norm}_{\mathrm{K}\alpha,\mathrm{laor}}$ [$10^{-3}$] | $6.9^{+0.3}_{-0.3}$ | $4.9^{+8.2}_{-0.4}$ | $6.6^{+0.5}_{-0.4}$ | $6.7^{+8.2}_{-0.5}$ |
| $\beta$ | $2.26^{+0.04}_{-0.05}$ | $2.28^{+0.06}_{-0.11}$ | $2.13^{+0.04}_{-0.04}$ | $2.21^{+0.07}_{-0.08}$ |
| $i$ [deg] | $59.1^{+2.1}_{-0.8}$ | $67.4^{+2.6}_{-2.0}$ | $64.5^{+1.2}_{-1.3}$ | $65.6^{+2.4}_{-0.8}$ |
| $\chi^2_{\mathrm{red}}$/dof | 2.199 / 78 | 1.893 / 78 | 1.962 / 78 | 1.532 / 78 |

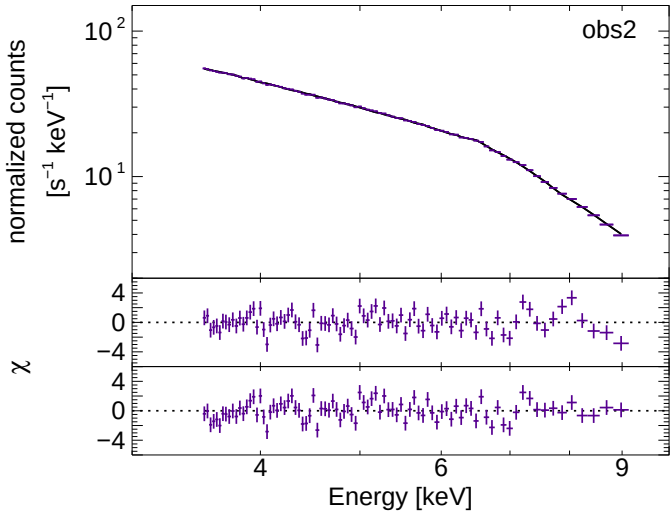


Figure 5.2: `diskline` fit to *XMM-Newton* obs2. The upper panel shows the residuals to a fit without an edge component, the lower lower panel the residuals if a `smedge` component is added to the model.

using the `laor` model is smaller than in the `diskline` fits. Overall the energy of the broad line tends to be unphysically low in all fits (a behavior that was already observed in *Chandra* observations by Miller et al. 2002). For the energy of the edge only obs1 shows a discrepancy between the `diskline` and `laor` value, while the other three observations are model independent. The smearing width of the edge could not be constrained in our fits due to the limited energy range of the *XMM-Newton* data, therefore it was kept fixed to 7 keV in all models (see, e.g., Miller et al. 2002, and references therein).

However, while the line parameters are still quite well constrained in these fits, the situation is different for the continuum parameters: besides from being consistent with 0 in half of the fits (namely obs2 and obs4), most temperatures found for the black body component show large uncertainties in general. The normalization of the `diskbb` component shows extreme variations with also huge uncertainties. Therefore it must be stated that the black body component cannot be constrained with *XMM-Newton*. This is most probably due to the high lower threshold of 3.5 keV. As the performance of the black body influences the determination of all continuum parameters, we decided to derive the continuum using our simultaneous *RXTE* observations before trying to answer the question "`diskline` or `laor`?" in the following section.

Table 5.4: Fits using the `diskline` model and a smeared edge. $\sigma_{\mathrm{K}\alpha,\mathrm{narr}}$ has been fixed to 50 eV.

| | **obs1** | **obs2** | **obs3** | **obs4** |
|---|---|---|---|---|
| $N_{\mathrm{H}}$ [$10^{22}\mathrm{cm}^{-2}$] | $0.00^{+0.04}_{-0.00}$ | $0.00^{+0.18}_{-0.00}$ | $0.03^{+0.29}_{-0.03}$ | $0.00^{+0.38}_{-0.00}$ |
| $kT_{\mathrm{in}}$ [keV ] | $0.070^{+0.001}_{-0.001}$ | $0.013^{+0.176}_{-0.013}$ | $0.098^{+0.002}_{-0.008}$ | $0.017^{+0.153}_{-0.017}$ |
| $\mathrm{norm}_{\mathrm{bb}}$ | $\left(3.5^{+0.5}_{-2.7}\right)10^{22}$ | $\left(4.6^{+\infty}_{-4.6}\right)10^{7}$ | $\left(4.1^{+3.9}_{-3.8}\right)10^{15}$ | $\left(1.1^{+\infty}_{-1.1}\right)10^{9}$ |
| $\Gamma$ | $2.05^{+0.03}_{-0.02}$ | $1.82^{+0.07}_{-0.03}$ | $1.85^{+0.06}_{-0.03}$ | $1.80^{+0.03}_{-0.02}$ |
| $\mathrm{norm}_{\mathrm{pl}}$ | $1.55^{+0.03}_{-0.03}$ | $0.69^{+0.03}_{-0.02}$ | $1.05^{+0.02}_{-0.03}$ | $1.05^{+0.04}_{-0.03}$ |
| $E_{\mathrm{K}\alpha,\mathrm{narr}}$ [keV ] | $6.58^{+0.03}_{-0.03}$ | $6.52^{+0.03}_{-0.03}$ | $6.51^{+0.03}_{-0.03}$ | $6.56^{+0.04}_{-0.05}$ |
| $\mathrm{norm}_{\mathrm{K}\alpha,\mathrm{narr}}$ [$10^{-4}$] | $3.8^{+0.8}_{-0.9}$ | $2.5^{+0.6}_{-0.6}$ | $2.8^{+0.7}_{-0.7}$ | $3.4^{+1.1}_{-1.4}$ |
| $E_{\mathrm{K}\alpha,\mathrm{diskl}}$ [keV ] | $6.24^{+0.05}_{-0.03}$ | $5.90^{+0.10}_{-0.04}$ | $6.01^{+0.08}_{-0.06}$ | $6.34^{+0.08}_{-0.08}$ |
| $\mathrm{norm}_{\mathrm{K}\alpha,\mathrm{diskl}}$ [$10^{-3}$] | $6.5^{+1.2}_{-0.8}$ | $2.9^{+0.3}_{-0.9}$ | $4.2^{+1.6}_{-1.4}$ | $2.6^{+1.0}_{-0.8}$ |
| $\beta$ | $2.64^{+0.07}_{-0.07}$ | $2.62^{+0.12}_{-0.22}$ | $2.44^{+0.10}_{-0.13}$ | $2.20^{+0.16}_{-0.22}$ |
| $i$ [deg] | $63.8^{+7.9}_{-4.1}$ | $76.5^{+13.5}_{-8.9}$ | $90.0^{+0.0}_{-19.5}$ | $55.4^{+34.6}_{-5.7}$ |
| $E_{\mathrm{edge}}$ [keV ] | $7.81^{+0.30}_{-0.08}$ | $7.36^{+0.09}_{-0.12}$ | $7.31^{+0.16}_{-0.11}$ | $7.35^{+0.20}_{-0.19}$ |
| $\tau_{\mathrm{edge}}$ | $0.37^{+0.13}_{-0.20}$ | $0.81^{+0.19}_{-0.08}$ | $0.64^{+0.22}_{-0.13}$ | $0.75^{+0.14}_{-0.50}$ |
| $\chi^2_{\mathrm{red}}$/dof | 1.821 / 76 | 1.543 / 76 | 1.706 / 76 | 1.402 / 76 |

Table 5.5: Fits using the `laor` model and a smeared edge. $\sigma_{\mathrm{K}\alpha,\mathrm{narr}}$ has been fixed to 50 eV.

| | **obs1** | **obs2** | **obs3** | **obs4** |
|---|---|---|---|---|
| $N_{\mathrm{H}}$ $[10^{22}\mathrm{cm}^{-2}]$ | $1.03^{+0.36}_{-0.51}$ | $1.89^{+0.56}_{-0.89}$ | $0.01^{+0.41}_{-0.01}$ | $0.21^{+0.30}_{-0.21}$ |
| $kT_{\mathrm{in}}$ [keV ] | $0.697^{+0.115}_{-0.012}$ | $0.279^{+0.026}_{-0.279}$ | $0.075^{+0.001}_{-0.001}$ | $0.091^{+0.005}_{-0.091}$ |
| $\mathrm{norm}_{\mathrm{bb}}$ | $\left(6.9^{+2.7}_{-0.7}\right)10^{2}$ | $\left(9.2^{+1200}_{-9.2}\right)10^{4}$ | $\left(4.0^{+25}_{-3.0}\right)10^{20}$ | $\left(1.5^{+240}_{-1.5}\right)10^{16}$ |
| $\Gamma$ | $1.53^{+0.08}_{-0.08}$ | $1.94^{+0.03}_{-0.16}$ | $1.82^{+0.07}_{-0.02}$ | $1.86^{+0.02}_{-0.05}$ |
| $\mathrm{norm}_{\mathrm{pl}}$ | $0.60^{+0.03}_{-0.09}$ | $0.86^{+0.04}_{-0.19}$ | $1.00^{+0.03}_{-0.02}$ | $1.16^{+0.03}_{-0.10}$ |
| $E_{\mathrm{K}\alpha,\mathrm{narr}}$ [keV ] | $6.55^{+0.02}_{-0.02}$ | $6.53^{+0.03}_{-0.02}$ | $6.54^{+0.04}_{-0.04}$ | $6.57^{+0.03}_{-0.04}$ |
| $\mathrm{norm}_{\mathrm{K}\alpha,\mathrm{narr}}$ $[10^{-4}]$ | $3.9^{+0.7}_{-1.0}$ | $2.9^{+0.6}_{-0.9}$ | $1.4^{+2.0}_{-1.0}$ | $5.5^{+1.1}_{-1.4}$ |
| $E_{\mathrm{K}\alpha,\mathrm{laor}}$ [keV ] | $5.93^{+0.19}_{-0.04}$ | $5.87^{+0.12}_{-0.08}$ | $6.10^{+0.07}_{-0.18}$ | $6.02^{+0.10}_{-0.09}$ |
| $\mathrm{norm}_{\mathrm{K}\alpha,\mathrm{laor}}$ $[10^{-3}]$ | $7.3^{+1.8}_{-2.0}$ | $4.2^{+0.5}_{-2.6}$ | $3.1^{+8.8}_{-1.0}$ | $5.0^{+2.3}_{-1.5}$ |
| $\beta$ | $4.38^{+0.32}_{-1.13}$ | $2.25^{+0.06}_{-0.23}$ | $1.84^{+0.27}_{-0.31}$ | $2.20^{+0.09}_{-0.13}$ |
| $i$ [deg] | $53.1^{+0.8}_{-0.8}$ | $66.7^{+1.7}_{-2.8}$ | $65.9^{+3.7}_{-3.1}$ | $62.9^{+2.6}_{-3.1}$ |
| $E_{\mathrm{edge}}$ [keV ] | $7.27^{+0.03}_{-0.04}$ | $7.96^{+0.20}_{-0.86}$ | $7.17^{+0.11}_{-0.12}$ | $7.66^{+0.19}_{-0.31}$ |
| $\tau_{\mathrm{edge}}$ | $1.88^{+0.07}_{-0.04}$ | $0.52^{+0.15}_{-0.15}$ | $0.84^{+0.15}_{-0.30}$ | $0.46^{+0.20}_{-0.17}$ |
| $\chi^2_{\mathrm{red}}$/dof | 1.555 / 76 | 1.542 / 76 | 1.791 / 76 | 1.416 / 76 |

#### *5.2.1.1 `diskline` or `laor`?*

To constrain the continuum parameters, the simultaneous *RXTE* data of the four observations have been fitted independently of the *XMM-Newton* data. Afterwards the continuum parameters were kept fixed when fitting the *XMM-Newton* data. This approach was necessary as due to the over-correction of the CTE effects the *XMM-Newton* spectra are shifted to slightly higher energies making a joint fit rather difficult[2]. Another advantage of the extended energy range of *RXTE* is the possibility to include the reflection component into the model, as the reflection hump is expected to extend down to energies in the Fe K$\alpha$ regime. In principle the inclusion of the `reflect` model would make an additional edge component redundant, as the reflection intrinsically includes an edge. When modeling the data, however, it turned out that the "`reflect` edge" is too sharp to describe the data properly ($\chi^2_{\rm red}$of the order of 2.5). We therefore included an additional `smedge` also in these models. In Tables 5.6 and 5.7 the best fit parameters are listed with the fixed *RXTE* parameters printed in italics.

As expected, the black body component is now much better constrained with temperatures in the 0.61 – 0.88 keV range and a normalization independent of the relativistic line model used. However, it is still not necessarily needed in obs2 and obs4. Also the normalization of the power law component is in principle independent of the line model, with a minimal discrepancy for obs2.

Like in the *XMM-Newton* only fits, the energy of the narrow core of the iron line is very well constrained for all observations between 6.51 and 6.60 keV. The energy of the broad line on the other hand is found to vary rather strong with $\Delta E = 0.27$ for the `diskline` model and $\Delta E = 0.18$ for `laor` [3]. The energy value itself is in all observations lower than in the respective `diskline` fits (although the values of obs1 and obs4 might be consistent due to the large uncertainties of the energy in the `laor` model). Also the equivalent width of the broad line is found to be smaller in the when using the `laor` model.

While the width of the `smedge` component was again kept fixed to 7 keV, its energy shows very little variation in the `laor` fits with values between 7.57 – 7.74 keV (which is consistent within the error-bars). For the `diskline` fits the scatter is larger with energies ranging from 7.33 keV to 8.00 keV. When comparing the two models, however, only in obs1 the values are not consistent when applying the uncertainty ranges. A similar scenario holds true for $\tau$, which only in obs4 is not model independently constrained.

Overall, all fits gave a comparable good description of the data, with $\chi^2_{\rm red}$ rang-

[2] We tried to model the shift by the `gain` function of *XSPEC* but without convincing results.

[3] It must be noted that the energy of the broad line could not really be constrained in the `laor` fit to obs2. We therefore set the lower limit to 5.80 keV.

ing from 1.78 (obs1) – 1.39 (obs4) for the `diskline` model and 1.85 (obs2) – 1.38 (obs4) for the `laor` model. It is therefore impossible to reject one of the two models on basis of the $\chi^2_{\rm red}$ (in fact, the `diskline` model gives a better description of obs1 – obs3 while obs4 is slightly better described by the `laor` model). The only significant difference found in both models, which might help to solve this issue, is the inclination found in the respective best fits. While it ranges around 67° for the `laor` fits, it approaches the upper limit of 90° in the `diskline` model. Before it is possible to compare these results with literature values, a more in depth consideration of the geometry of Cygnus X-1 must be made.

The question of the inclination angle in Cyg X-1 is not simply restricted to the orbital inclination *i* of the system: Pooley et al. (1999) first reported the detection of a super-orbital period of ∼150 d in the radio data of Cyg X-1. From thereon this period was also observed in X-rays (e.g., Brocksopp et al. 1999a; Benlloch et al. 2004; Lachowicz et al. 2006; Ibragimov et al. 2007). The generally accepted explanation for the 150 d modulation is precession of the accretion disk, which is tilted by an amount $\delta$ with respect to the orbital plane (Brocksopp et al. 1999a). The angle $\theta$ under which the disk is seen by the observer is hence given by

$$\cos\theta = -\sin i \sin\delta \cos\Phi + \cos i \cos\delta \tag{5.1}$$

with $\Phi$ being the super-orbital phase (see also Lachowicz et al. 2006; Ibragimov et al. 2007)[4]. At super-orbital phase $\Phi$=0 the disk is most inclined with respect to the observer, as

$$\theta = -\sin i \sin\delta + \cos i \cos\delta = \cos(i+\delta) = i+\delta \quad . \tag{5.2}$$

The opposite case occurs at super-orbital phase $\Phi$=0.5, where the disk inclination is smallest:

$$\theta = \sin i \sin\delta + \cos i \cos\delta = \cos(i-\delta) = |i-\delta| \quad . \tag{5.3}$$

Following Ibragimov et al. (2007) and assuming $30° \leq i \leq 45°$ and $8° \leq \delta \leq 22°$ as found by these authors, $\theta$ should vary between 8° and 67° (for the most extreme combinations of parameters) depending on orbital phase. A more detailed calculation for our four *XMM-Newton* observations yields values of $37° \leq \theta \leq 66°$, as the observations were taken during super-orbital phases 0.374–0.493 (see also Table 5.8).

Comparing these theoretical values with the fit results, the inclination found by the `diskline` model can be ruled out on physical grounds. In contrast the `laor` results are consistent with the theoretical allowed region for obs1 and obs4, while

[4]Note that this relation does not directly depend on the orbital phase as it describes the disk inclination in an inertial frame, i.e., the precession is independent of the orbital motion.

Table 5.6: Fits using the `diskline` model and a smeared edge with the continuum parameters fixed to *RXTE* values. $\sigma_{\mathrm{K}\alpha,\mathrm{narr}}$ has been fixed to 50 eV.

| | **obs1** | **obs2** | **obs3** | **obs4** |
|---|---|---|---|---|
| $N_{\mathrm{H}}$ [$10^{22}\mathrm{cm}^{-2}$] | *0.15* | *0.00* | *0.30* | *0.03* |
| $kT_{\mathrm{in}}$ [keV ] | *0.61* | *0.81* | *0.88* | *0.69* |
| $\mathrm{norm}_{\mathrm{bb}}$ | $350.0^{+34.0}_{-35.0}$ | $0.0^{+1.0}_{-0.0}$ | $12.0^{+6.0}_{-2.0}$ | $0.0^{+25.0}_{-0.0}$ |
| $\Gamma$ | *2.00* | *1.90* | *1.89* | *1.87* |
| $\mathrm{norm}_{\mathrm{pl}}$ | $1.350^{+0.008}_{-0.008}$ | $0.759^{+0.002}_{-0.002}$ | $1.104^{+0.013}_{-0.012}$ | $1.148^{+0.002}_{-0.012}$ |
| $\Omega/2\pi$ | *0.68* | *0.57* | *0.53* | *0.49* |
| $E_{\mathrm{K}\alpha,\mathrm{narr}}$ [keV ] | $6.57^{+0.02}_{-0.02}$ | $6.51^{+0.03}_{-0.03}$ | $6.51^{+0.03}_{-0.03}$ | $6.56^{+0.02}_{-0.02}$ |
| $\mathrm{norm}_{\mathrm{K}\alpha,\mathrm{narr}}$ [$10^{-4}$] | $4.2^{+0.8}_{-0.9}$ | $1.8^{+0.8}_{-0.5}$ | $2.3^{+0.6}_{-0.3}$ | $5.2^{+0.8}_{-1.2}$ |
| $E_{\mathrm{K}\alpha,\mathrm{diskl}}$ [keV ] | $6.15^{+0.09}_{-0.08}$ | $5.88^{+0.04}_{-0.03}$ | $6.01^{+0.04}_{-0.05}$ | $6.07^{+0.10}_{-0.08}$ |
| $\mathrm{norm}_{\mathrm{K}\alpha,\mathrm{diskl}}$ [$10^{-3}$] | $4.6^{+0.6}_{-0.6}$ | $4.9^{+0.2}_{-0.2}$ | $5.3^{+8.4}_{-0.9}$ | $5.2^{+0.8}_{-0.4}$ |
| equivalent width [eV] | 134 | 196 | 148 | 137 |
| $\beta$ | $2.63^{+0.11}_{-0.12}$ | $2.78^{+0.04}_{-0.06}$ | $2.54^{+0.09}_{-0.05}$ | $2.61^{+0.12}_{-0.11}$ |
| $i$ [deg] | $87.1^{+2.9}_{-14.8}$ | $90.0^{+0.0}_{-8.5}$ | $90.0^{+0.0}_{-11.7}$ | $88.5^{+1.4}_{-12.3}$ |
| $E_{\mathrm{edge}}$ [keV ] | $7.33^{+0.08}_{-0.08}$ | $8.00^{+0.12}_{-0.15}$ | $7.53^{+0.21}_{-0.15}$ | $7.36^{+0.48}_{-0.24}$ |
| $\tau_{\mathrm{edge}}$ | $0.71^{+0.08}_{-0.07}$ | $0.54^{+0.12}_{-0.12}$ | $0.45^{+0.07}_{-0.06}$ | $0.35^{+0.05}_{-0.10}$ |
| $\chi^2_{\mathrm{red}}$/dof | 1.777 / 79 | 1.685 / 79 | 1.764 / 79 | 1.388 / 79 |

Table 5.7: Fits using the `laor` model and a smeared edge with the continuum parameters fixed to *RXTE* values. $\sigma_{\mathrm{K}\alpha,\mathrm{narr}}$ has been fixed to 50 eV.

| | **obs1** | **obs2** | **obs3** | **obs4** |
|---|---|---|---|---|
| $N_{\mathrm{H}}$ [$10^{22}\mathrm{cm}^{-2}$] | *0.15* | *0.00* | *0.30* | *0.03* |
| $kT_{\mathrm{in}}$ [keV ] | *0.61* | *0.81* | *0.88* | *0.69* |
| $\mathrm{norm}_{\mathrm{bb}}$ | $346.0^{+50.0}_{-41.0}$ | $0.0^{+1.0}_{-0.0}$ | $19.0^{+5.0}_{-7.0}$ | $9.0^{+19.0}_{-9.0}$ |
| $\Gamma$ | *2.00* | *1.90* | *1.89* | *1.87* |
| $\mathrm{norm}_{\mathrm{pl}}$ | $1.347^{+0.011}_{-0.012}$ | $0.754^{+0.002}_{-0.002}$ | $1.079^{+0.014}_{-0.010}$ | $1.132^{+0.006}_{-0.008}$ |
| $\Omega/2\pi$ | *0.68* | *0.57* | *0.53* | *0.49* |
| $E_{\mathrm{K}\alpha,\mathrm{narr}}$ [keV ] | $6.60^{+0.03}_{-0.02}$ | $6.52^{+0.03}_{-0.02}$ | $6.50^{+0.03}_{-0.02}$ | $6.56^{+0.02}_{-0.02}$ |
| $\mathrm{norm}_{\mathrm{K}\alpha,\mathrm{narr}}$ [$10^{-4}$] | $5.1^{+0.8}_{-2.2}$ | $2.9^{+0.5}_{-0.6}$ | $3.6^{+0.6}_{-0.9}$ | $5.4^{+0.9}_{-1.3}$ |
| $E_{\mathrm{K}\alpha,\mathrm{laor}}$ [keV ] | $5.95^{+0.24}_{-0.22}$ | $5.80^{+0.04*}_{-0.00}$ | $5.83^{+0.11}_{-0.06}$ | $5.98^{+0.09}_{-0.10}$ |
| $\mathrm{norm}_{\mathrm{K}\alpha,\mathrm{laor}}$ [$10^{-3}$] | $4.6^{+1.1}_{-1.5}$ | $3.8^{+0.3}_{-0.2}$ | $4.7^{+0.9}_{-1.0}$ | $3.6^{+0.8}_{-0.6}$ |
| equivalent width [eV] | 129 | 155 | 134 | 97 |
| $\beta$ | $2.29^{+0.07}_{-0.15}$ | $2.19^{+0.05}_{-0.06}$ | $2.11^{+0.06}_{-0.10}$ | $2.17^{+0.11}_{-0.16}$ |
| $i$ [deg] | $64.7^{+4.9}_{-6.1}$ | $68.1^{+0.7}_{-1.1}$ | $69.3^{+3.2}_{-2.3}$ | $64.6^{+6.8}_{-3.1}$ |
| $E_{\mathrm{edge}}$ [keV ] | $7.57^{+0.09}_{-0.11}$ | $7.74^{+0.16}_{-0.17}$ | $7.59^{+0.15}_{-0.38}$ | $7.59^{+0.15}_{-0.43}$ |
| $\tau_{\mathrm{edge}}$ | $0.80^{+0.11}_{-0.08}$ | $0.63^{+0.12}_{-0.10}$ | $0.56^{+0.10}_{-0.09}$ | $0.60^{+0.10}_{-0.14}$ |
| $\chi^2_{\mathrm{red}}$/dof | 1.810 / 79 | 1.847 / 79 | 1.837 / 79 | 1.382 / 79 |

* parameter could not be constrained so lower limit was set to 5.80 keV

Table 5.8: Predictions for the disk viewing angle $\theta$. The minimum value is obtained with $i = 30°$ and $\delta = 8°$ while the maximum value follows from $i = 45°$ and $\delta = 22°$.

| Observation | $\Phi$ | $\theta_{\rm min}$ | $\theta_{\rm max}$ |
|---|---|---|---|
| obs1 | 0.374 – 0.375 | $37\overset{\circ}{.}5$ | $65\overset{\circ}{.}9$ |
| obs2 | 0.413 – 0.415 | $37\overset{\circ}{.}4$ | $65\overset{\circ}{.}5$ |
| obs3 | 0.453 – 0.454 | $37\overset{\circ}{.}4$ | $65\overset{\circ}{.}3$ |
| obs4 | 0.492 – 0.493 | $37\overset{\circ}{.}3$ | $65\overset{\circ}{.}0$ |

they are slightly above it for obs2 and obs3. We therefore calculated confidence contours for these two cases. Fig. 5.3 shows the confidence contours for the inclination and disk emissivity index. For both observations the 99% contour of the `laor` model reaches the theoretical predicted region for the inclination. To further constrain the assertion that Kerr models yield a better description of the *XMM-Newton* data we decided to try another approach of modeling the overall spectrum and fit the data using the convolution model `kdblur`.

### *5.2.2 Another way of doing it:* `kdblur`

In the two models described up to now, the relativistic line was modeled separate from the continuum. A physically more appropriate description, however, demands a blurring of the reflection continuum *and* the line as they are both exposed to the strong gravitational field of the black hole. This was done using the `kdblur` model (Fabian et al. 2002). Due to the smoothing of the reflection

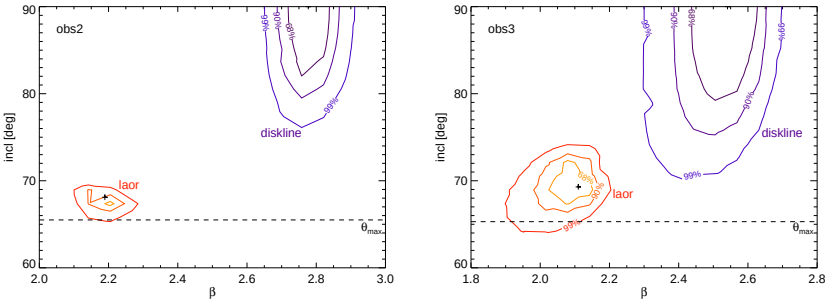


Figure 5.3: Confidence contours for the inclination and disk emissivity index of obs2 (left) and obs3 (right). Only the 99% contour of the `laor` model reaches the theoretically predicted region for the inclination.

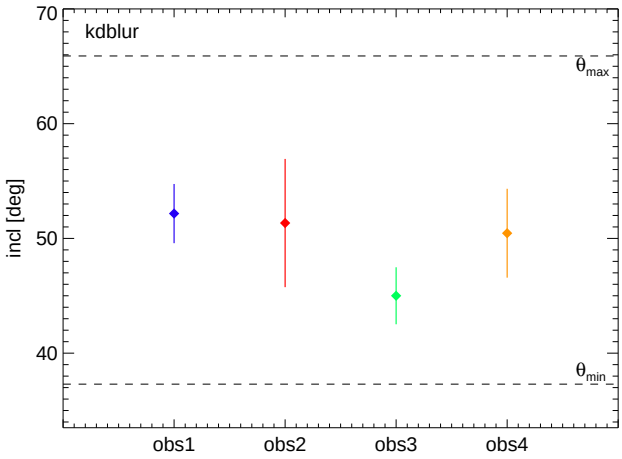


Figure 5.4: Inclinations found using the `kdblur` model. All four values are within the allowed region.

component, the edge "included" in `reflect` is able to account for the observed structures in the residuals of Cyg X-1, hence no additional edge component is needed. As the energy of the broad line (which in this case is modeled as a simple Gaussian which is blurred via `kdblur`) could not be constrained it was fixed to the energy of the narrow line.

Table 5.9 lists the results of the fits. The quality of the fits in terms of $\chi^2_{\rm red}$ is comparable to those of the `diskline` / `laor` fits, for obs2 the `kdblur` model even provides the best description of the three models. While the normalization of the black body has increased compared to the `diskline` / `laor` fits, the normalization of the power-law has decreased. The energy of the line is consistent with the energy of the narrow core found in the `diskline` / `laor` fits. In the parameters describing the disk, $\beta$ and $i$, are the largest differences found: with values of the order of 4 (respective 3 in obs3), $\beta$ is significantly larger in the `kdblur` fits, i.e., the disk emissivity profile is much steeper. The inclination is found between 45° and 52.°2 and hence within the allowed range calculated for $\theta$ for all observations as shown in Fig. 5.4.

Table 5.9: Fits using the `kdblur` model. $\sigma_{\mathrm{K}\alpha,\mathrm{narr}}$ has been fixed to 50 eV.

| | **obs1** | **obs2** | **obs3** | **obs4** |
|---|---|---|---|---|
| $N_{\mathrm{H}}$ [$10^{22}\mathrm{cm}^{-2}$] | *0.15* | *0.00* | *0.30* | *0.03* |
| $kT_{\mathrm{in}}$ [keV ] | *0.61* | *0.81* | *0.88* | *0.69* |
| $\mathrm{norm}_{\mathrm{bb}}$ | $703.0^{+27.0}_{-28.0}$ | $32.0^{+6.0}_{-5.0}$ | $54.0^{+4.0}_{-4.0}$ | $133.0^{+16.0}_{-16.0}$ |
| $\Gamma$ | *2.00* | *1.90* | *1.89* | *1.87* |
| $\mathrm{norm}_{\mathrm{pl}}$ | $1.195^{+0.008}_{-0.008}$ | $0.667^{+0.012}_{-0.010}$ | $0.971^{+0.008}_{-0.010}$ | $1.029^{+0.010}_{-0.009}$ |
| $\Omega/2\pi$ | *0.68* | *0.57* | *0.53* | *0.49* |
| $E_{\mathrm{K}\alpha}$ [keV ] | $6.56^{+0.02}_{-0.02}$ | $6.51^{+0.03}_{-0.03}$ | $6.48^{+0.03}_{-0.03}$ | $6.55^{+0.02}_{-0.02}$ |
| $\sigma_{\mathrm{K}\alpha,\mathrm{broad}}$ [keV ] | $0.39^{+0.07}_{-0.07}$ | $0.59^{+0.16}_{-0.14}$ | $0.71^{+0.10}_{-0.08}$ | $0.48^{+0.10}_{-0.10}$ |
| $\mathrm{norm}_{\mathrm{K}\alpha,\mathrm{broad}}$ [$10^{-2}$] | $2.5^{+0.2}_{-0.1}$ | $1.6^{+0.2}_{-0.2}$ | $1.7^{+0.2}_{-0.2}$ | $1.9^{+0.2}_{-0.2}$ |
| $\mathrm{norm}_{\mathrm{K}\alpha,\mathrm{narr}}$ [$10^{-4}$] | $4.7^{+0.6}_{-0.9}$ | $2.2^{+0.6}_{-0.6}$ | $2.3^{+0.7}_{-0.7}$ | $5.1^{+0.9}_{-1.0}$ |
| $\beta$ | $4.45^{+0.41}_{-0.32}$ | $4.14^{+0.74}_{-0.64}$ | $3.09^{+0.26}_{-0.23}$ | $4.07^{+0.60}_{-0.48}$ |
| $i$ [deg] | $52.2^{+2.6}_{-2.1}$ | $51.3^{+5.6}_{-5.0}$ | $45.0^{+2.5}_{-2.7}$ | $50.5^{+3.9}_{-3.7}$ |
| $\mathrm{flux}_{3.5-9.5\,\mathrm{keV}}$ disk [$10^{-11}\mathrm{erg\,cm^{-2}\,s^{-1}}$] | 8.54 | 3.34 | 9.24 | 4.27 |
| $\mathrm{flux}_{3.5-9.5\,\mathrm{keV}}$ pl [$10^{-9}\mathrm{erg\,cm^{-2}\,s^{-1}}$] | 2.04 | 1.36 | 1.97 | 2.17 |
| $\chi^2_{\mathrm{red}}$/dof | 1.828 / 81 | 1.653 / 81 | 1.822 / 81 | 1.482 / 81 |

## 5.3 Variability of the line

The multiple *XMM-Newton* observations also allow us to track the evolution of the spectral parameters not only with time but also with with luminosity of the source. As the `kdblur` model described above proved to give the most reasonable parameters we only use those fits for comparison in the following.

### 5.3.1 Variability with time

As shown in Fig 5.5, in which the data over model ratios for a power law fit to the data outside the 5–8 keV range are plotted, the iron line is strongly variable during our observations. Especially obs3 differs significantly from the other three observations. This behavior is also obvious in the measured parameters: obs3 is found to have the lowest values for the line energy as well as for the disk emissivity index $\beta$ and the inclination (see also Fig. 5.4), but the largest width $\sigma_{\rm broad}$. Overall the line as well as the disk parameters of obs1, obs2, and obs4 are consistent with each other, showing the special status of obs3.

Apart from being lowest in obs3, the line energy shows in general the tendency to be lower in the middle two observations as compared to obs1 and obs4. The same holds true for the normalizations of the power-law (and therefore the flux attributed to the corona) and the disk black body. The flux of the disk component, however, is highest in obs3[5].

This picture mirrors the high variability of Cygnus X-1 seen in the light curves. While it is not surprising that the line parameters show no clear trend, it is unexpected that obs3 is the "misfit", as rather obs2 shows a different luminosity and variation coefficient (see Table 3.4). We therefore decided to also test the data on variations with luminosity.

### 5.3.2 Variability with luminosity

To study the variability with luminosity, we divided the *XMM-Newton* observations in four different luminosity levels as shown in Fig 5.6. The band with the lowest luminosity (hereafter called "level1") comprises all data with count rates up to 200 cts $s^{-1}$. The intermediate bands consist of data with count rates between 200 and 250 cts $s^{-1}$ ("level2") and 250 and 300 cts $s^{-1}$ ("level3"), respectively. In the "level4" band all data with count rates larger than 300 cts $s^{-1}$ are accumulated. For the analysis the continuum parameters were again determined using *RXTE* (with the respective *RXTE* GTIs corresponding to the *XMM-Newton* ones). Again we list here only the `kdblur` results which can be found in Table 5.10.

[5] As the flux is not associated to the normalization in the `diskbb` model, this assertion cannot directly be seen from the normalizations.

Table 5.10: Fits using the `kdblur` model. $\sigma_{\mathrm{K}\alpha,\mathrm{narr}}$ has been fixed to 50 eV.

| | **level1** | **level2** | **level3** | **level4** |
|---|---|---|---|---|
| $N_{\mathrm{H}}$ [$10^{22}\mathrm{cm}^{-2}$] | *0.00* | *0.00* | *0.00* | *0.20* |
| $kT_{\mathrm{in}}$ [keV ] | *0.59* | *0.81* | *0.80* | *0.68* |
| $\mathrm{norm}_{\mathrm{bb}}$ | $261.0^{+34.0}_{-29.0}$ | $72.0^{+5.0}_{-4.0}$ | $97.0^{+7.0}_{-7.0}$ | $451.0^{+35.0}_{-31.0}$ |
| $\Gamma$ | *1.88* | *1.90* | *1.91* | *1.95* |
| $\mathrm{norm}_{\mathrm{pl}}$ | $0.677^{+0.006}_{-0.007}$ | $0.943^{+0.006}_{-0.007}$ | $1.164^{+0.010}_{-0.010}$ | $1.472^{+0.016}_{-0.020}$ |
| $\Omega/2\pi$ | *0.46* | *0.44* | *0.45* | *0.58* |
| $E_{\mathrm{K}\alpha}$ [keV ] | $6.50^{+0.03}_{-0.02}$ | $6.51^{+0.02}_{-0.02}$ | $6.56^{+0.03}_{-0.02}$ | $6.57^{+0.03}_{-0.03}$ |
| $\sigma_{\mathrm{K}\alpha,\mathrm{broad}}$ [keV ] | $0.52^{+0.10}_{-0.11}$ | $0.56^{+0.07}_{-0.06}$ | $0.49^{+0.09}_{-0.08}$ | $0.48^{+0.12}_{-0.13}$ |
| $\mathrm{norm}_{\mathrm{K}\alpha,\mathrm{broad}}$ [$10^{-2}$] | $1.9^{+0.2}_{-0.1}$ | $1.7^{+0.1}_{-0.1}$ | $2.0^{+0.2}_{-0.2}$ | $3.1^{+0.4}_{-0.3}$ |
| $\mathrm{norm}_{\mathrm{K}\alpha,\mathrm{narr}}$ [$10^{-4}$] | $2.6^{+0.5}_{-0.5}$ | $3.0^{+0.6}_{-0.6}$ | $4.3^{+0.9}_{-1.0}$ | $4.6^{+1.5}_{-1.4}$ |
| $\beta$ | $5.02^{+0.63}_{-0.65}$ | $3.46^{+0.27}_{-0.21}$ | $3.54^{+0.38}_{-0.27}$ | $4.17^{+0.74}_{-0.46}$ |
| $i$ [deg] | $55.4^{+3.3}_{-4.4}$ | $47.4^{+2.1}_{-2.0}$ | $46.4^{+3.0}_{-2.7}$ | $51.9^{+4.5}_{-3.7}$ |
| $\mathrm{flux}_{3.5-9.5\,\mathrm{keV}}$ disk [$10^{-11}\mathrm{erg\,cm^{-2}\,s^{-1}}$] | 2.23 | 7.15 | 8.99 | 11.7 |
| $\mathrm{flux}_{3.5-9.5\,\mathrm{keV}}$ pl [$10^{-9}\mathrm{erg\,cm^{-2}\,s^{-1}}$] | 1.41 | 1.89 | 2.26 | 2.68 |
| $\chi^2_{\mathrm{red}}$/dof | 1.760 / 81 | 1.880 / 81 | 1.273 / 81 | 1.320 / 81 |

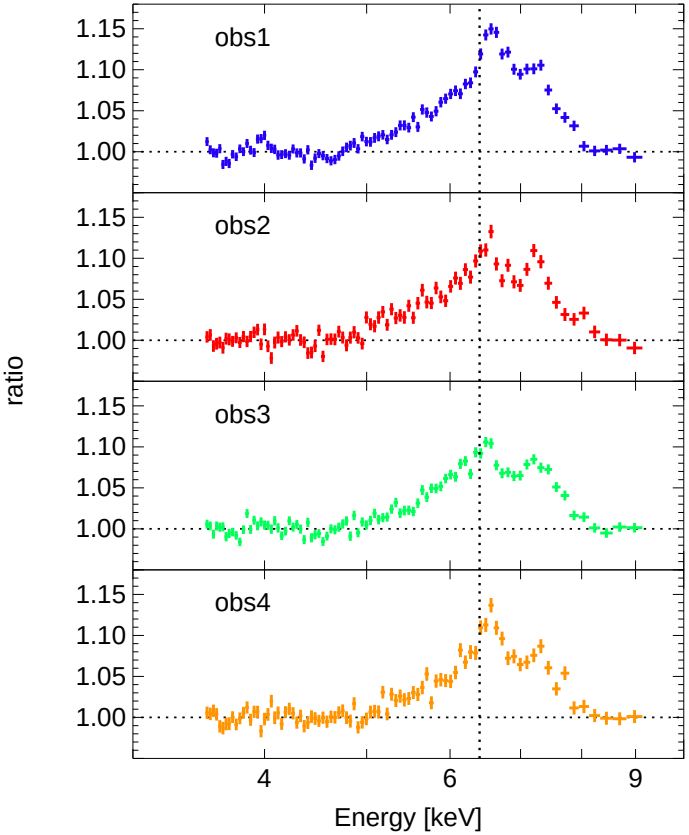


Figure 5.5: Variation of the iron line with time.

The first thing to notice is the increase in the obtained line energy from 6.50 keV in level1 to 6.57 keV in level4. This increase is most probably due to CTE effects as described in section 4.3.3. Also increasing with luminosity is the fraction the disk contributes to the total flux in the 3.5–9.5 keV band (from 1.6% to 4.2%), accompanied by a softening of the powerlaw, a behavior typical for black holes.

For the other disk parameters $\beta$ and $i$ no such trend is observed. The emissivity index $\beta$ is highest in level1, but within the uncertainties the value found for level4 is consistent with this first value. The values found for $\beta$ in the intermediate levels 2 and 3 are also consistent with the level4 value due to the rather large uncertainties. The same picture applies to the inclinations: level4 is in between

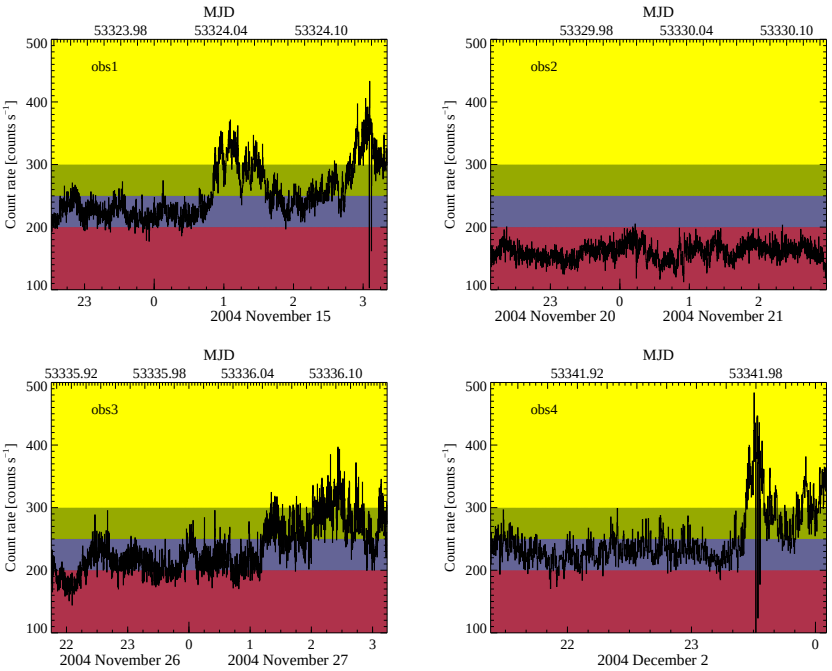


Figure 5.6: Light curves of the four *XMM-Newton* observations. The colors indicate the chosen luminosity levels (from bottom to top level1 – level4).

the values of level1 (where the largest value is found), and those of level2 and level3. Like it was the case for the temporal evolution of the spectral parameters, they also show no clear correlation with luminosity.

Fig. 5.7 shows again the data over model ratio for a power law fit to the data outside the 5–8 keV region to illustrate the different line shapes. The luminosity is decreasing from top to bottom.

## *5.4 Summary and Discussion*

In this chapter the results of the spectral analysis of our *XMM-Newton* observations of Cyg X-1 were described. The data show clearly the presence of a relativistically broadened iron line with a narrow core as reported before in *Chandra* data by Miller et al. (2002). The model used to describe the continuum was composed of an absorbed black body and a power-law including reflection. We mod-

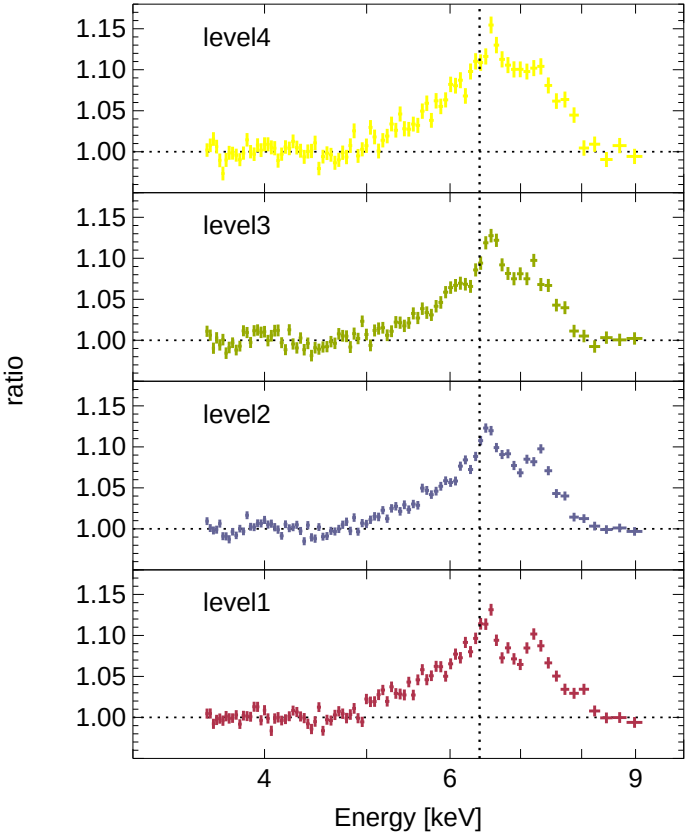


Figure 5.7: Variation of the iron line with luminosity.

eled the line emission by combination of a narrow Gaussian (with fixed width of $\sigma_{\mathrm{K}\alpha,\mathrm{narr}} = 50\,\mathrm{eV}$) and a broad line feature using the `diskline` model (corresponding to a black hole with zero spin) as well as with the `laor` model (corresponding to a maximally rotating Kerr black hole). Furthermore the addition of a smeared edge is favored by all models in terms of a decreasing $\chi^2_{\mathrm{red}}$. As the parameters of the black body component could not be constrained within the restricted energy range of *XMM-Newton*, we determined the continuum parameters with *RXTE* and kept them fixed throughout the analysis.

We also tried to model the data (keeping the continuum parameters also fixed to *RXTE* values) with only a smeared edge and a narrow line. These attempts,

however, resulted in no successful description of the data, with $\chi^2_{\rm red}$ of the order of 5. We therefore have not quoted the results of the fits in more detail, as this model can be clearly ruled out.

The `diskline` and `laor` were equally well suited to describe the data in terms of $\chi^2_{\rm red}$. Hence no clear statement can be made about the spin of Cyg X-1. The only discrimination criterion which is found to be clearly different is the inclination of the system. While the `diskline` fits tend to an edge on result (90°), the `laor` fits favor an inclination of $\sim 67°$. The allowed range for the angle derived from the super-orbital modulation period (which is attributed to precession of the accretion disk) is $37° \leq \theta \leq 66°$. Thus the `laor` model is favored in terms of giving more physically reasonable parameters. However, the `laor` fits are still found on the borderline of the allowed region. We therefore applied also the `kdblur` model to the data – a relativistic convolution model based on the `laor` code.

Using `kdblur`, the quality of the fits in terms of $\chi^2_{\rm red}$ is the same as in the models described before, but `kdblur` gives a much better description of the continuum as the edge component which was additionally needed in the `diskline` / `laor` fits with reflection is now already described by the blurred reflection model itself. Furthermore, the inclination found using this model is fully consistent with the theoretically predicted values of $\theta$. We therefore conclude that `kdblur` provides the best description of our data.

The iron line profile showed a strong variability during the observations. Comparing the `kdblur` parameters, especially obs3 sticks out as it differs in virtually all parameters from the other three observations. This behavior is hard to understand, as from the light curves obs3 is very similar to obs1 and obs4 and rather obs2 is different.

Also with luminosity a variation in the disk parameters was found, however, no clear trend is evident. The only smooth variations found are an increase of the line energy with luminosity (which can be attributed to CTE effects) and an increase in the strength of the disk component in the spectrum accompanied by a spectral softening.

### *5.4.1 Comparison with Chandra*

All our results hint that Cygnus X-1 is indeed best described by a Kerr model instead of the pure Schwarzschild model `diskline`. This interpretation, however, is in sharp contrast with the 2002 *Chandra* results by Miller et al. (see also Miller 2006). These authors claimed that Cyg X-1 is harboring a not or only marginally spinning black hole. A direct comparison of the parameters found for both data sets is given in the following. As obs2 shows most similarities with the *Chandra* parameters, we decided to use this observation for comparison. To achieve compa-

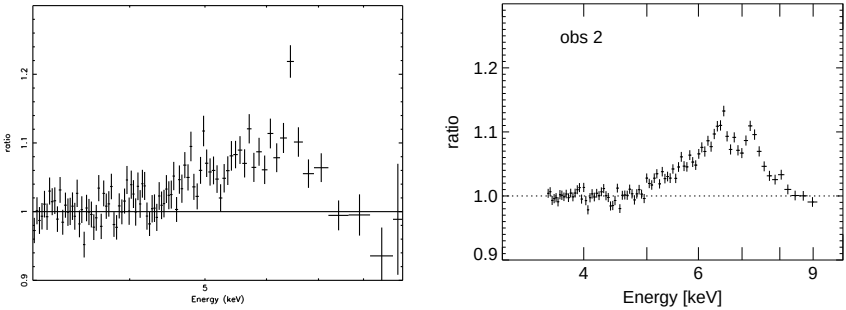


Figure 5.8: Left: *Chandra* data/model ratio of the iron line region, ignoring the 4.0–7.2 keV range in the fit to the data. Right: Same for the second *XMM-Newton* observation.

rability concerning the energy ranges available for the analysis, for *XMM-Newton* the fits without the *RXTE* constrained continuum parameters are quoted.

The continuum parameters are difficult to compare, as they strongly depend on the state Cyg X-1 is observed in. However, while the power-law indices are virtually identical ($\Gamma = 1.80^{+0.01}_{-0.01}$ for *Chandra* and $\Gamma = 1.82^{+0.07}_{-0.03}$ for *XMM-Newton*), the power-law normalization and the black body parameters are quite different. This difference might be due to the fact that the black body component could not be constrained by *XMM-Newton*, but could also be indicative of a slightly different state in the two observations. Miller et al. (2002) state that their observation took place during an Intermediate State (like the *XMM-Newton* observations), however, also the *RXTE* continuum parameters are different from the *Chandra* values. Therefore we conclude that the states have indeed been slightly different.

The energy of the narrow iron line core is found to be at 6.42 keV with *Chandra*. The *XMM-Newton* best fit value of $6.52^{+0.03}_{-0.03}$ keV is significantly higher, but due to the CTE over-correction still consistent with the *Chandra* value. The same holds true for the energy of the broad line component which is centered at $5.90^{+0.10}_{-0.04}$ keV in the *XMM-Newton* data and at $5.85^{+0.01}_{-0.01}$ keV in the *Chandra* data, but the equivalent width of the broad line in *XMM-Newton* is with 112 eV almost twice the value found for *Chandra* ($\mathrm{EW}_{\mathrm{K}\alpha,\mathrm{diskl}} = 60$ eV). With values of $E_{\mathrm{edge}} = 7.36^{+0.09}_{-0.12}$ keV/ $\tau_{\mathrm{edge}} = 0.81^{+0.19}_{-0.08}$ (*XMM-Newton*) and $E_{\mathrm{edge}} = 7.2^{+0.1}_{-0.1}$ keV/ $\tau_{\mathrm{edge}} = 1.2^{+0.2}_{-0.2}$ (*Chandra*), the parameters of the edge are consistent.

The main disagreement between the *XMM-Newton* and *Chandra* results is seen in the fitted inclination angle. While Miller et al. find a value of $40^{+10}_{-10}$ deg, the *XMM-Newton* value for obs2 is $76.5^{+13.5}_{-8.9}$ deg. We therefore calculated also the allowed range of $\theta$ from the super-orbital phase for the *Chandra* observation (which took place at $\Phi = 0.060$) to $38^\circ \leq \theta \leq 67^\circ$. Hence $40^\circ$ is well within this al-

lowed region. The *XMM-Newton* value, however, is outside the region quoted for obs2 in Tab 5.8. Fixing the inclination in the *XMM-Newton* fit to 40° yielded a significantly worse $\chi^2_{\rm red}$. It must therefore be stated that in case of the *XMM-Newton* observations – contrary to *Chandra*– the `diskline` model is not able to produce meaningful results (at least for the inclination). To distinguish between a Schwarzschild and a Kerr black hole in Cygnus X-1 further high resolution observations of the iron line region are urgently needed.

# Part II

# Neutron Star Binaries: 4U 1907+09

# Chapter 6

# Some Neutron Star X-ray Binary Physics

The second part of this thesis is dedicated to the analysis of a neutron star X-ray binary, namely the source 4U 1907+09. Before the detailed analysis is described in chapter 7 some basic observational properties of neutron stars and their underlying physical models shall briefly be reviewed in this chapter.

## *6.1 Accretion onto highly magnetized Neutron Stars*

While the overall principles of accretion are the same for black hole and neutron star binary systems, the accretion process onto the compact object itself is quite different. The main difference of course arises from the presence of a surface on neutron stars, which can be "seen", e.g., by the detection of type I X-ray bursts. Apart from the surface, the second relevant difference is the presence of magnetic fields with up to $10^{13}$ G in neutron stars. These strong magnetic fields make the accretion process far more complex than accretion onto black holes.

Inside the magnetosphere of neutron stars the matter is forced to follow the magnetic field lines and is accreted onto the poles of the neutron star (reaching free-fall velocities of $\sim 0.4c$) on an area of only $\sim 1\,\mathrm{km}^2$ (Lamb et al. 1973). Above these polar caps an accretion column forms. The exact shape of the accretion column depends on the mass accretion rate: above the critical luminosity (Basko & Sunyaev 1976)

$$L_{\mathrm{crit}} = 2\frac{l_0}{R}\frac{c}{\kappa}\frac{GM}{R} \tag{6.1}$$

the radiation pressure can decelerate the accretion stream and a shock front forms inside the accretion column. Here $l_0$ is the diameter of the accretion funnel, $\kappa$ the opacity and $R$ the radius of the neutron star. For typical neutron star parameters this critical luminosity is around $10^{36}\,\mathrm{erg\,s^{-1}}$. In the shock front the kinetic energy is converted into thermal energy. Below the shock front – whose height above the neutron star surface depends on $\dot{M}$ – the plasma (which is now very hot) sinks down to the surface of the neutron star, thereby cooling through the emission of

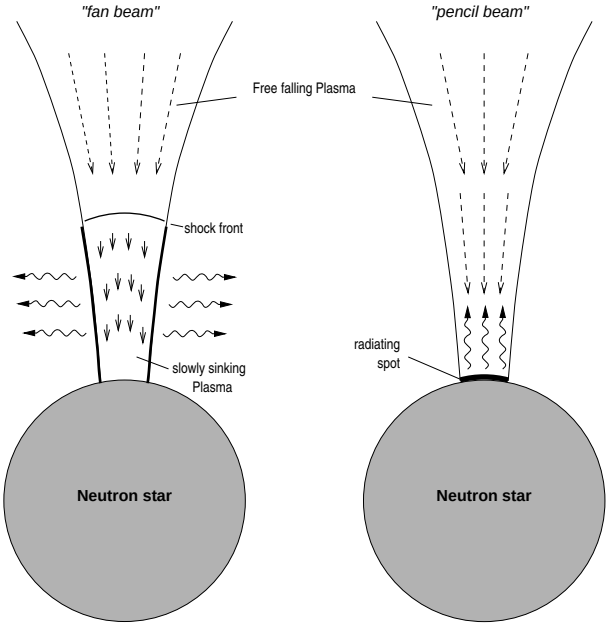


Figure 6.1: Geometries of the accretion column (Kretschmar 1996). *Left:* Case of a source with high $\dot{M}$ and the therefrom resulting fan-beam geometry. *Right:* pencil-beam geometry for the case of low accretion rates.

X-ray photons. As the column itself is almost opaque to X-rays, the radiation leaves the accretion column perpendicular to the magnetic field axis. This emission pattern is called “fan beam” geometry (Fig. 6.1, left).

If the luminosity is below the critical value $L_{\mathrm{crit}}$ the radiation pressure cannot decelerate the infalling material. In this case the deceleration most probably occurs through Coulomb interactions or through Bremsstrahlung processes. The matter sinks to the neutron star surface where a thin radiating polar cap forms at the bottom of the accretion column. As the optical depth of the plasma is low, the radiation is emitted parallel to the magnetic field axis in a very narrow emission pattern. Therefore this geometry is called “pencil beam” (Fig. 6.1, right).

The detailed structure of the inside of the accretion column is not known yet. The classical picture of a filled cylinder is shown in Fig. 6.2 on the right. However, the material couples to the field lines at a certain radius in the accretion disk, the

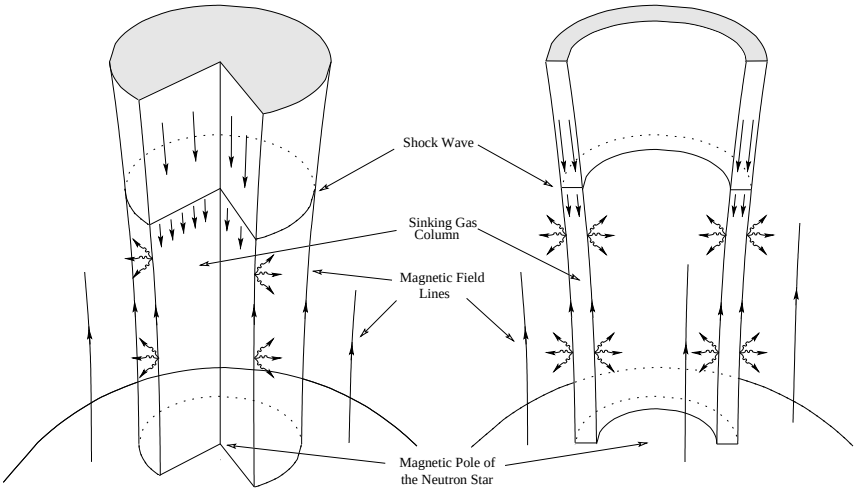


Figure 6.2: Inside of the accretion column (Figure from Kuster, 2003, after Basko & Sunyaev 1976). *Left:* Classical picture of a filled whole cylinder. *Right:* The infalling matter is constrained to the walls of a hollow cylinder.

magnetospheric (or Alfvén) radius

$$P_{\rm Gas} = P_{\rm mag} \quad \Rightarrow \quad r_{\rm m} = \left(\frac{8\pi^2}{G}\right)^{\frac{1}{7}} \left(\frac{R^{12}B^4}{M\dot{M}^2}\right)^{\frac{1}{7}} \tag{6.2}$$

which is $\approx 3.5 \cdot 10^8$ cm for typical neutron star parameters. That radius corresponds to one certain magnetic field strength. Those field lines of the same strength all emerge at the same radius around the magnetic pole. Therefore the accretion funnel should take the form of a hollow cylinder (Fig. 6.2, right). This model has been proposed already by Basko & Sunyaev (1975) who also showed that the walls of the cylinder are small compared to its radius.

Inside the accretion column, the seed photons produced by the deceleration of the infalling matter are most probably upscattered by bulk Comptonization in the accretion shock. Therefore the emerging continuum spectrum is best described by a power law with exponential high energy cutoff. A more detailed description of the ongoing processes and their modeling is beyond the scope of this thesis but can be found in, e.g. (Becker & Wolff 2005a,b, 2007).

## 6.2 Variability of Neutron Star XRBs

As the overall emission pattern is very narrow in both cases and the magnetic axis will usually not coincide with the rotational axis, accreting NS XRBs show a modulation in their X-ray flux that is due to their rotation period (as already mentioned in section 1.1.1). This pulse period of accreting binaries, however, is not constant but varies with time. If the dominant accretion mechanism is wind accretion, it often shows a kind of random walk behavior as could be observed for example in sources like Vela X-1 (de Kool & Anzer 1993). In other sources the period evolution might show a more smooth behavior with long phases of constant spin-down followed by a phase of spin-up (as for example observed in 4U 1907+09).

But what is the reason of this change in the period? The crucial parameter for the evolution of the pulse period is the transfer of angular momentum from the accreted material onto the neutron star. According to the model of Ghosh & Lamb (1978, 1979a,b) the algebraic sign and absolute value of this parameter are defined by the magnetosphere of the neutron star. Close to the star – in the so called transition region – the magnetic field lines can penetrate the accretion disk material and interact with the plasma. The inner boundary of this region is defined by the magnetospheric radius, the outer boundary by the screening radius $r_s$. The transition region itself is further divided into a thin boundary layer in which the plasma leaves the disk perpendicular to its surface and an outer transition zone in which viscous forces dominate over the magnetic ones (see Fig. 6.3). Outside the transition zone the disk is screened completely against the magnetic field lines due to a slow radial drift of the plasma transverse to the field. These drift leads to a weak current that causes the screening outside $r_s$.

Another important parameter of this geometry is the corotation radius where the angular velocity of the material in the disk (which rotates with Keplerian velocity $\Omega_K = \sqrt{GM/r^3}$) equals the angular velocity $\Omega_{ns}$ of the neutron star and therefore the angular velocity of the magnetosphere

$$r_{co} = \left(\frac{GM}{\Omega_{ns}^2}\right)^{\frac{1}{3}} \quad . \tag{6.3}$$

To understand changes in the pulse period the "fastness parameter" needs to be defined also (Elsner & Lamb 1977):

$$\omega_s = \frac{\Omega_{ns}}{\Omega_K(r_m)} = \left(\frac{r_m}{r_{co}}\right)^{\frac{3}{2}} \quad . \tag{6.4}$$

The neutron star is accelerated for the case of $\omega_s \ll 1$ (which means $r_m \ll r_{co}$) leading to an observed spin-up. Wang (1995) found that for a critical fastness

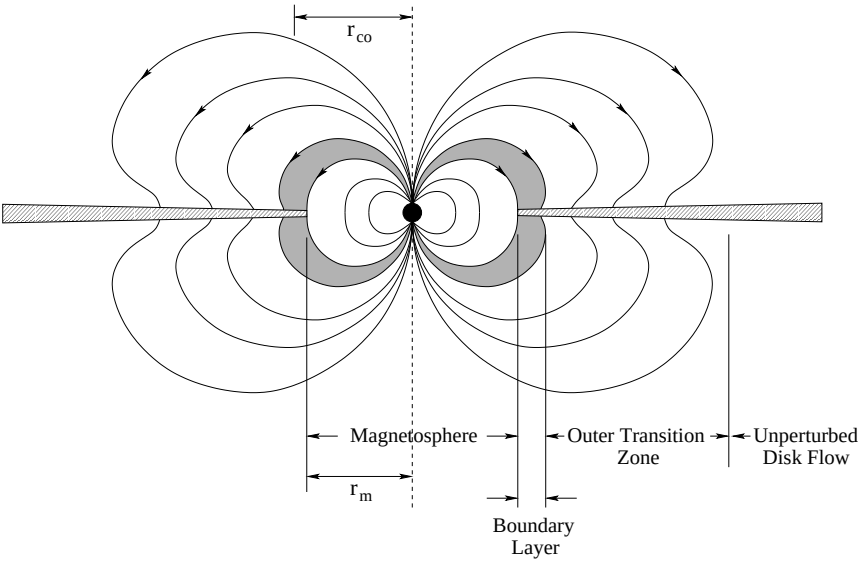


Figure 6.3: Accretion geometry around a neutron star according to the model of Ghosh & Lamb (1978, 1979a,b, Figure from Kuster, 2003).

of $\omega_{\rm crit} \approx 0.875 - 0.95$ this process changes to a deceleration of the neutron star and an observed spin-down due to slower rotating plasma outside $r_{\rm co}$. The overall period evolution can be described by (Ghosh & Lamb 1979b)

$$-\frac{\dot{P}_{\rm pulse}}{P_{\rm pulse}} \propto \frac{r^{6/7}}{M^{3/7} I} \cdot n(\omega_{\rm S}) \cdot \mu^{2/7} \cdot P_{\rm pulse} \cdot L^{6/7} \tag{6.5}$$

with $n(\omega_{\rm S})$ being a dimensionless function of the fastness parameter, $\mu$ the magnetic moment, and $I$ the effective moment of inertia. Thus the main parameters which determine the evolution of the pulse period are the luminosity of the system, its actual pulse period and its magnetic moment. Fig. 6.4 shows this $-\dot{P}_{\rm pulse} \propto P_{\rm pulse} L^{3/7}$ proportionality for different values of the magnetic moment. In the plot there are also measurements of nine accreting X-ray binaries included, showing that it is in principle possible to estimate the magnetic moment of a neutron star by measuring its luminosity, its pulse period, and pulse period derivative.

However, it is very difficult to get firm statements about the magnetic field of neutron stars just from pulse period measurements as these measurements themselves are subjected to errors and furthermore the values for $R$ and $I$ as well as for the the mass of most objects are still questionable. A more reliable method of

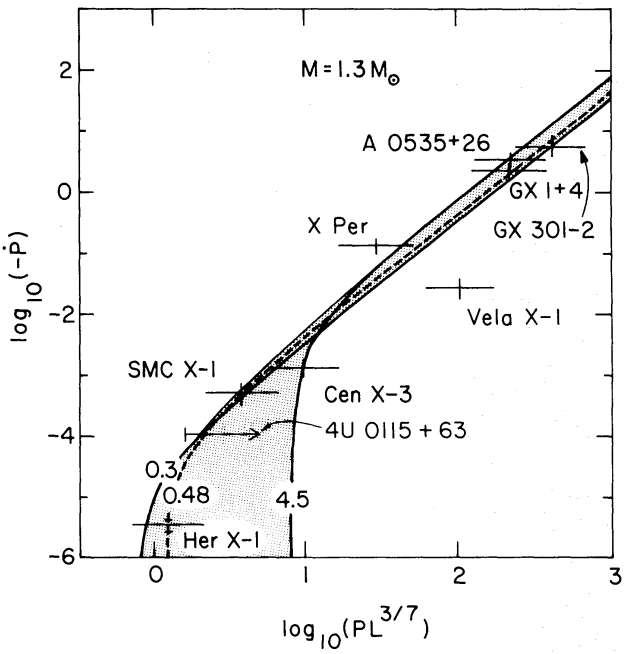


Figure 6.4: Correlation between $-\dot{P}_{\rm pulse}$ and $P_{\rm pulse}L^{3/7}$ for different values of the magnetic moment $\mu$ (Ghosh & Lamb 1979b).

obtaining the strength of the magnetic field is the measurement of so called "cyclotron resonant scattering features" whose energy is directly related to the field strength as will be explained in the following section.

## *6.3 Cyclotron Resonant Scattering Features*

In the strong magnetic fields of neutron stars (which are in the order of $10^{12}$ G) the kinetic energy of electrons perpendicular to the field is not continuous but quantized in so called Landau levels (see, e.g., Harding & Daugherty 1991; Lai 2001; Schönherr 2007)

$$E_n = m_e c^2 \sqrt{1 + \left(\frac{p_\parallel}{m_{\rm e} c^2}\right)^2 + 2n\frac{B}{B_{\rm crit}}} \quad . \tag{6.6}$$

In this equation $n$ is the quantum number and $p_{\|}$ the moment of the electrons parallel to the magnetic field. Above a critical magnetic field strength $B_{\rm crit} = (m_{\rm e}c^2)/(e\bar{h}) \approx 4.4 \cdot 10^{13}$ G the cyclotron energy is of the same order as the electron rest mass. In this case the Landau levels are not equally spaced any more and relativistic corrections must be applied.

In the non-relativistic case the difference between two Landau levels is given by the cyclotron energy (Canuto & Ventura 1977)

$$E_{\rm cyc} = \frac{e\bar{h}}{m_e c} B \approx 11.6\,{\rm keV}\left(\frac{B}{10^{12}{\rm G}}\right) \tag{6.7}$$

which is the famous 12-$B$-12-rule. Electrons can only change between these Landau levels if they absorb or emit a photon with $E = n \cdot E_{\rm cyc}$. The life time of the excited Landau levels is very short (typical values are $\sim 10^{-15}(B/10^{12}{\rm G})^{-1}$ s, Latal 1986), therefore an excited electron de-excites practically instantaneous by emitting a resonant photon. However, as the photon is immediately re-emitted after being absorbed, the whole process is more scattering-like than absorption-like.

In first works by Trümper et al. (1977) (the first detection of a cyclotron resonant scattering feature at all!) or Yahel (1979) it was believed that the process described above would lead to an emission line in the spectrum. Herold (1979) and Nagel (1981) showed, however, that the line has to be an absorption line as the mean free path of the photons is so small that they almost instantly excite another electron after being emitted and therefore cannot leave the emitting plasma. In the spectrum these "absorption" lines are found at multiples of $E_{\rm cyc}$ (see Fig. 6.5 for an example) and allow therefore the calculation of the magnetic field strength via the 12-$B$-12-rule (Eq. 6.7). As the emitting region is expected to be close to the surface of the neutron star, the derived field strength has to be corrected for gravitational redshift effects via

$$\frac{B}{10^{12}{\rm G}} = (1+z)\frac{E_{\rm cyc}^{\rm obs}}{11.6\,{\rm keV}} = \left(1 - \frac{2GM_{\rm NS}}{Rc^2}\right)^{-1/2} \frac{E_{\rm cyc}^{\rm obs}}{11.6\,{\rm keV}} \quad . \tag{6.8}$$

Assuming an emission region directly at the neutron star surface (and therefore $R = 10$ km) and a typical neutron star mass of $M_{\rm NS} = 1.4\,{\rm M}_\odot$ this equation leads to a correction of the magnetic field strength of the order of ~30%.

Observations have shown, however, that the cyclotron lines are not found at strictly the same energies for different pulse phases (and therefore different viewing angles on the line emitting region) of the neutron star (see, e.g., Santangelo et al. 1999; Heindl & Chakrabarty 1999; Burderi et al. 2000; Kreykenbohm et al. 2004; Pottschmidt et al. 2005). The observed variation of up to ~ 30% with phase,

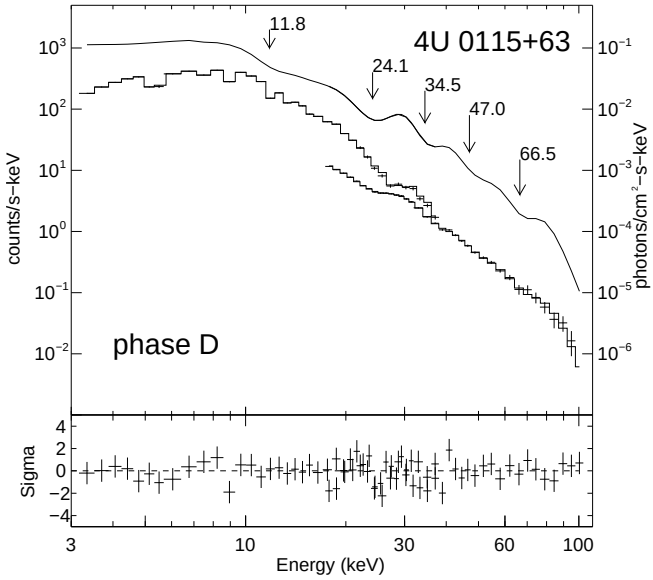


Figure 6.5: Example of cyclotron lines in the source 4U 0115+63 (Kreykenbohm 2004).

is too large to be explained by simply applying relativistic corrections to the energies of the Landau levels (Harding 1994)

$$E_n = \frac{m_e c^2}{\sin^2\theta}\left(\sqrt{1+2n(B/B_{\rm crit})\sin^2\theta}-1\right) \quad , \tag{6.9}$$

with $\theta$ being the angle between the magnetic field vector and the photon direction[1]. Instead, the widely accepted scenario to explain the phase dependency of the line energy is that different regions of the accretion column have a different magnetic field strength and hence the observed variations are due to the observation of regions with different magnetic fields.

Variations in the magnetic field across the line forming region are also thought to be responsible for the non-linear spacing of the harmonics of the cyclotron lines which is observed in several sources (e.g., 4U 0115+63, Fig. 6.5). It was found by Nishimura (2005), that the line ratios decrease if the magnetic field increases linearly with height. Vice versa the line ratios increase for a decreasing $B$-field.

[1]It should be noted that the exact definition of $\theta$ is quite difficult as light bending effects lead to a deflection of the photons of 90° and more.

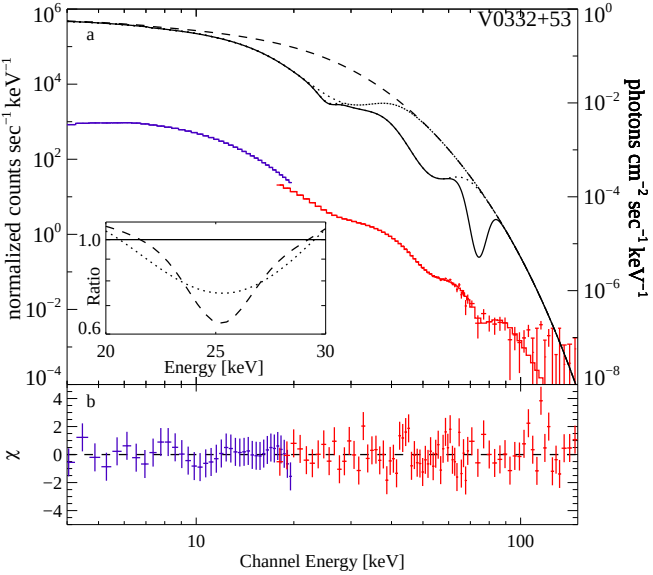


Figure 6.6: Example for the complex line shape in the source V0332+53 (adapted from Pottschmidt et al. 2005).

Such a varying field was proposed by Gil et al. (2002) through the superposition of a dipole field centered in the core of the neutron star and a dipole anomaly in the crust.

One point that is not addressed by analytical examinations is the question for the shape of the line. Observations have revealed the fundamental line to show a complex structure that cannot be modeled with a simple Gaussian. Fig. 6.6 (Pottschmidt et al. 2005) shows the example of V0332+53 where the fundamental line requires a combination of a narrow and a shallow Gaussian at slightly different energies. Monte Carlo simulations (e.g., Schönherr 2007) show that the main parameter defining the shape of the line is the plasma temperature, as the hotter the plasma the more asymmetric and wider the lines. The continuum shape also influences the structure of the fundamental, which can be explained as photon redistribution effects mainly due to photon spawning (i.e., Compton scattering with multiple photon emission where a photon with energy $2E_{\rm cyc,1}$ results in two photons with energy $E_{\rm cyc,1}$, Alexander & Mészáros 1989) in hard continua. This effect of making the fundamental line shallower than the first harmonic due to photon spawning was also observed in, e.g., 4U 0115-63 (Santangelo et al. 1999) and 4U 1907+09 (which will be the subject of the following chapter).

# Chapter 7

# A torque reversal of 4U 1907+09

In this chapter the analysis of the neutron star High Mass X-ray Binary system 4U 1907+09 is described. The analysis is based on *INTEGRAL* observations performed between 2003 and 2005. In Sect. 7.2 the *INTEGRAL* data reduction is described, followed by a discussion of the broadband X-ray spectrum of the source (Sect. 7.3). Afterwards the results of the long term X-ray timing analysis (Sect. 7.4.1) are presented, showing that the source underwent a torque reversal towards a spin up (Sect. 7.4.2). Finally the results are summarized and discussed in Sect. 7.5.

Since this chapter is based on Fritz et al. (2006) the typical paper structure is adopted.

## *7.1 The 4U 1907+09 system*

The wind-accreting High Mass X-ray Binary system 4U 1907+09 (Giacconi et al. 1971) consists of a neutron star in an eccentric ($e = 0.28$) 8.3753 d orbit (in 't Zand et al. 1998) around its companion, which has been identified optically with a highly reddened $m_V = 16.37$ mag star (Schwartz et al. 1980). Using interstellar atomic lines of NaI and KI, Cox et al. (2005) set a lower limit of 5 kpc for the distance. According to this value a lower limit of the X-ray luminosity above 1 keV is given by $2\,10^{36}\,\mathrm{erg\,s^{-1}}$ (in 't Zand et al. 1997). Cox et al. (2005) also confirm earlier suggestions (Schwartz et al. 1980; Marshall & Ricketts 1980; van Kerkwijk et al. 1989) that the stellar companion is a O8–O9 Ia supergiant with an effective temperature of 30500 K, a radius of $26\,R_\odot$, a luminosity of $5\,10^5\,L_\odot$, and a mass loss rate of $7\,10^{-6}\,M_\odot\,yr^{-1}$. Note that the presence of X-ray flaring seen twice per neutron star orbit (Marshall & Ricketts 1980, see also Fig. 7.1) had led some authors (e.g., Makishima et al. 1984; Iye 1986; Cook & Page 1987) to the suggestion of a Be star companion, however, this classification would require a distance of <1.5 kpc, which is in contradiction to the significant interstellar extinction measured in optical observations (van Kerkwijk et al. 1989).

Similar to other accreting neutron stars, the X-ray continuum of 4U 1907+09 can be described by a power-law spectrum with an exponential turnover at approximately 13 keV (Mihara 1995; in 't Zand et al. 1997; Cusumano et al. 1998). The spectrum is modified by strong photoelectric absorption with a column $N_{\rm H}$ = 1.5–5.7 $10^{22}$ cm$^{-2}$ (Schwartz et al. 1980; Marshall & Ricketts 1980; Makishima et al. 1984; Cook & Page 1987; Chitnis et al. 1993; Cusumano et al. 1998). As the absorbing material is situated in the dense stellar wind, $N_{\rm H}$ is strongly variable over the orbit. The column is maximal between the end of the primary X-ray flare and the start of the secondary flare (Fig. 7.1) of the orbital light curve (Roberts et al. 2001). Fluorescence in the absorbing material gives rise to an Fe K$\alpha$ line at 6.4 keV with an equivalent width of ∼60 eV (Cusumano et al. 1998). At higher energies, the spectrum exhibits cyclotron resonant scattering features (CRSF) at ∼19 keV and ∼40 keV (Makishima et al. 1992; Mihara 1995; Cusumano et al. 1998).

With a pulse period of ∼ 440 s, 4U 1907+09 is a slowly rotating neutron star. Since the discovery of the pulsations by Makishima et al. (1984) the neutron star has exhibited a steady linear spin down with an average of $\dot{P}_{\rm pulse} = +0.225\,{\rm s\,yr^{-1}}$ from $P_{\rm pulse}$ = 437.5 s in 1983 to 440.76 s in 1998 (in 't Zand et al. 1998). Recently, Baykal et al. (2006) reported a decrease in $\dot{P}_{\rm pulse}$, which in 2002 was $\sim 0.115\,{\rm s\,yr^{-1}}$ and therefore ∼0.5 times the long term value.

## *7.2 Observation and data reduction*

For our analysis we took into account all public *INTEGRAL* data up to orbit (revolution) 250 as well as data from the *INTEGRAL* Galactic Plane Scans and the Galactic Central Radian Deep Exposure. In addition we also used private data from a monitoring campaign on the galactic micro-quasar GRS 1915+105 (PI J. Rodriguez). To avoid systematic effects that start to become important for larger off-axis angles, we constrained the maximum off-axis angle between the satellite's optical axis and 4U 1907+09 to 4.°5 for IBIS and 2.°4 for JEM-X according to the respective FCFOVs of the instruments. In total, the analyzed data are spread over almost three years with a total on source time of ∼2280 ksec for IBIS. The log of the observations is given in Table 7.2. We used the Off-line Scientific Analysis Software, `OSA` 5.1, in our analysis. In the analysis of the coded mask data we also took into account the presence of GRS 1915+105, 4U 1901+03, 4U 1909+07, and IGR J19140+0951, by forcing the `OSA` to consider 4U 1907+09 and these four sources.

Background subtracted light curves were obtained using `ii_light`, a tool distributed with the `OSA` to generate high resolution light curves. While the standard

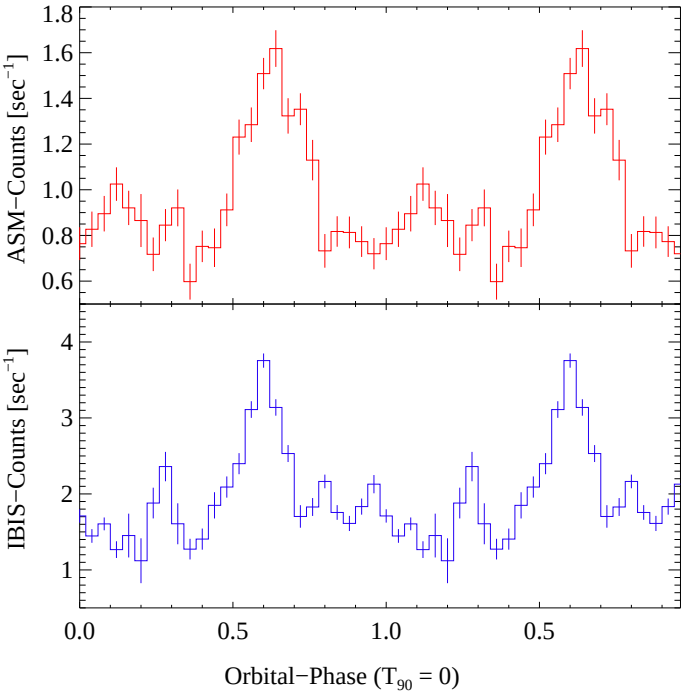


Figure 7.1: Upper Panel: Rossi X-ray Timing Explorer All Sky Monitor (ASM) 2–12 keV light curve of 4U 1907+09 folded on the orbital period of 8.3753 days. Lower Panel: Same for the IBIS 20–40 keV light curve.

`OSA` tools build light curves by deconvolving shadowgrams for each requested energy band and time bin to obtain the light curves, which is only possible if the signal to noise ratio in the shadowgram is high, `ii_light` uses the Pixel Illuminated Fraction (PIF) to create light curves. For 4U 1907+09, this approach allows us to extract light curves with a resolution of 1 s. The count rates found by `ii_light` show no systematic difference between the single pointings. Tests based on observations of the Crab nebula and pulsar (Kreykenbohm et al. 2008) and the fact that the count rates of 4U 1907+09 are not affected by the very variable flux of the nearby source GRS 1915+105 (Fig. 7.2) confirm the stability of our extraction method. The light curves were barycentered and corrected for the orbital motion of the neutron star using the ephemeris of in 't Zand et al. (1998), as given in Table 7.1. Orbital phase 0 is at $T_{90}$.

Table 7.1: Ephemeris used for the binary correction (in 't Zand et al. 1998). $P_{\rm orb}$ is the orbital period, $T_{90}$ the time of mean longitude 90°. All other symbols have their usual meanings.

| Parameter | Value |
|---|---|
| $T_{90}$ | MJD 50134.76 |
| $P_{\rm orb}$ | 8.3753 d |
| $a \sin i$ | 83 lt-s |
| Eccentricity | 0.28 |
| $\omega$ | 330° |

## *7.3 Spectral Analysis*

For the spectral analysis we applied systematic errors of 1% and 5% for IBIS and JEM-X2, respectively, and used data taken in the energy ranges 18–90 keV and 5–20 keV. Because of the switch over from JEM-X2 to JEM-X1 after revolution 171, we only used data taken before that revolution to avoid cross-calibration uncertainties between the two JEM-X detectors. This resulted in a total exposure time of 200 ksec for JEM-X2. For ISGRI we used all public data up to revolution 250 resulting in an exposure time of 1258 ksec. We modeled the spectrum using an absorbed power-law, which is modified by the Fermi-Dirac cutoff (Tanaka 1986):

$$C(E) = E^{-\alpha} \left[ \exp\left( \frac{E_{\rm cut} - E}{E_{\rm fold}} \right) + 1 \right]^{-1} \tag{7.1}$$

This continuum model alone could not describe the data adequately ($\chi^2_{\rm red} = 3.10$, see Tab. 7.3), as strong absorption line like features at ∼19 keV and ∼40 keV remain (Fig. 7.3). These features have been identified as cyclotron resonant scattering features (CRSFs) by Makishima et al. (1992) and have also been reported by Mihara (1995) and Cusumano et al. (1998). The addition of a line at 36.0 keV with a width of 3.7 keV (Table 7.3) with a Gaussian optical depth profile (for definition, see Coburn et al. 2002) to the baseline continuum model results in a improved fit ($\chi^2_{\rm red} = 2.49$ for 47 degrees of freedom). The $F$-test probability that this improvement is achieved just by chance is $3.8 \times 10^{-3}$ (see, however, Protassov et al. 2002). Modeling both features with Gaussians at 39.8 keV and 18.9 keV further improves $\chi^2$ significantly to $\chi^2_{\rm red} = 1.00$. The $F$-Test probability for this case as opposed to the case without lines is $9.8 \times 10^{-10}$, confirming the unambiguous detection of the cyclotron lines. For this model we also added the Fe-line which has been seen, e.g., in the *BeppoSAX* data (Cusumano et al. 1998). The best fit value for the line energy is 7.1 keV. The width of the line could not be constrained by our data, so

Table 7.2: Log of observations.

| Observation | Revolution | Date MJD | On Source Time (IBIS) ksec | $\Phi_{orb}$ | Mean Count Rate cps in 20–40 keV |
|---|---|---|---|---|---|
| 1 | 48 | 52704.1–52705.4 | 100.61 | 0.78–0.93 | 1.26±0.10 |
| 2 | 57 | 52731.1–52732.3 | 72.12 | 0.00–0.14 | 2.44±0.13 |
| 3 | 59 | 52738.3–52739.6 | 107.13 | 0.86–0.02 | 1.66±0.11 |
| 4 | 62 | 52746.7–52747.9 | 72.78 | 0.86–0.01 | 2.76±0.13 |
| 5 | 67 | 52762.9–52763.4 | 33.48 | 0.80–0.86 | 2.12±0.19 |
| 6 | 68 | 52764.6–52766.5 | 61.66 | 0.00–0.22 | 1.92±0.14 |
| 7 | 69 | 52767.8–52769.5 | 107.41 | 0.38–0.59 | 1.66±0.11 |
| 8 | 70 | 52771.2–52771.7 | 32.71 | 0.79–0.85 | 1.87±0.19 |
| 9 | 135 | 52965.7–52966.9 | 104.37 | 0.01–0.16 | 1.50±0.12 |
| 10 | 172 | 53075.9–53076.2 | 23.03 | 0.17–0.21 | 1.39±0.23 |
| 11 | 174 | 53082.6–53083.0 | 23.09 | 0.97–0.01 | 2.26±0.24 |
| 12 | 176 | 53089.1–53089.6 | 30.83 | 0.74–0.81 | 1.07±0.20 |
| 13 | 177 | 53091.0–53092.0 | 51.80 | 0.97–0.09 | 1.30±0.15 |
| 14 | 186 | 53117.0–53117.7 | 37.18 | 0.07–0.16 | 2.37±0.18 |
| 15 | 187 | 53120.7–53122.0 | 65.47 | 0.52–0.67 | 3.70±0.14 |
| 16 | 188 | 53123.2–53125.4 | 75.72 | 0.82–0.08 | 2.55±0.13 |
| 17 | 189 | 53126.3–53128.5 | 62.89 | 0.19–0.45 | 1.46±0.14 |
| 18 | 193 | 53138.1–53140.5 | 185.49 | 0.60–0.88 | 3.60±0.09 |
| 19 | 231 | 53253.4–53254.0 | 33.69 | 0.36–0.43 | 1.32±0.19 |
| 20 | 242 | 53285.4–53285.6 | 19.16 | 0.18–0.21 | 2.02±0.26 |
| 21 | 243 | 53288.9–53289.2 | 21.24 | 0.60–0.64 | 2.27±0.24 |
| 22 | 246 | 53296.4–53297.6 | 100.89 | 0.49–0.64 | 2.79±0.11 |
| 23 | 248 | 53303.9–53305.0 | 144.48 | 0.27–0.52 | 1.78±0.09 |
| 24 | 249 | 53305.7–53308.0 | 141.95 | 0.61–0.87 | 1.54±0.09 |
| 25 | 250 | 53309.1–53311.0 | 100.83 | 0.02–0.23 | 0.97±0.12 |
| 26 | 255 | 53324.3–53325.5 | 98.74 | 0.82–0.97 | 1.60±0.11 |
| 27 | 295 | 53443.0–53444.1 | 99.40 | 0.99–0.14 | 1.37±0.11 |
| 28 | 305 | 53472.9–53474.1 | 106.13 | 0.57–0.72 | 3.11±0.11 |
| 29 | 315 | 53503.6–53504.8 | 72.15 | 0.24–0.37 | 1.88±0.17 |
| 30 | 361 | 53640.4–53641.6 | 91.67 | 0.57–0.71 | 3.16±0.11 |

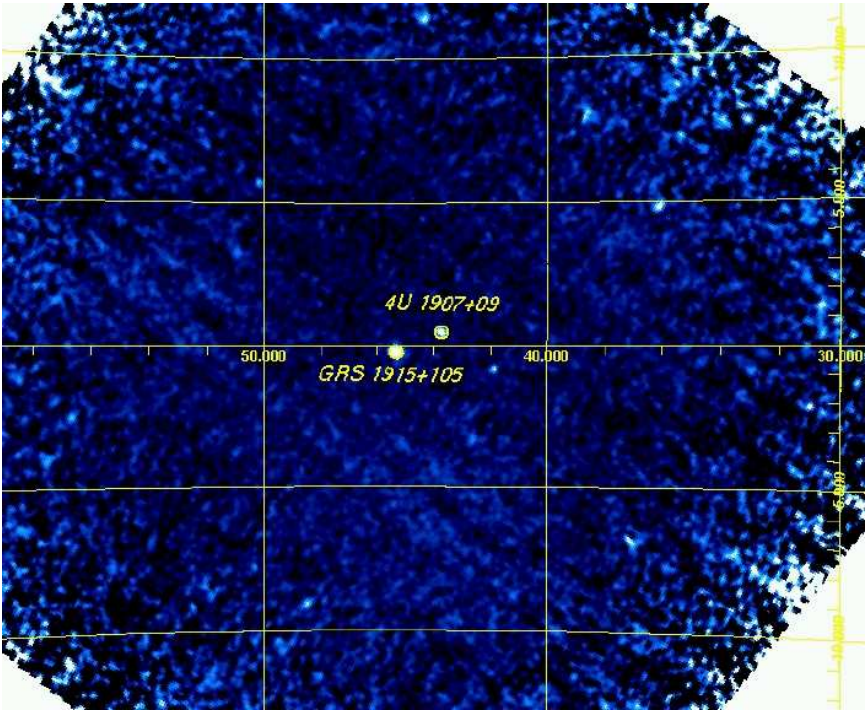


Figure 7.2: ISGRI image of the 4U 1907+09 region in the 20–40 keV band (exposure time about 100 ksec, data from revolution 246).

we fixed it to 2 eV, corresponding to an equivalent width of 136 eV.

To exclude the possibility that the CRSFs are due to incorrect modeling of the continuum, we also used other continuum models[1] including the NPEX model, which consists of negative and positive power-laws with a common exponential cutoff factor (Mihara 1995):

$$C(E) = A_1 \left(E^{-\alpha_1} + A_2 \cdot E^{+\alpha_2}\right) \exp\left(-\frac{E}{E_{\mathrm{fold}}}\right) \tag{7.2}$$

Using an absorbed NPEX model, we obtain $\chi^2_{\mathrm{red}} = 4.54$ and also observe line like features at 19 and 40 keV. Again we first fitted only one feature at 44.4 keV, resulting in a $\chi^2_{\mathrm{red}} = 2.56$. Fitting these features with two Gaussians at 42.0 keV

[1] We did not use the `highecut` model due to the artificial features introduced in the fit residuals by the abrupt onset of the cutoff (Kretschmar et al. 1997; Kreykenbohm et al. 1999).

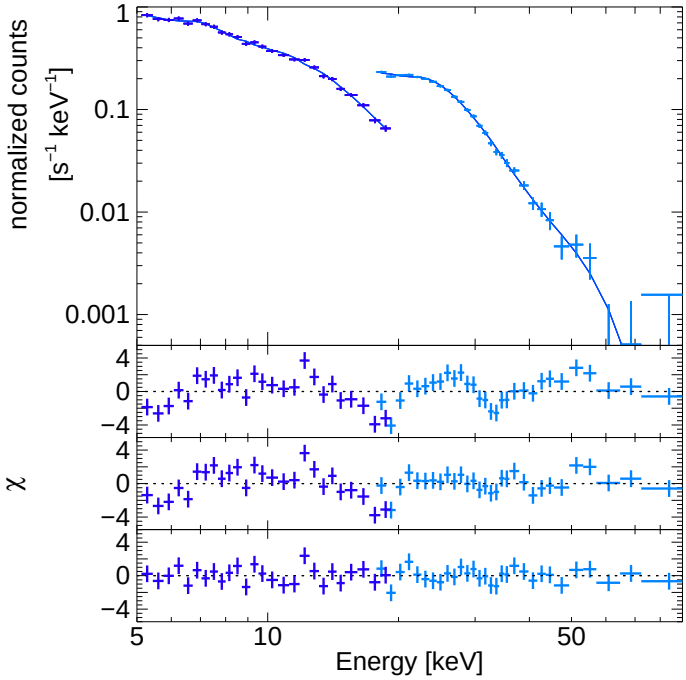


Figure 7.3: Fit to the data using the Fermi-Dirac cutoff model including 2 cyclotron lines. The bottom panels show the residuals, from top to bottom the case without lines, with 1 line, and with 2 cyclotron lines.

and 18.7 keV improves the fit significantly resulting in $\chi^2_{\rm red} = 1.16$ ($F$-Test: $8.7 \times 10^{-13}$). See Table 7.4 for the complete set of model parameters. With the NPEX model it was not possible to constrain the Fe-line, however the upper limit for a line with the same energy and sigma as in the Fermi-Dirac cutoff model is $9.7\,10^{-4}$ photons cm$^{-2}$ s$^{-1}$, consistent with the results obtained for the continuum with a Fermi-Dirac cutoff. The continuum and line parameters measured with *INTEGRAL* are consistent with the *BeppoSAX* results (Cusumano et al. 1998). Our measurements also confirm the *BeppoSAX* result that in this source the second line is deeper than the fundamental line, a fact that can be explained by "photon spawning". From our spectral fitting we obtain an average flux of $2.6\,10^{-10}$ erg cm$^{-2}$ s$^{-1}$ in the 20–40 keV band.

Table 7.3: Best fit parameters for the Fermi-Dirac cutoff model. Shown are the best-fit absorbing column, $N_{\rm H}$, the photon index, $\Gamma$, the flux at 1 keV, $A$, the cut-off energy, $E_{\rm cut}$, the folding energy, $E_{\rm fold}$, and the cyclotron line parameters (energy, $E_{\rm cyc}$, depth $D_{\rm cyc}$, and width, $\sigma_{\rm cyc}$), and the reduced $\chi^2$ and the number of degrees of freedom, dof. All uncertainties are at the 90% level for one interesting parameter.

| | fdcut | | |
|---|---|---|---|
| | without line | with 1 line | with 2 lines |
| $N_{\rm H}$ [$10^{22}$ cm$^{-2}$] | $3^{+7}_{-3}$ | $10^{+6}_{-7}$ | $0^{+7}_{-0}$ |
| $\Gamma$ | $2.01^{+0.17}_{-0.10}$ | $2.21^{+0.15}_{-0.17}$ | $1.67^{+0.39}_{-0.09}$ |
| $A$ | $0.21^{+0.13}_{-0.05}$ | $0.34^{+0.20}_{-0.13}$ | $0.11^{+0.03}_{-0.03}$ |
| $E_{\rm cut}$ [keV] | $31^{+1}_{-1}$ | $37^{+6}_{-3}$ | $30^{+5}_{-8}$ |
| $E_{\rm fold}$ [keV] | $5^{+1}_{-1}$ | $4^{+1}_{-1}$ | $7^{+3}_{-2}$ |
| $E_{\rm cyc,1}$ [keV] | – | – | $18.9^{+0.6}_{-0.7}$ |
| $D_{\rm cyc,1}$ | – | – | $0.35^{+0.10}_{-0.09}$ |
| $\sigma_{\rm cyc,1}$ [keV] | – | – | $3.0^{+1.0}_{-0.7}$ |
| $E_{\rm cyc,2}$ [keV] | – | $36.0^{+3.6}_{-2.4}$ | $39.8^{+4.0}_{-2.7}$ |
| $D_{\rm cyc,2}$ | – | $0.7^{+0.6}_{-0.2}$ | $0.9^{+0.2}_{-0.4}$ |
| $\sigma_{\rm cyc,2}$ [keV] | – | $3.7^{+2.1}_{-2.2}$ | $9.0^{+2.7}_{-3.3}$ |
| $E_{\rm Fe}$ [keV] | – | – | $7.1^{+0.3}_{-0.3}$ |
| $\sigma_{\rm Fe}$ [eV] | – | – | 2 (fixed) |
| $A_{\rm Fe}$ [$10^{-4}$] | – | – | $6^{+3}_{-3}$ |
| $\chi^2$/dof | 154.91/50 | 116.82/47 | 41.90/42 |
| $\chi^2_{\rm red}$ | 3.10 | 2.49 | 1.00 |

## *7.4 Timing Analysis*

### *7.4.1 The X-ray light curve of 4U 1907+09*

The X-ray light curve of 4U 1907+09 shows a clearly pulsed signal with a period of ~441 s. The mean count rates in the 20–40 keV band for our observations are shown in Table 7.2. The variations in count rate largely reflect the orbital phase dependent variability (Fig. 7.1).

Table 7.4: Best fit parameters for the `npex` model, i.e., the photon index of the lower energy power-law, $\alpha_1$ (the positive power-law index, $\alpha_2$, was fixed at 2.0), the power-law normalizations $A_1$ and $A_2$ as defined in Eq. 7.2, and the folding energy $E_{\rm fold}$. All other symbols have the same meaning as in Table 7.3.

| | npex | | |
|---|---|---|---|
| | without line | with 1 line | with 2 lines |
| $N_{\rm H}$ [$10^{22}$cm$^{-2}$] | $1^{+8}_{-1}$ | $4^{+9}_{-4}$ | $3^{+7}_{-3}$ |
| $\alpha_1$ | $0.88^{+0.20}_{-0.13}$ | $0.98^{+0.22}_{-0.15}$ | $0.87^{+0.29}_{-0.20}$ |
| $A_1$ [$10^{-2}$] | $9^{+7}_{-1}$ | $9^{+7}_{-3}$ | $8^{+7}_{-3}$ |
| $A_2$ [$10^{-4}$] | $7^{+1}_{-3}$ | $2^{+1}_{-1}$ | $6^{+6}_{-3}$ |
| $E_{\rm fold}$ [keV] | $4.85^{+0.04}_{-0.03}$ | $6.21^{+0.08}_{-0.10}$ | $5.16^{+0.76}_{-0.33}$ |
| $E_{\rm cyc,1}$ [keV] | – | – | $18.7^{+0.6}_{-0.8}$ |
| $D_{\rm cyc,1}$ | – | – | $0.32^{+0.20}_{-0.08}$ |
| $\sigma_{\rm cyc,1}$ [keV] | – | – | $2.8^{+1.1}_{-0.9}$ |
| $E_{\rm cyc,2}$ [keV] | – | $44.4^{+2.5}_{-2.0}$ | $42.0^{+5.1}_{-3.6}$ |
| $D_{\rm cyc,2}$ | – | $1.32^{+0.37}_{-0.29}$ | $0.77^{+0.78}_{-0.37}$ |
| $\sigma_{\rm cyc,2}$ [keV] | – | $7.0^{+1.5}_{-1.2}$ | $7.8^{+4.6}_{-2.7}$ |
| $\chi^2$/dof | 227.05/50 | 120.46/47 | 50.88/44 |
| $\chi^2_{\rm red}$ | 4.54 | 2.56 | 1.16 |

4U 1907+09 is also known to exhibit flares on a timescale of hours (Makishima et al. 1984; in 't Zand et al. 1998; Mukerjee et al. 2001). We observed four such flares with count rate increases of at least $5\sigma$ over its normal level (Fig. 7.4). Three of them, in revolutions 187, 193, and 305, are associated with the main peak in the orbital light curve (Fig. 7.1) while the flare observed in revolution 188 is linked to the secondary peak. Table 7.5 shows an overview of the properties of these flares.

During flares, in 't Zand et al. (1998) and Mukerjee et al. (2001) also reported the detection of transient 18.2 s and 14.4 s quasi-periodic oscillations (QPOs). We therefore considered to calculate dynamical power spectra for the flare light curves to search for similar oscillations, however, simulated light curves showed that our *INTEGRAL* data are not sensitive enough to detect a QPO at the reported levels.

Table 7.5: Flares in the X-ray light curve of 4U 1907+09. The peak rates are quoted for a 441 s binned light curve in the 20–40 keV band.

| Revolution | Center of Flare MJD | Duration sec | $\Phi_{\rm orb}$ | Peak Rates IBIS cts s$^{-1}$ |
|---|---|---|---|---|
| 187 | 53121.65 | 7000 | 0.63 | 18.09 |
| 188 | 53125.03 | 5000 | 0.03 | 12.11 |
| 193 | 53138.21 | 7000 | 0.61 | 22.56 |
| 305 | 53472.93 | 2500 | 0.57 | 13.88 |

### *7.4.2 Pulsar Period and Pulse Profiles*

It is possible to track the evolution of the pulse period of 4U 1907+09 for more than 20 years. Since the first measurements, the source showed a steady spin down rate of $\dot{P}_{\rm pulse} = +0.225\,{\rm s\,yr}^{-1}$ (in 't Zand et al. 1998). A recent analysis of *RXTE* data, however, taken during MJD 51980–52340 showed a spin down rate which is 0.5 times lower than the previous value (Baykal et al. 2006). Using our *INTEGRAL* data, we can extend the pulse period evolution to the years 2003–2005 (MJD 52739–53504).

To measure the pulse period of 4U 1907+09 we first performed epoch folding (Leahy et al. 1983) on each revolution separately. Using these periods we derived pulse profiles for each revolution using the respective period. The pulse profiles were then fitted by a sum of sine functions to determine the position of the trailing edge (see for example Fig 7.7 at phase 1.0) of the pulse to obtain absolute pulse arrival times and the differences between the arrival times of adjacent revolutions. From these time differences the approximate number of pulse cycles between those absolute times was determined. For sufficiently well sampled observations, those values are close to an integer number. These integer numbers are then taken to count the cycles throughout those well sampled subsets, and a model can be constructed to calculate expected pulse arrival times (trailing edges). The observed times can then be compared with the calculated times and a polynomial fit to the observed times yields values for the period and its derivative. Care was taken that within subsets no miscounting was possible. Between subsets the time gaps are too large such that they cannot be bridged uniquely and no statement about the period development during the gaps can be made. Using this procedure we were able to derive 12 periods with sufficient accuracy (see Table 7.6).

Fig. 7.5 shows the long-time history of the period evolution based on all available data. The overplotted line indicates the historic spin down trend with $\dot{P}_{\rm pulse} = +0.225\,{\rm s\,yr}^{-1}$ from in 't Zand et al. (1997). The recent periods obtained by Baykal et al. (2006) show a clear deviation from the historic spin down trend. The periods

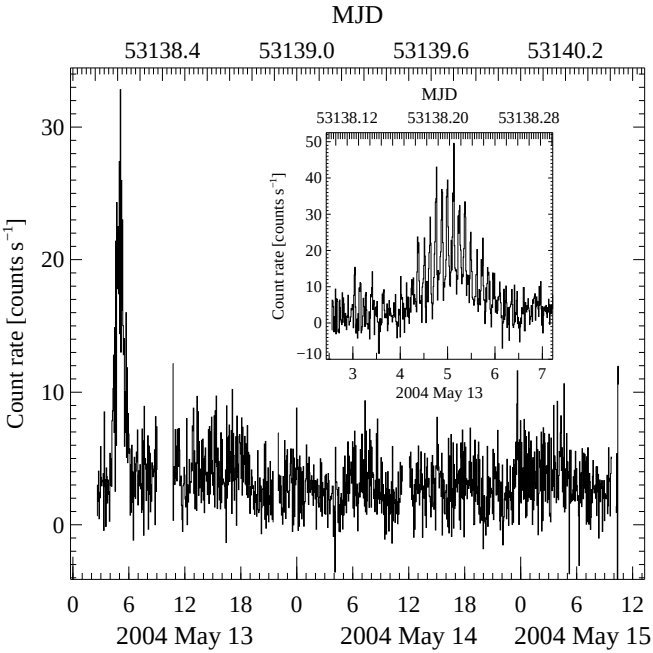


Figure 7.4: IBIS (ISGRI) 20–40 keV light curve of revolution 193. The bin time is 200 s. The inset shows a close up of the flare, the bin time in this case is 40 s. X-axis numbers are hours.

obtained from *INTEGRAL* (shown as diamonds), not only confirm this change of the trend but show a complete trend reversal from the historic long term spin down trend to a spin up trend from MJD 53131 onwards (see Figs. 7.5 and 7.6).

We tried several models to fit this overall period evolution[2]. The description of the data by three distinct episodes with a linear spin down from MJD 45576 to MJD 50290 ($\dot{P}_{\rm pulse} = +0.235 \pm 0.001\,{\rm s\,yr^{-1}}$), a parabolic turnover from MJD 50290 to MJD 53022 of the form $P(T) = P_0 + \dot{P}_{\rm pulse,0}(T - T_0) + \ddot{P}_{\rm pulse,0}(T - T_0)^2/2$ with $T_0$ = MJD 51321, $\dot{P}_{\rm pulse,0} = +0.121 \pm 0.001\,{\rm s\,yr^{-1}}$ and $\ddot{P}_{\rm pulse,0} = -(7.743 \pm 0.002)$ $10^{-3}\,{\rm s\,yr^{-2}}$ , and a linear spin up ($\dot{P}_{\rm pulse} = -0.147 \pm 0.006\,{\rm s\,yr^{-1}}$) from MJD 53022 onwards resulted in $\chi^2_{\rm red} = 8.74$ for 34 degrees of freedom. Modeling the period evolution of 4U 1907+09 with four distinct episodes of different, but constant, $\dot{P}$ results in a slightly better $\chi^2_{\rm red}$ ($\chi^2_{\rm red} = 7.2$ for 34 dof, see Figs. 7.5 and 7.6).

[2]For this analysis we excluded the two period measurements by *IXAE* (Mukerjee et al. 2001) as outliers. Including them resulted in $\chi^2_{\rm red}$ values increased by a factor of 5.

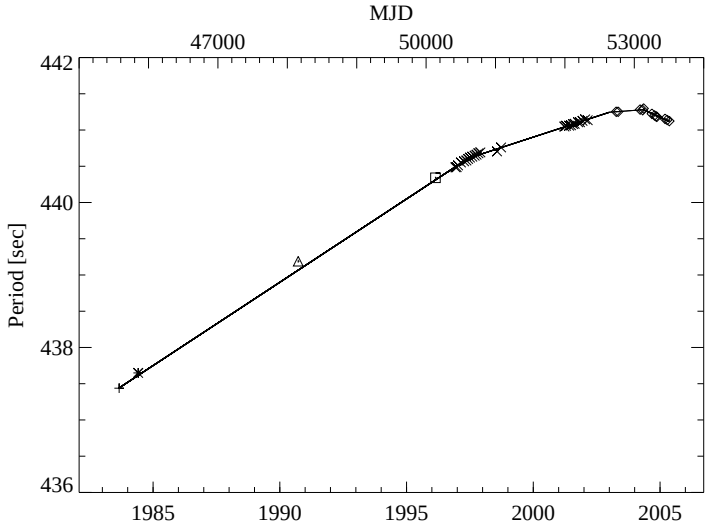


Figure 7.5: Evolution of the 4U 1907+09 pulse period over the last 20 years. Diamonds indicate the results obtained in this work, other symbols indicate data from Makishima et al. (1984, plus-signs), Cook & Page (1987, asterixes), Mihara (1995, triangles), in 't Zand et al. (1998, squares), and Baykal et al. (2001, 2006, crosses). From MJD 51980 onwards 4U 1907+09 shows a clear deviation from the long term spin down trend with a complete reversal to a spin up after MJD 53131. The solid line shows the fit of four distinct episodes of different, but constant, $\dot{P}$.

The four episodes are the historic spin down with $\dot{P}_{\rm pulse} = +0.230 \pm 0.001\,{\rm s\,yr^{-1}}$ (MJD 45576 to MJD 50610), the turnover with $\dot{P}_{\rm pulse} = +0.114 \pm 0.001\,{\rm s\,yr^{-1}}$ from MJD 50610 to MJD 52643 and $\dot{P}_{\rm pulse} = +0.026 \pm 0.003\,{\rm s\,yr^{-1}}$ from MJD 52643 to MJD 53131, and finally the spin up with $\dot{P}_{\rm pulse} = -0.158 \pm 0.007\,{\rm s\,yr^{-1}}$.

Using the derived periods, pulse profiles for all revolutions were determined (Fig. 7.7) by folding the light curves with the best respective periods. No change in the shape of the pulse profile is detectable, and the *INTEGRAL* pulse profiles before and after the reversal of $\dot{P}$ are consistent with each other. In addition, we also obtained energy resolved pulse profiles (see Fig. 7.8 for an example). Again, the evolution of the pulse profile from below 30 keV to high energies is identical for all revolutions: the profile exhibits a single peak at all energies with only a small secondary hump, indicating the potential presence of a second peak at energies $\lesssim$20 keV, where a clear double peaked pulse profile was observed previously (Makishima et al. 1984; Cook & Page 1987; in 't Zand et al. 1998). At energies

Table 7.6: Period measurements of 4U 1907+09.

| Date MJD | Instrument | Pulse Period s | Reference |
|---|---|---|---|
| 45576.5 | *Tenma* | $437.438 \pm 0.004$ | Makishima et al. (1984) |
| 45850.7 | *EXOSAT* | $437.649 \pm 0.019$ | Cook & Page (1987) |
| 48156.6 | *Ginga* | $439.19 \pm 0.02$ | Mihara (1995) |
| 50134.8 | *RXTE* | $440.341 \pm 0.014$ | in 't Zand et al. (1998) |
| 50302.0 | *IXAE* | $440.53 \pm 0.01$ | Mukerjee et al. (2001) |
| 50424.3 | *RXTE* | $440.4854 \pm 0.0109$ | Baykal et al. (2006) |
| 50440.4 | *RXTE* | $440.4877 \pm 0.0085$ | Baykal et al. (2001) |
| 50460.9 | *RXTE* | $440.5116 \pm 0.0075$ | Baykal et al. (2006) |
| 50502.1 | *RXTE* | $440.5518 \pm 0.0053$ | Baykal et al. (2006) |
| 50547.1 | *RXTE* | $440.5681 \pm 0.0064$ | Baykal et al. (2006) |
| 50581.1 | *RXTE* | $440.5794 \pm 0.0097$ | Baykal et al. (2006) |
| 50606.0 | *RXTE* | $440.6003 \pm 0.0115$ | Baykal et al. (2006) |
| 50631.9 | *RXTE* | $440.6189 \pm 0.0089$ | Baykal et al. (2006) |
| 50665 | *IXAE* | $440.95 \pm 0.01$ | Mukerjee et al. (2001) |
| 50665.5 | *RXTE* | $440.6323 \pm 0.0069$ | Baykal et al. (2006) |
| 50699.4 | *RXTE* | $440.6460 \pm 0.0087$ | Baykal et al. (2006) |
| 50726.8 | *RXTE* | $440.6595 \pm 0.0105$ | Baykal et al. (2006) |
| 50754.1 | *RXTE* | $440.6785 \pm 0.0088$ | Baykal et al. (2006) |
| 50782.5 | *RXTE* | $440.6910 \pm 0.0097$ | Baykal et al. (2006) |
| 51021.9 | *RXTE* | $440.7045 \pm 0.0032$ | Baykal et al. (2001) |
| 51080.9 | *RXTE* | $440.7598 \pm 0.0010$ | Baykal et al. (2001) |
| 51993.8 | *RXTE* | $441.0484 \pm 0.0072$ | Baykal et al. (2006) |
| 52016.8 | *RXTE* | $441.0583 \pm 0.0071$ | Baykal et al. (2006) |
| 52061.5 | *RXTE* | $441.0595 \pm 0.0063$ | Baykal et al. (2006) |
| 52088.0 | *RXTE* | $441.0650 \pm 0.0063$ | Baykal et al. (2006) |
| 52117.4 | *RXTE* | $441.0821 \pm 0.0062$ | Baykal et al. (2006) |
| 52141.2 | *RXTE* | $441.0853 \pm 0.0082$ | Baykal et al. (2006) |
| 52191.4 | *RXTE* | $441.1067 \pm 0.0046$ | Baykal et al. (2006) |
| 52217.2 | *RXTE* | $441.1072 \pm 0.0077$ | Baykal et al. (2006) |
| 52254.3 | *RXTE* | $441.1259 \pm 0.0074$ | Baykal et al. (2006) |
| 52292.0 | *RXTE* | $441.1468 \pm 0.0065$ | Baykal et al. (2006) |
| 52328.8 | *RXTE* | $441.1353 \pm 0.0090$ | Baykal et al. (2006) |
| 52739.3 | *INTEGRAL* | $441.253 \pm 0.005$ | this work |
| 52767.1 | *INTEGRAL* | $441.253 \pm 0.005$ | this work |
| 53083.9 | *INTEGRAL* | $441.283 \pm 0.005$ | this work |
| 53121.1 | *INTEGRAL* | $441.274 \pm 0.005$ | this work |
| 53133.4 | *INTEGRAL* | $441.297 \pm 0.005$ | this work |
| 53253.6 | *INTEGRAL* | $441.224 \pm 0.010$ | this work |
| 53291.3 | *INTEGRAL* | $441.201 \pm 0.005$ | this work |
| 53314.0 | *INTEGRAL* | $441.188 \pm 0.005$ | this work |
| 53324.7 | *INTEGRAL* | $441.183 \pm 0.005$ | this work |
| 53443.4 | *INTEGRAL* | $441.154 \pm 0.005$ | this work |
| 53473.3 | *INTEGRAL* | $441.139 \pm 0.005$ | this work |
| 53503.8 | *INTEGRAL* | $441.124 \pm 0.005$ | this work |

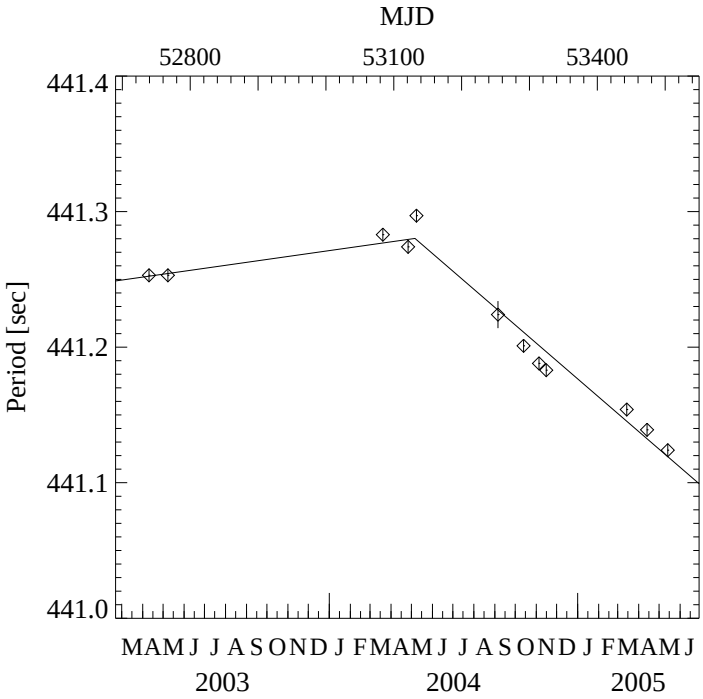


Figure 7.6: Close up of the periods found in this work. Between MJD 52643 to MJD 53131 the derived pulse periods show a spin down of the source with $\dot{P}_{\rm pulse} = +0.026\,{\rm s\,yr^{-1}}$. After MJD 53131 the accretion torque changes sign and 4U 1907+09 spins up with $\dot{P}_{\rm pulse} = -0.158\,{\rm s\,yr^{-1}}$. The line indicates the linear fit to the periods as described in the text.

above 60 keV, the source gets too faint and no pulsed emission is observable.

## *7.5 Summary and Discussion*

Since 2003, 4U 1907+09 was observed frequently with *INTEGRAL*. In this chapter the results of the timing analysis of ~2280 ksec of IBIS data and of the spectral analysis of 1258 ksec of IBIS and 200 ksec of JEM-X2 data are presented. Two cyclotron lines at ~19 keV and ~40 keV are detected, consistent with earlier *Ginga* and *BeppoSAX* results (Mihara 1995; Cusumano et al. 1998). Assuming a gravitational redshift of $z = (1-(2GM/rc^2))^{-1/2} - 1 = 0.31$ (assuming $M = 1.4{\rm M}_\odot$ and $r = 10^6$ cm), from these CRSF observations a $B$-field strength of $2.15 \times 10^{12}$ G can

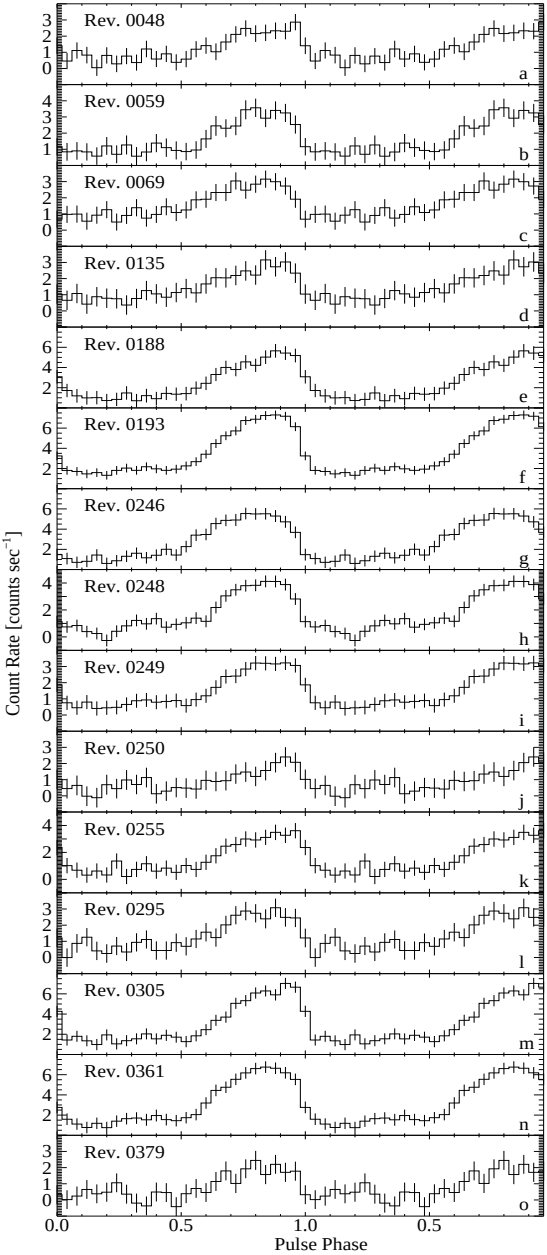


Figure 7.7: Pulse profiles for different revolutions in the 20–40 keV band. Panels a–e show pulse profiles obtained during the period of spin down, and panels f–o show spin up pulse profiles.

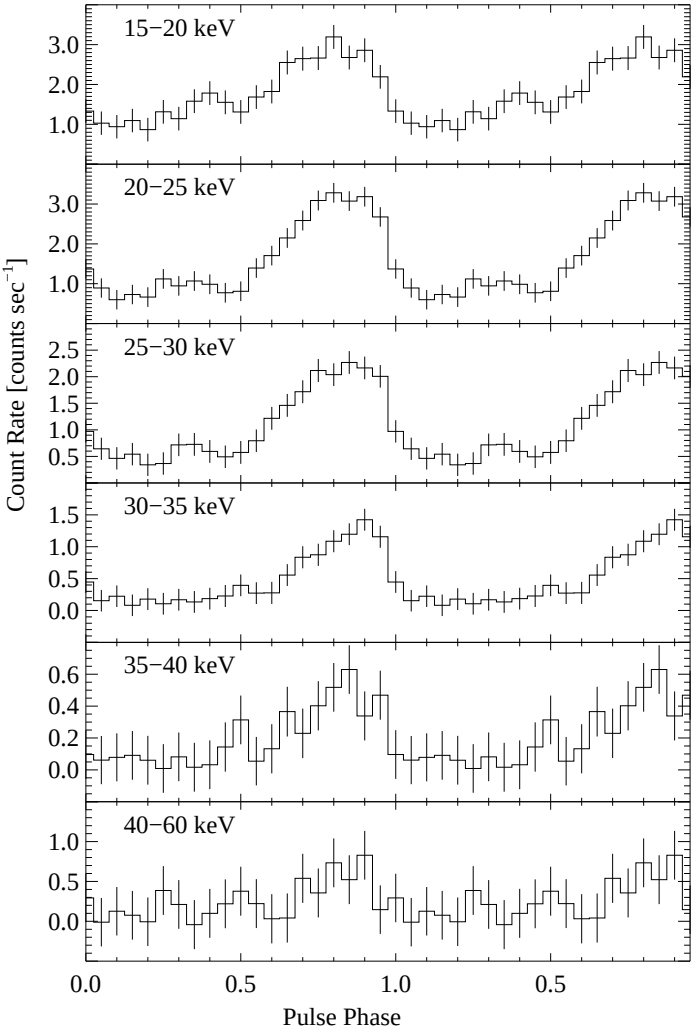


Figure 7.8: Energy resolved pulse profiles for revolution 193 ($P_{\rm pulse}$ = 441.224 s).

be inferred. Four flares in the X-ray light curves with durations between ∼2500 s and ∼7000 s were observed, three of which are associated with the primary flare in the orbital light curve of 4U 1907+09.

In addition to these confirmations of earlier results, our *INTEGRAL* data show,

for the first time, a clear spin up phase in 4U 1907+09 (Table 7.6 and in Figs. 7.5 and 7.6). After almost 20 years of constant spin down at a rate of $\dot{P}_{\rm pulse} = +0.225\,{\rm s\,yr^{-1}}$, with the available data being consistent with $\ddot{P} = 0\,{\rm s^{-1}}$, in 2002 and 2003 first indications for a decrease in the magnitude of spin down were detected (Baykal et al. 2006). As shown in Sect. 7.4.2, the new *INTEGRAL* data show a torque reversal from ∼MJD 53131 onwards, with the source now exhibiting a spin up with a rate of $\dot{P}_{\rm pulse} = -0.158\,{\rm s\,yr^{-1}}$. So far, the *INTEGRAL* results appear to be consistent with $\ddot{P} = 0\,{\rm s^{-1}}$ (the $1\sigma$ upper limit for $\ddot{P}$ during the spin up is $-4\,10^{-5}\,{\rm s^{-1}\,yr^{-2}}$).

The traditional interpretation of spin up in X-ray binaries with a strongly magnetized, disk-accreting neutron star is that the accretion disk is truncated at the inner edge of the disk by the magnetic field of the neutron star (see the description in section 6.2 and for a more detailed description, e.g., Ghosh et al. 1977; Ghosh & Lamb 1979a,b, and references therein). For prograde disks, the magnetic coupling between the accretion disk and the neutron star and the transfer of angular momentum from the accreted matter onto the neutron star will lead to a torque onto the neutron star resulting in spin up. The general expectation of these models is that the accretion disk is close to equilibrium, i.e., the Alfvén or magnetospheric radius, $r_{\rm m}$, where the accretion flow couples to the magnetic field, is assumed to be close to the corotation radius, $r_{\rm co}$, where the disk's Kepler frequency equals the rotational frequency of the neutron star. For accretion to occur, $r_{\rm m} \lesssim r_{\rm co}$, as otherwise the onset of the centrifugal barrier (the "propeller effect") prevents the material from falling onto the neutron star (Illarionov & Sunyaev 1975).

Most accreting neutron star systems, such as Her X-1 or Vela X-1, show a secular spin up or spin down trend onto which short, large magnitude episodes of spin down or spin up are superimposed (Bildsten et al. 1997). These shorter episodes are often interpreted to be due to short term variations in $\dot{M}$, which give rise to short-term torque fluctuations. In contrast to these systems, GX 1+4, 4U 1626−67, and 4U 1907+09 showed decade-long phases where $\dot{P}$ did not change its sign. GX 1+4 was seen to spin up with a very short characteristic timescale, $P/\dot{P} \sim$ 40 years, from the early 1970s until the source flux dropped below detectability in the *EXOSAT* era of the early 1980s. From 1985 onwards the source reemerged with a strong spin down (Makishima et al. 1988; Mony et al. 1991; Chakrabarty et al. 1997). Recent *INTEGRAL* observations show that this spin down has continued until at least 2004 (Ferrigno et al. 2007). A second source with a long phase of unchanged sign of $\dot{P}$ is the ultracompact low mass X-ray binary 4U 1626−67, which was spinning up between 1977 and 1989, followed by a torque reversal and an extended spin down phase starting in 1991 (Chakrabarty et al. 1997). In contrast to GX 1+4, no luminosity drop was seen during the torque reversal and

with $|P/\dot{P}| \sim 5000$ years the characteristic spin up and spin down timescales are significantly larger. Provided that the torque reversal of 4U 1907+09 described in this chapter does not change back in the next years, in its overall period behavior, 4U 1907+09 resembles 4U 1626−67: both sources have $|P/\dot{P}| \sim$ several thousands of years and no change in luminosity was observed during the torque reversal. On the other hand, however, 4U 1907+09 is a high mass X-ray binary with a much longer orbital period, and thus shares similarities with the low mass X-ray binary GX 1+4, and furthermore 4U 1907+09 switched from spin down to spin up, while GX 1+4 and 4U 1626−67 switched from spin up to spin down. Common for the three sources is that the magnitude of $|P/\dot{P}|$ is similar for the spin up and the spin down.

With the simple magnetic torquing model outlined above, the long distinct episodes of roughly constant $\dot{P}$ and the magnitude and sign of $\dot{P}$ are difficult to explain: As discussed above, for systems close to equilibrium it is expected that $r_{\rm m} \sim r_{\rm co}$. In reality, however, this is not the case. In the case of 4U 1907+09, it was first pointed out by in 't Zand et al. (1998) that the magnetospheric radius inferred from the cyclotron line measurements is $r_{\rm m} \sim 2400$ km, while $r_{\rm co} \sim 12000$ km. Moving $r_{\rm m}$ out to $r_{\rm co}$ would require a magnetic field of $\sim 10^{14}$ G, which is two orders of magnitude larger than the magnetic field deduced from the observed cyclotron lines. Alternatively, $\dot{M}$ could be significantly lower than the value inferred from the X-ray luminosity of the system. Assuming the efficiency of accretion is comparable to other systems, however, a low $\dot{M}$ would imply a significantly smaller distance to 4U 1907+09 than allowed by its optical reddening, which seems equally unlikely. in 't Zand et al. (1998) argued that the presence of quasi-periodic oscillations (QPOs) and the long term systematic trend in the spin down are strong indicators for the presence of a accretion disk in the system with a small inner disk radius. In analogy to GX 1+4 (Chakrabarty et al. 1997, and references therein), these authors show that a transient retrograde disk with a duty cycle of 1–5% could provide a sufficiently strong torque to explain the observed spin down. This torquing would coincide with a short term increase of source luminosity. in 't Zand et al. (1998) speculate that the X-ray flares indicate the presence of the retrograde disk, since a switch to a retrograde disk would imply an increase in X-ray luminosity. They point out, however, that the ∼1000 s duration of the flares seen in their *RXTE* data is too small with respect to the required duty cycle for a retrograde disk. We note that the *INTEGRAL* results show flare durations of several ksec duration (Tab. 7.5), which is more in line with the expected duty cycle. Furthermore, the folded light curve of 4U 1907+09 indicates a brightening of the source around phase 0.6 (Fig. 7.1). With $0.1P_{\rm orb}$ duration, this flare is long enough to easily accommodate the required duty cycle of the retrograde disk and to explain the observed $\dot{P}$. We note, however, that not all of the brightening seen

in Fig. 7.1 is due to the flares identified by us as removing these flares from the data still results in a clear peak at phase 0.6 in the folded light curve. Part of the brightening could therefore be also due to an enhanced $\dot{M}$ during this phase of the elliptical orbit of the neutron star, although we cannot firmly exclude the presence of smaller flares which would not be picked up due to our conservative definition of a flare.

While the model of a retrograde disk can explain the magnitude of $P/\dot{P}$, it is more difficult to reconcile the torque reversal found with *INTEGRAL* with this model. First of all, as discussed above, the four intervals of different $\dot{P}$ represent distinct episodes of different torques on the neutron star. In the retrograde disk model, it is difficult to understand why the characteristic spin up and spin down timescales appear so similar. Furthermore, these three phases would then correspond to different duty cycles of the retrograde disk, resulting in a change in observed flux. Such a behavior has been observed, e.g., in GX 1+4, where torque and luminosity are correlated during the spin down phase (Chakrabarty et al. 1997). No such correlations are observable in 4U 1907+09, where the flux has not appreciably changed during the *INTEGRAL* and the pointed *RXTE* observations (see also Baykal et al. 2006). In addition, an analysis of the orbit-averaged 2–12 keV *RXTE* ASM light curves also does not reveal a change in the soft X-ray behavior of the source, and neither is a change in the X-ray light curve with orbital phase observed.

The *INTEGRAL* observations also rule out the application of the torque reversals put forward by Murray et al. (1999) to explain GX 1+4. In this model, the accretion disk is assumed to consist of several rings with opposite rotation. Between these rings a gap is created such that a torque reversal should be accompanied by a minimum in the accretion luminosity. The model predicts a change in pulse profile from "leading-edge bright" during the spin down to "trailing-edge bright" during the spin up. Both, a minimum in luminosity and a change in the shape of the pulse profile are observed in GX 1+4 (Greenhill et al. 1999), but neither effect is present in 4U 1907+09 (see discussion above and Fig. 7.7).

Recently, Perna et al. (2006) presented a new *Ansatz* to explain torque changes in accreting neutron stars, which does not require the presence of retrograde disks. This model makes use of the fact that X-ray pulsars are oblique rotators, i.e., the neutron star's magnetic field is tilted by an angle $\chi$ with respect to the axis of rotation of the neutron star. Assuming the accretion disk is situated in the neutron star's equatorial plane, for a ring of matter in the accretion disk, the magnetic field strength then depends on the azimuthal angle and thus the boundary of the magnetosphere is asymmetric. As shown by Perna et al. (2006), such a configuration can lead to regions in the disk where the propeller effect is locally at work, while accretion from other regions is not inhibited (i.e., on a ring on the disk, there are

some regions with $r_m < r_{co}$ and other regions with $r_m > r_{co}$). This results in a non-linear dependence of the accretion luminosity from the $\dot{M}$ through the outer parts of the disk. A nontrivial consequence of this more realistic accretion geometry is that for values of $\chi$ greater than a critical value, $\chi_{crit}$, limit cycles are present, where cyclic torque reversal episodes are possible without a change in $\dot{M}$. For typical parameters. $\chi_{crit}$ is between ~25° and ~45°. We stress that the existence of the limit cycles depends only on $\chi$ and on the pulsar's polar magnetic field, $B$, and no variation of external parameters is required to trigger torque reversals. This fact is a big advantage of this model over the models discussed above.

Perna et al. (2006) show that their model can explain the principal observed properties of GX 1+4, including the luminosity drop during torque reversal, except for the observed correlation between torque and luminosity during the spin down phase. For 4U 1626−67, assuming $B = 2.5 \times 10^{12}$ G and $\chi = 68°$, all observed properties of the spin history of 4U 1626−67 including the large and values of $|P/\dot{P}|$ before and after the torque reversal and the virtually unchanged luminosity of the source can be explained (in the model, the required change in luminosity is only ~5%). For these model parameters, the limit cycle of 4U 1626−67 is predicted to have a long period.

The similarity between the pulse histories of 4U 1907+09 and 4U 1626−67 suggests that a similar model would also work for the former source. We stress, however, that further quantitative work, which is outside the scope of this work, is clearly required. Specifically, from a theoretical point of view we note that the model of Perna et al. (2006) does not yet take changes in $\dot{M}$ due to the orbital eccentricity into account and that the current version of the model assumes the disk to be flat and in the equatorial plane of the neutron star, while more realistic disks onto magnetized objects can be expected to be warped and precessing (e.g., Pfeiffer & Lai 2004, and therein). From an observational point of view, the donor stars in both systems are very different, with 4U 1626−67 being a low mass and 4U 1907+09 being a high mass system. Finally, we also emphasize that the torque reversal in 4U 1626−67 was from a spin up to a spin down, while for 4U 1907+09 it was from a spin down to a spin up. Since the torque reversal episodes are cyclic, however, we do not expect this latter difference to be of major importance.

In conclusion, the torque reversal of 4U 1907+09 with no associated drop in luminosity and no change in the shape of the pulse profile seem to be difficult to reconcile with models explaining the large $P/\dot{P}$ through the presence of a retrograde disk. On the other hand, the proposal of Perna et al. (2006) to explain torque reversals through accretion onto an oblique rotator seems to be able to explain the long term constancy of $\dot{P}$ trends in 4U 1907+09 and 4U 1626−67, the large magnitude of $|P/\dot{P}|$, and the constancy of X-ray flux over the torque reversal, although further and more detailed theoretical studies are required. As a prediction of the

model for systems such as 4U 1907+09 and 4U 1626−67 is that torque reversal episodes are rare events, further monitoring of the pulse period of 4U 1907+09 is required to determine whether this change is a sign of a long term torque reversal or whether we are just observing a short deviation from a long term spin down trend.

# Part III

# Summary and Outlook

# Chapter 8

# Summary and Outlook

## 8.1 Cygnus X-1

The galactic black hole Cyg X-1 has been observed simultaneously by *INTEGRAL*, *RXTE*, and *XMM-Newton* four times in November/December 2004. The total energy range covered by those three instruments ranges from 2.8 keV to several MeV, i.e., our observations provided one of the best resolved broadband spectra ever obtained for this source. The analysis of the data was split in two main parts:

1. *Analysis of the broadband continuum:* in this part we wanted to constrain models for the Comptonizing plasma. One special aim was the search for effects of non-thermal Comptonization in the spectra. The broadband continuum is also needed to constrain the amount of photons that is Compton reflected off the accretion disk, which is crucial for the second part of the analysis. This study of the broadband continuum was done using *RXTE* and *INTEGRAL*.

2. *Analysis of Fe K$\alpha$ region of the spectrum:* the main goal of this part was to study the structure of the line which is skewed and broadened due to relativistic effects. Along with the line, the shape and the strength of the Fe K edge was analyzed. This was done using *XMM-Newton*.

To observe Cyg X-1 with *XMM-Newton* it was necessary to develop a new observing mode for the EPIC-pn camera, called the "Modified Timing mode". By switching off the EPIC-MOS cameras and increasing the lower energy threshold it is possible to observe sources with luminosities up to ~1 Crab using this mode. Within this thesis, an appropriate response matrix was calculated for the Modified Timing mode, which has been made public through the ESA *XMM-Newton* website. However, there are still some improvements to be made in the future,

as the matrix still lacks the correct treatment of the CTE. The Modified Timing mode could officially be requested in *XMM-Newton* AO7 and four out of eight proposals were accepted by the OTAC.

### *8.1.1 Broadband*

The *RXTE* and *INTEGRAL* data have been modeled using the Comptonization codes `compTT` and `eqpair` as well as a simple phenomenological power-law model. All three approaches resulted in a similar good description of the data in terms of $\chi^2_{\rm red}$. The main results of this analysis are:

- The same spectral parameters found to describe the 3–120 keV *RXTE* range are valid for the extended energy range up to 1 MeV.
- Cyg X-1 was observed in the Hard Intermediate State.
- The four observations show indications for the presence of a hard tail above ~300 keV. This hard tail is confirmed in the time averaged spectrum.

The hard tail can be explained in terms of hybrid thermal/non-thermal Comptonization in the Plasma. The best fit indicated that 67% of the power supplied to the electrons in the plasma is used for the non-thermal acceleration of the electrons.

Another scenario to explain the non-thermal Comptonization would be radiation from a jet in Cyg X-1, which is expected to be present in the Hard Intermediate State. The hard tail may therefore be due to synchrotron self-Comptonization in the jet (Markoff et al. 2003, and references therein). To test this scenario, the jet models of Markoff et al. (2001; 2003) should be applied to the broadband data in a future work.

### *8.1.2 Iron Line*

For the analysis of the iron line region of the spectrum, the *XMM-Newton* data were modeled combined with continuum parameters derived using *RXTE*. The spectral model was composed of an absorbed disk black body and power-law with reflection plus a narrow Gaussian and a relativistically broadened line (using the *XSPEC* models `diskline`, `laor`, and `kdblur`) as well as a smeared edge. The main results of this analysis are:

- The line is clearly composed of a relativistically broadened component and a narrow core.
- An edge component is seen in all observations.

- In terms of $\chi^2_{\rm red}$ Schwarzschild and the Kerr models are similar. However, Kerr models provide inclinations which are physically more meaningful and are therefore slightly favored.

- The line parameters vary with time as well as with luminosity of Cyg X-1 but no clear trend is evident.

The result that Kerr models are slightly favored over the Schwarzschild model is in contradiction with the conclusion derived from Chandra observations that Cygnus X-1 harbors a black hole of no or only modest spin (Miller et al. 2002; Miller 2006). As in the last years more sophisticated models have been developed which also allow to fit the black hole spin parameter *a* (Dovčiak et al. 2004; Brenneman & Reynolds 2006) a logical next step would be to apply them to the *XMM-Newton* data (first tries with the Dovčiak et al. model have not resulted in meaningful parameters so far). Also the combination of the currently used disk models with a new reflection model by Ross & Fabian (2005, 2007) would be very interesting as the reflection hump may extend down to energies in the Fe $K\alpha$ regime.

These new models may also help to understand the observed variability of the spectral parameters. For the variability with time it might also be helpful to split the spectra in shorter parts to follow the evolution more closely (especially in obs3). This analysis should be addressed in a future work.

As soon as the calibration of the CTE effects is finished one could also think of combining at least *XMM-Newton* and *RXTE* (or even also *INTEGRAL*) to a joint fit of the broadband continuum and the relativistic line.

## *8.2 4U 1907+09*

The neutron star binary 4U 1907+09 has been observed by *INTEGRAL* regularly during its so called “Galactic Plane Scans” and “Galactic Central Radian Deep Exposures”. These data, taken between 2003 and 2005, together with private data from a monitoring campaign on the galactic micro-quasar GRS 1915+105 (PI J. Rodriguez) as well as all public available data in the *INTEGRAL* archive, have been studied in the second part of this thesis. The main results of this analysis are:

- While 4U 1907+09 showed a continuous spin-down behavior over the last 20 years (in fact since the first period measurement in 1983), the source underwent a complete torque reversal in 2004 and is spinning-up since then.

- Four flares in the X-ray light curves with durations between ∼2.5 ks and ∼7 ks were observed.

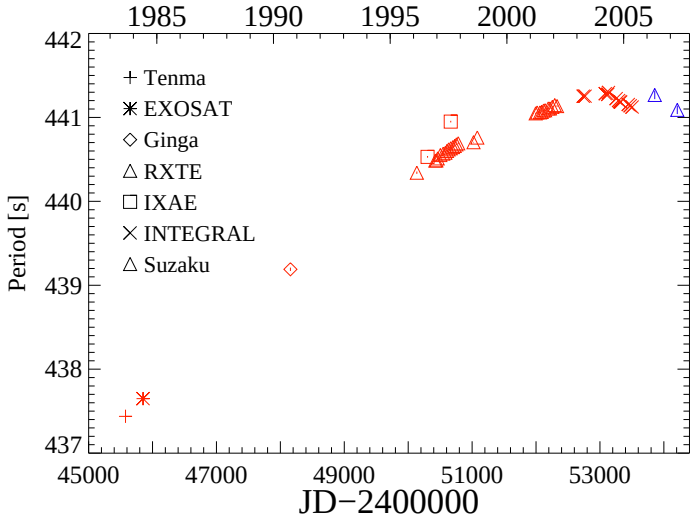


Figure 8.1: Period evolution of 4U 1907+09 including the new Suzaku measurements (Figure from Roth 2008).

- The presence of two cyclotron lines at ~19 keV and ~40 keV, as reported from earlier *Ginga* and *BeppoSAX* observations, could be confirmed.

The observed torque reversal cannot be explained in the classical model by Ghosh and Lamb (Ghosh et al. 1977; Ghosh & Lamb 1979a,b) as the derived magnetospheric radius is too small compared to the corotation radius but the model expects $r_m \sim r_{co}$. Instead the oblique rotator scenario by Perna et al. (2006) was presented as possible explanation for the change in spin behavior. The core statement of this model is the assumption that the boundary of the magnetosphere is asymmetric and therefore there are regions on the disk with $r_m > r_{co}$ while in other regions $r_m < r_{co}$. This leads to the existence of limit cycles which can explain cyclic torque reversal episodes. Applying this model to 4U 1907+09 allows the prediction that the limit cycle will have a long period and no further torque reversal is expected in the near future.

In 2006 and 2007 4U 1907+09 has been observed by the Japanese X-ray satellite Suzaku. While the source showed its typical dipping behavior during the first observation (2006, May 2–3), the second observation (2007, April 19–21) was characterized by flaring. Roth (2008) derived periods for both observations using epoch folding: for the first observation a period of 441.27±0.05 s was found and for the second one a slightly lower value of 441.09±0.05 s. While these two val-

ues show an intrinsic spin-up, the trend compared to the long-term evolution is not so obvious as shown in Fig. 8.1. From these two data points it cannot unambiguously be decided if 4U 1907+09 is continuing its spin-up trend and therefore the Perna et al. model still holds as explanation. A further monitoring of the source is strongly required.

# Bibliography


Abubekerov, M. K., Antokhina, E. A., & Cherepashchuk, A. M. 2004, Astronomy Reports, 48, 550

Akhiezer, A. I. & Berestetskii, V. B. 1965, Quantum Electrodynamics (New York: Interscience)

Albert, J., Aliu, E., Anderhub, H., et al. 2007, ApJL, 665, L51

Alexander, S. G. & Mészáros, P. 1989, ApJ, 344, L1

Bałucińska-Church, M., Church, M. J., Charles, P. A., et al. 2000, MNRAS, 311, 861

Bałucińska-Church, M. & McCammon, D. 1992, ApJ, 400, 699

Bałucińska-Church, M., Takahashi, T., Ueda, Y., et al. 1997, ApJL, 480, L115

Barr, P., White, N. E., & Page, C. G. 1985, MNRAS, 216, 65P

Basko, M. M. & Sunyaev, R. A. 1975, A&A, 42, 311

Basko, M. M. & Sunyaev, R. A. 1976, MNRAS, 175, 395

Baumert, L. D., ed. 1971, Lecture Notes in Mathematics, Springer Verlag, Vol. 182, Cyclic difference sets

Baykal, A., İnam, Ç., Ali Alpar, M., in 't Zand, J., & Strohmayer, T. 2001, MNRAS, 327, 1269

Baykal, A., İnam, S. Ç., & Beklen, E. 2006, MNRAS, 369, 1760

Becker, P. A. & Wolff, M. T. 2005a, ApJL, 621, L45

Becker, P. A. & Wolff, M. T. 2005b, ApJ, 630, 465

Becker, P. A. & Wolff, M. T. 2007, ApJ, 654, 435

Beckwith, K. & Done, C. 2004, MNRAS, 352, 353

Belloni, T. 2005, in American Institute of Physics Conference Series, Vol. 797, Interacting Binaries: Accretion, Evolution, and Outcomes, ed. L. Burderi, L. A. Antonelli, F. D'Antona, T. di Salvo, G. L. Israel, L. Piersanti, A. Tornambè, & O. Straniero, 197–204

Belloni, T., Psaltis, D., & van der Klis, M. 2002, ApJ, 572, 392

Benlloch, S., Pottschmidt, K., Wilms, J., et al. 2004, in American Institute of Physics Conference Series, Vol. 714, X-ray Timing 2003: Rossi and Beyond, ed. P. Kaaret, F. K. Lamb, & J. H. Swank, 61–64

Berestetzki, W. B., Lifschitz, E. M., & Pitajewski, L. P. 1989, Quantenelektrodynamik, 6th edn., Lehrbuch der Theoretischen Physik No. 4 (Berlin: Akademie-Verlag)

Bhattacharya, D. & Srinivasan, G. 1995, in X-ray binaries, p. 495 - 522, 495–522

Bildsten, L., Chakrabarty, D., Chiu, J., et al. 1997, ApJS, 113, 367

Bochkarev, N. G., Karitskaya, E. A., Loskutov, V. M., & Sokolov, V. V. 1986, Soviet Astronomy, 30, 43

Bondi, H. & Hoyle, F. 1944, MNRAS, 104, 273
Bowyer, S., Byram, E. T., Chubb, T. A., & Friedman, H. 1965, Science, 147, 394
Bradt, H. 2004, Astronomy Methods: A Physical Approach to Astronomical Observations (Astronomy Methods, by Hale Bradt. ISBN 0521535514, UK: Cambridge University Press, 2004)
Brandt, S., Budtz-Jørgensen, C., Lund, N., et al. 2003, A&A, 411, L243
Brenneman, L. W. & Reynolds, C. S. 2006, ApJ, 652, 1028
Brocksopp, C., Fender, R. P., Larionov, V., et al. 1999a, MNRAS, 309, 1063
Brocksopp, C., Tarasov, A. E., Lyuty, V. M., & Roche, P. 1999b, A&A, 343, 861
Burderi, L., Di Salvo, T., Robba, N. R., La Barbera, A., & Guainazzi, M. 2000, ApJ, 530, 429
Cadolle Bel, M., Sizun, P., Goldwurm, A., et al. 2006, A&A, 446, 591
Camenzind, M. 2007, Compact objects in astrophysics : white dwarfs, neutron stars, and black holes (Springer-Verlag Berlin, ISBN 9783540257707)
Canuto, V. & Ventura, J. 1977, Fundamentals of Cosmic Physics, 2, 203
Casella, P., Belloni, T., & Stella, L. 2005, ApJ, 629, 403
Chakrabarty, D. 2005, in Astronomical Society of the Pacific Conference Series, Vol. 328, Binary Radio Pulsars, ed. F. A. Rasio & I. H. Stairs, 279
Chakrabarty, D., Bildsten, L., Finger, M. H., et al. 1997, ApJ, 481, L101
Chakrabarty, D., Bildsten, L., Grunsfeld, J. M., et al. 1997, ApJ, 474, 414
Chitnis, V. R., Rao, A. R., Agrawal, P. C., & Manchanda, R. K. 1993, A&A, 268, 609
Coburn, W., Heindl, W. A., Rothschild, R. E., et al. 2002, ApJ, 580, 394
Cook, M. C. & Page, C. G. 1987, MNRAS, 225, 381
Coppi, P. S. 1992, MNRAS, 258, 657
Coppi, P. S. 1999, in ASP Conf. Ser. 161: High Energy Processes in Accreting Black Holes, 375
Cox, N. L. J., Kaper, L., & Mokiem, M. R. 2005, A&A, 436, 661
Cusumano, G., di Salvo, T., Burderi, L., et al. 1998, A&A, 338, L79
de Kool, M. & Anzer, U. 1993, MNRAS, 262, 726
Dennerl, K., Briel, U. G., Haberl, F., et al. 1999, in conf. Proc. SPIE, EUV, X-Ray, and Gamma-Ray Instrumentation for Astronomy X., ed. O. H. Siegmund & K. A. Flanagan, Vol. 3765, 232–243
Dolan, J. F. 1992, ApJ, 384, 249
Donati, J.-F., Howarth, I. D., Bouret, J.-C., et al. 2006, MNRAS, 365, L6
Done, C. & Gierliński, M. 2003, MNRAS, 342, 1041
Done, C., Mulchaey, J. S., Mushotzky, R. F., & Arnaud, K. A. 1992, ApJ, 395, 275
Dove, J. B., Wilms, J., & Begelman, M. C. 1997, ApJ, 487, 747
Dovčiak, M., Karas, V., Martocchia, A., Matt, G., & Yaqoob, T. 2004, in RAGtime 4/5: Workshops on black holes and neutron stars, ed. S. Hledík & Z. Stuchlík, 33–73
Ebisawa, K., Ogawa, M., Aoki, T., et al. 1994, PASJ, 46, 375
Ebisawa, K., Ueda, Y., Inoue, H., Tanaka, Y., & White, N. E. 1996, ApJ, 467, 419
Ehle, M., Breitfellner, M., González Riestra, R., et al. 2005, XMM-Newton Users' Handbook
Elsner, R. F. & Lamb, F. K. 1977, ApJ, 215, 897
Fabian, A. C. 2006, Astronomische Nachrichten, 327, 943
Fabian, A. C., Rees, M. J., Stella, L., & White, N. E. 1989, MNRAS, 238, 729

Fabian, A. C., Vaughan, S., Nandra, K., et al. 2002, MNRAS, 335, L1

Fender, R. 2006, Jets from X-ray binaries (Compact stellar X-ray sources), 381–419

Fender, R., Corbel, S., Tzioumis, T., et al. 1999, ApJL, 519, L165

Fender, R. P., Belloni, T. M., & Gallo, E. 2004, MNRAS, 355, 1105

Fender, R. P., Stirling, A. M., Spencer, R. E., et al. 2006, MNRAS, 369, 603

Fenimore, E. E., Cannon, T. M., van Hulsteyn, D. B., & Lee, P. 1979, Appl. Opt., 18, 945

Ferrigno, C., Segreto, A., Santangelo, A., et al. 2007, A&A, 462, 995

Finger, M. H. 1998, Advances in Space Research, 22, 1007

Frank, J., King, A., & Raine, D. 1992, Cambridge Astrophysics Series, 21

Friend, D. B. & Castor, J. I. 1982, ApJ, 261, 293

Fritz, S., Wilms, J., Pottschmidt, K., et al. 2006, in Proceedings of the X-ray Universe 2005, ed. A. Wilson, ESA SP No. 604 (Noordwijk: ESA Publications Division), 267–268

Frontera, F., Palazzi, E., Zdziarski, A. A., et al. 2001a, ApJ, 546, 1027

Frontera, F., Zdziarski, A. A., Amati, L., et al. 2001b, ApJ, 561, 1006

Gallo, E., Fender, R., Kaiser, C., et al. 2005, Nat, 436, 819

Gallo, E., Fender, R. P., & Pooley, G. G. 2003, MNRAS, 344, 60

Ghosh, P. & Lamb, F. K. 1978, ApJL, 223, L83

Ghosh, P. & Lamb, F. K. 1979a, ApJ, 232, 259

Ghosh, P. & Lamb, F. K. 1979b, ApJ, 234, 296

Ghosh, P., Pethick, C. J., & Lamb, F. K. 1977, ApJ, 217, 578

Giacconi, R., Kellogg, E., Gorenstein, P., Gursky, H., & Tananbaum, H. 1971, ApJ, 165, L27

Gierliński, M., Zdziarski, A. A., Done, C., et al. 1997, MNRAS, 288, 958

Gierliński, M., Zdziarski, A. A., Poutanen, J., et al. 1999, MNRAS, 309, 496

Gies, D. R. & Bolton, C. T. 1982, ApJ, 260, 240

Gies, D. R. & Bolton, C. T. 1986, ApJ, 304, 389

Gies, D. R., Bolton, C. T., Thomson, J. R., et al. 2003, ApJ, 583, 424

Gil, J. A., Melikidze, G. I., & Mitra, D. 2002, A&A, 388, 235

Gilfanov, M., Churazov, E., & Revnivtsev, M. 1999, A&A, 352, 182

Greenhill, J. G., Galloway, D. K., & Murray, J. R. 1999, Proc. Astron. Soc. Aust., 16, 240

Grimm, H.-J., Gilfanov, M., & Sunyaev, R. 2003, MNRAS, 339, 793

Gros, A., Goldwurm, A., Cadolle-Bel, M., et al. 2003, A&A, 411, L179

Gunson, J. & Polychronopulos, B. 1976, MNRAS, 177, 485

Haardt, F. & Maraschi, L. 1991, ApJL, 380, L51

Haardt, F. & Maraschi, L. 1993, ApJ, 413, 507

Harding, A. K. 1994, in American Institute of Physics Conference Series, Vol. 308, The Evolution of X-ray Binariese, ed. S. Holt & C. S. Day, 429

Harding, A. K. & Daugherty, J. K. 1991, ApJ, 374, 687

Harding, A. K. & Lai, D. 2006, Reports of Progress in Physics, 69, 2631

Heindl, W. A. & Chakrabarty, D. 1999, in Highlights in X-ray Astronomy, ed. B. Aschenbach & M. J. Freyberg, 25

Heindl, W. A., Rothschild, R. E., Coburn, W., et al. 2004, in American Institute of

Physics Conference Series, Vol. 714, X-ray Timing 2003: Rossi and Beyond, ed. P. Kaaret, F. K. Lamb, & J. H. Swank, 323–330
Herold, H. 1979, Phys. Rev. D, 19, 2868
Herrero, A., Kudritzki, R. P., Gabler, R., Vilchez, J. M., & Gabler, A. 1995, A&A, 297, 556
Hua, X.-M. & Titarchuk, L. 1995, ApJ, 449, 188
Ibragimov, A., Poutanen, J., Gilfanov, M., Zdziarski, A. A., & Shrader, C. R. 2005, MNRAS, 362, 1435
Ibragimov, A., Zdziarski, A. A., & Poutanen, J. 2007, MNRAS, 381, 723
Illarionov, A. F. & Sunyaev, R. A. 1975, A&A, 39, 185
in 't Zand, J. J. M., Baykal, A., & Strohmayer, T. E. 1998, ApJ, 496, 386
in 't Zand, J. J. M., Heise, J., & Jager, R. 1994, A&A, 288, 665
in 't Zand, J. J. M., Strohmayer, T. E., & Baykal, A. 1997, ApJ, 479, L47
Iye, M. 1986, PASJ, 38, 463
Jahoda, K., Swank, J. H., Giles, A. B., et al. 1996, in conf. Proc. SPIE, EUV, X-Ray, and Gamma-Ray Instrumentation for Astronomy VII, ed. O. H. Siegmund & M. A. Gummin, Vol. 2808, 59–70
Kendziorra, E., Colli, M., Kuster, M., et al. 1999, in conf. Proc. SPIE, EUV, X-Ray, and Gamma-Ray Instrumentation for Astronomy X, ed. O. H. Siegmund & K. A. Flanagan, Vol. 3765, 204–214
Kendziorra, E., Wilms, J., Haberl, F., et al. 2004, in Proceedings of the SPIE, Volume 5488, ed. G. Hasinger & M. J. L. Turner, 613–622
Kippenhahn, R. & Weigert, A. 1994, Stellar Structure and Evolution, corrected 3rd printing 1994 edn. (Stellar Structure and Evolution, XVI, 468 pp. 192 figs.. Springer-Verlag Berlin Heidelberg New York. Also Astronomy and Astrophysics Library)
Kirsch, M. G. F. 1998, PhD thesis, Eberhard-Karls-Universität Tübingen
Kitamoto, S., Miyamoto, S., Tanaka, Y., et al. 1984, PASJ, 36, 731
Kitamoto, S., Takahashi, K., Yamashita, K., Tanaka, Y., & Nagase, F. 1990, PASJ, 42, 85
Kitchin, C. R. 1984, Astrophysical techniques (Bristol, England, Adam Hilger, Ltd., 1984, 451 p.)
Klein, O. & Nishina, Y. 1929, Z. Physik, 52, 853
Krause, N., Briel, U. G., Dennerl, K., et al. 1999, in conf. Proc. SPIE, EUV, X-Ray, and Gamma-Ray Instrumentation for Astronomy X, ed. O. H. Siegmund & K. A. Flanagan, Vol. 3765, 220–230
Kretschmar, P. 1996, PhD thesis, Eberhard-Karls-Universität Tübingen
Kretschmar, P., Kreykenbohm, I., Staubert, R., et al. 1997, in AIP Conf. Proc., Vol. 410, Proc. 4th Compton Symposium, ed. C. D. Dermer, M. S. Strickman, & J. D. Kurfess, Woodbury, 788–792
Kreykenbohm, I. 2004, PhD thesis, Eberhard-Karls-Universität Tübingen
Kreykenbohm, I., Kretschmar, P., Wilms, J., et al. 1999, A&A, 341, 141
Kreykenbohm, I., Wilms, J., Coburn, W., et al. 2004, A&A, 427, 975
Kreykenbohm, I., Wilms, J., Kretschmar, P., et al. 2008, A&A, submitted
Kuster, M., Benlloch, S., Kendziorra, E., & Briel, U. G. 1999, in conf. Proc. SPIE, EUV, X-Ray, and Gamma-Ray Instrumentation for Astronomy X, ed. O. H. Siegmund & K. A. Flanagan, Vol. 3765, 673–682
Lachowicz, P., Zdziarski, A. A., Schwarzenberg-Czerny, A., Pooley, G. G., & Kitamoto, S. 2006, MNRAS,

368, 1025
Lai, D. 2001, Reviews of Modern Physics, 73, 629
Lamb, F. K., Pethick, C. J., & Pines, D. 1973, ApJ, 184, 271
Laor, A. 1991, ApJ, 376, 90
Latal, H. G. 1986, ApJ, 309, 372
Leahy, D. A., Darbro, W., Elsner, R. F., et al. 1983, ApJ, 266, 160
Lebrun, F., Leray, J. P., Lavocat, P., et al. 2003, A&A, 411, L141
Levine, A. M., Bradt, H., Cui, W., et al. 1996, ApJL, 469, L33
Liang, E. P. & Nolan, P. L. 1984, Space Science Reviews, 38, 353
Lightman, A. P. & White, T. R. 1988, ApJ, 335, 57
Longair, M. S. 1992, High energy astrophysics. Vol.1: Particles, photons and their detection (High Energy Astrophysics, by Malcolm S. Longair, pp. 436. ISBN 0521387736. Cambridge, UK: Cambridge University Press, March 1992.)
Longinotti, A. L., Nandra, K., Petrucci, P. O., & O'Neill, P. M. 2004, MNRAS, 355, 929
Lubiński, P., Dubath, P., Paltani, S., Walter, R., & Courvoisier, T. 2005, INTEGRAL cross calibration status for OSA 5.1
Lund, N., Budtz-Jørgensen, C., Westergaard, N. J., et al. 2003, A&A, 411, L231
Magdziarz, P. & Zdziarski, A. A. 1995, MNRAS, 273, 837
Makishima, K., Kawai, N., Koyama, K., et al. 1984, PASJ, 36, 679
Makishima, K., Maejima, Y., Mitsuda, K., et al. 1986, ApJ, 308, 635
Makishima, K., Mihara, T., Nagase, F., & Murakami, T. 1992, in Proc. 28th Yamada Conference: Frontiers of X-ray Astronomy, ed. Y. Tanaka & K. Koyama, Frontiers Science Series (Tokyo: Universal Academy Press), 23
Makishima, K., Ohashi, T., Sakao, T., et al. 1988, Nat, 333, 746
Malzac, J. & Jourdain, E. 1998, in 19th Texas Symposium on Relativistic Astrophysics and Cosmology, ed. J. Paul, T. Montmerle, & E. Aubourg
Markoff, S., Falcke, H., & Fender, R. 2001, A&A, 372, L25
Markoff, S., Nowak, M., Corbel, S., Fender, R., & Falcke, H. 2003, A&A, 397, 645
Marshall, F. E., Mushotzky, R. F., Petre, R., & Serlemitsos, P. J. 1993, ApJ, 419, 301
Marshall, N. & Ricketts, M. J. 1980, MNRAS, 193, 7
Mauche, C. W., Liedahl, D. A., Akiyama, S., & Plewa, T. 2007, Progress of Theoretical Physics Supplement, 169, 196
McClintock, J. E., Haswell, C. A., Garcia, M. R., et al. 2001, ApJ, 555, 477
McClintock, J. E. & Remillard, R. A. 2003, ArXiv Astrophysics e-prints
McClintock, J. E. & Remillard, R. A. 2006, Black hole binaries (Compact stellar X-ray sources), 157–213
McConnell, M. L., Zdziarski, A. A., Bennett, K., et al. 2002, ApJ, 572, 984
Mihara, T. 1995, PhD thesis, RIKEN, Tokyo
Miller, J. M. 2006, Astronomische Nachrichten, 327, 997
Miller, J. M., Fabian, A. C., Wijnands, R., et al. 2002, ApJ, 578, 348
Mitsuda, K., Inoue, H., Koyama, K., et al. 1984, PASJ, 36, 741
Mony, B., Kendziorra, E., Maisack, M., et al. 1991, A&A, 247, 405
Mukerjee, K., Agrawal, P. C., Paul, B., et al. 2001, ApJ, 548, 368
Murray, J. R., de Kool, M., & Li, J. 1999, ApJ, 515, 738
Nagel, W. 1981, ApJ, 251, 288
Nice, D. J., Splaver, E. M., Stairs, I. H., et al.

2005, ApJ, 634, 1242
Ninkov, Z., Walker, G. A. H., & Yang, S. 1987, ApJ, 321, 425
Nishimura, J., Mitsuda, K., & Itoh, M. 1986, PASJ, 38, 819
Nishimura, O. 2005, PASJ, 57, 769
Nowak, M. A., Wilms, J., Heinz, S., et al. 2005, ApJ, 626, 1006
Oda, M. 1977, Space Science Reviews, 20, 757
Padmanabhan, P. 2000, Theoretical astrophysics. Vol.1: Astrophysical processes (Theoretical astrophysics. Vol.1: Astrophysical processes, Cambridge, MA: Cambridge University Press, 2000, xix, 601 p. ISBN 0521566320)
Peacock, A. 1984, Physica Scripta, 7, 216
Perna, R., Bozzo, E., & Stella, L. 2006, ApJ, 639, 363
Pfeiffer, H. P. & Lai, D. 2004, ApJ, 604, 766
Pooley, G. G., Fender, R. P., & Brocksopp, C. 1999, MNRAS, 302, L1
Pottschmidt, K. 2002, PhD thesis, Eberhard-Karls-Universität Tübingen
Pottschmidt, K., Kreykenbohm, I., Wilms, J., et al. 2005, ApJL, 634, L97
Poutanen, J. & Svensson, R. 1996, ApJ, 470, 249
Pozdnyakov, L. A., Sobol, I. M., & Sunyaev, R. A. 1979, A&A, 75, 214
Proctor, R. J., Skinner, G. K., & Willmore, A. P. 1979, MNRAS, 187, 633
Protassov, R., van Dyk, D. A., Connors, A., Kashyap, V. L., & Siemiginowska, A. 2002, ApJ, 571, 545
Psaltis, D. 2006, Accreting neutron stars and black holes: a decade of discoveries (Compact stellar X-ray sources), 1–38
Reis, R. C., Fabian, A. C., Ross, R., et al. 2008, ArXiv e-prints, 804
Reisenegger, A., Prieto, J. P., Benguria, R., Lai, D., & Araya, P. A. 2005, in American Institute of Physics Conference Series, Vol. 784, Magnetic Fields in the Universe: From Laboratory and Stars to Primordial Structures., ed. E. M. de Gouveia dal Pino, G. Lugones, & A. Lazarian, 263–273
Remillard, R. A. & McClintock, J. E. 2006, ARA&A, 44, 49
Reynolds, C. S. & Nowak, M. A. 2003, Phys. Rep, 377, 389
Roberts, M. S. E., Michelson, P. F., Leahy, D. A., et al. 2001, ApJ, 555, 967
Ross, R. R. & Fabian, A. C. 1993, MNRAS, 261, 74
Ross, R. R. & Fabian, A. C. 2005, MNRAS, 358, 211
Ross, R. R. & Fabian, A. C. 2007, MNRAS, 381, 1697
Roth, S. 2008, Master's thesis, Friedrich-Alexander Universität Erlangen-Nürnberg
Rothschild, R. E., Blanco, P. R., Gruber, D. E., et al. 1998, ApJ, 496, 538
Ruderman, M. 2005, in NATO ASIB Proc. 210: The Electromagnetic Spectrum of Neutron Stars, ed. A. Baykal, S. K. Yerli, S. C. Inam, & S. Grebenev, 47
Rybicki, G. B. & Lightman, A. P. 1979, Radiative processes in astrophysics (New York, Wiley-Interscience)
Santangelo, A., Segreto, A., Giarrusso, S., et al. 1999, ApJL, 523, L85
Schwartz, D. A., Griffiths, R. E., Bowyer, S., Thorstensen, J. R., & Charles, P. A. 1980, AJ, 85, 549
Schönherr, G. 2007, PhD thesis, Eberhard-Karls-Universität Tübingen
Shakura, N. I. & Syunyaev, R. A. 1973, A&A, 24, 337
Shaposhnikov, N. & Titarchuk, L. 2007, ApJ, 663, 445
Shirakawa, A. & Lai, D. 2002, ApJ, 564, 361
Srinivasan, G. 1997, in Saas-Fee Advanced

Course 25. Lecture Notes 1995. Swiss Society for Astrophysics and Astronomy: Stellar remnants, p. 97 - 235, ed. S. D. Kawaler, I. Novikov, & G. Srinivasan, 97–235

Stirling, A., Spencer, R., & Garrett, M. 1998, New Astronomy Review, 42, 657

Stirling, A. M., Spencer, R. E., de la Force, C. J., et al. 2001, MNRAS, 327, 1273

Strüder, L., Briel, U., Dennerl, K., et al. 2001, A&A, 365, L18

Sunyaev, R. & Revnivtsev, M. 2000, A&A, 358, 617

Sunyaev, R. A. & Titarchuk, L. G. 1980, A&A, 86, 121

Sunyaev, R. A. & Trümper, J. 1979, Nat, 279, 506

Svensson, R. 1982, ApJ, 258, 335

Tanaka, Y. 1986, in Radiation Hydrodynamics in Stars and Compact Objects, ed. D. Mihalas & K.-H. A. Winkler, IAU Coll. No. 89 (Heidelberg: Springer), 198

Tauris, T. M. & van den Heuvel, E. P. J. 2006, Formation and evolution of compact stellar X-ray sources (Compact stellar X-ray sources), 623–665

Thompson, C. & Duncan, R. C. 1993, ApJ, 408, 194

Titarchuk, L. 1994, ApJ, 434, 570

Titarchuk, L. & Hua, X.-M. 1995, ApJ, 452, 226

Titarchuk, L. & Lyubarskij, Y. 1995, ApJ, 450, 876

Tomsick, J. A., Kalemci, E., Kaaret, P., et al. 2008, ArXiv e-prints, 802

Trümper, J., Sacco, B., Pietsch, W., et al. 1977, Mitteilungen der Astronomischen Gesellschaft Hamburg, 42, 120

Turner, M. J. L., Abbey, A., Arnaud, M., et al. 2001, A&A, 365, L27

Turon, C., Crézé, M., Egret, D., Gómez, A., et al. 1992, The Hipparcos Input Catalogue, ESA-SP No. 1136 (Noordwijk: ESA Publications Division)

Ubertini, P., Lebrun, F., Di Cocco, G., et al. 2003, A&A, 411, L131

van den Heuvel, E. P. J. 1975, ApJL, 198, L109

van der Klis, M. 2000, ARA&A, 38, 717

van der Klis, M. 2006, Compact stellar X-ray sources, 39

van Kerkwijk, M. H., van Oijen, J. G. J., & van den Heuvel, E. P. J. 1989, A&A, 209, 173

Vedrenne, G., Roques, J.-P., Schönfelder, V., et al. 2003, A&A, 411, L63

Verner, D. A. & Yakovlev, D. G. 1995, A&AS, 109, 125

Vrtilek, S. D., Boroson, B., Hunacek, A., Gies, D., & Bolton, C. T. 2007, ArXiv e-prints, 710

Walborn, N. R. 1973, ApJ, 186, 611

Wang, Y.-M. 1995, ApJL, 449, L153

Watarai, K.-y., Fukue, J., Takeuchi, M., & Mineshige, S. 2000, PASJ, 52, 133

Webb, N. A. & Barret, D. 2007, ApJ, 671, 727

Wen, L., Cui, W., Levine, A. M., & Bradt, H. V. 1999, ApJ, 525, 968

White, T. R., Lightman, A. P., & Zdziarski, A. A. 1988, ApJ, 331, 939

Wilms, J. 1996, Master's thesis, Eberhard-Karls-Universität Tübingen

Wilms, J. 1998, PhD thesis, Eberhard-Karls-Universität Tübingen

Wilms, J. 2001, Astrophysical Radiation Processes, Lecture, `http://astro.uni-tuebingen.de/~wilms/teach/radproc/`

Wilms, J., Nowak, M. A., Pottschmidt, K., Pooley, G. G., & Fritz, S. 2006, A&A, 447, 245

Wilms, J., Pottschmidt, K., Pooley, G. G., et al. 2007, ApJL, 663, L97

Wilms, J., Speith, R., & Reynolds, C. S. 1998, in Lecture Notes in Physics, Berlin

Springer Verlag, Vol. 514, Black Holes: Theory and Observation, ed. F. W. Hehl, C. Kiefer, & R. J. K. Metzler, 69
Winkler, C., Courvoisier, T. J.-L., Di Cocco, G., et al. 2003, A&A, 411, L1
Wolter, H. 1952a, Annalen der Physik, 445, 94
Wolter, H. 1952b, Annalen der Physik, 445, 286
Woosley, S. E., Heger, A., & Weaver, T. A. 2002, Reviews of Modern Physics, 74, 1015
Woosley, S. E. & Weaver, T. A. 1986, ARA&A, 24, 205
Yahel, R. Z. 1979, ApJL, 229, L73
Ziółkowski, J. 2005, MNRAS, 358, 851

Appendix A

# Calibration of Modified Timing mode

Table A.1: Log of observations. – Part I

| Obsid | Source | Filter | Type | Count Rate (cts/s) | selected |
|---|---|---|---|---|---|
| 0023940401 | LMC X-1 | Thin1 | HMXB | 128 | X |
| 0031740101 | PSR J0034-0534 | Medium | Pulsar | 1 | |
| 0036140201 | XB 1323-619 | Thin1 | LMXB | 27 | X |
| 0060740101 | XB 1254-69 | Thin1 | LMXB | 182 | X |
| 0060740901 | XB 1254-69 | Thin1 | LMXB | 201 | X |
| 0061140101 | X0918-54 | Medium | | 63 | X |
| 0061140201 | X1543-62 | Medium | LMXB | 223 | |
| 0064940101 | SAX J1808.4-3658 | Thin1 | LMXB | 0 | |
| 0073140201 | 1RXSJ160518.8+32490 | Thin1 | Object of unknown nature | 6 | X |
| 0073140301 | 1RXSJ160518.8+32490 | Thin1 | Object of unknown nature | 6 | X |
| 0073140501 | 1RXSJ160518.8+32490 | Thin1 | Object of unknown nature | 14 | X |
| 0074140101 | 4U 1608-52 | Thin1 | LMXB | 14 | X |
| 0074140201 | 4U 1608-52 | Thin1 | LMXB | 5 | X |
| 0085290301 | 4U1915-05 | Medium | LMXB | 61 | X |
| 0085680501 | GX 339-4 | Medium | LMXB | 0 | |
| 0085680601 | GX 339-4 | Medium | LMXB | 0 | |
| 0087350101 | X2127+119 | Medium | LMXB | 71 | X |
| 0087350601 | X2127+119 | Medium | LMXB | 74 | X |
| 0087350801 | X2127+119 | Medium | LMXB | 92 | X |
| 0090340101 | U1728-16 | Thin1 | LMXB | 1372 | |
| 0090340201 | U1735-44 | Thin1 | LMXB | 1192 | |
| 0090340601 | U1728-16 | Thin1 | LMXB | 1469 | |
| 0092820101 | PSR 1259-63 | Medium | Pulsar | 2 | |

Table A.2: Log of observations. – Part II

| Obsid | Source | Filter | Type | Count Rate (cts/s) | selected |
|---|---|---|---|---|---|
| 0092820201 | PSR 1259-63 | Medium | Pulsar | 4 | X |
| 0092820301 | PSR 1259-63 | Medium | Pulsar | 1 | |
| 0092820801 | PSR J0034-0534 | Medium | Pulsar | 2 | |
| 0092821201 | PSR 1259-63 | Medium | Pulsar | 0 | |
| 0094520201 | Circinius X-1 | Thin1 | LMXB | 92 | X |
| 0094520301 | Circinius X-1 | Thin1 | LMXB | 158 | |
| 0099280101 | Mkn 421 | Thick | BL Lac type object | 319 | X |
| 0109090101 | LMC X-3 | Medium | HMXB | 541 | |
| 0109463801 | V834 Cen | Thin1 | Cataclysmic var. AM Her type | 1 | |
| 0111030101 | Vela X-1 | Thick | HMXB | 50 | |
| 0111040101 | 4U0614+09 | Thick | LMXB | 258 | |
| 0111060101 | Her X-1 | Medium | XRB | 23 | X |
| 0111061201 | Her X-1 | Medium | XRB | 51 | X |
| 0111061301 | Her X-1 | Medium | XRB | 12 | X |
| 0111061401 | Her X-1 | Medium | XRB | 17 | X |
| 0111061501 | Her X-1 | Medium | XRB | 48 | X |
| 0111061601 | Her X-1 | Medium | XRB | 13 | X |
| 0111061701 | Her X-1 | Medium | XRB | 15 | X |
| 0111061801 | Her X-1 | Medium | XRB | 31 | X |
| 0111062101 | Her X-1 | Medium | XRB | 19 | X |
| 0111062301 | Her X-1 | Medium | XRB | 36 | X |
| 0111062501 | Her X-1 | Medium | XRB | 90 | X |
| 0111062601 | Her X-1 | Medium | XRB | 29 | X |

Table A.3: Log of observations. – Part III

| Obsid | Source | Filter | Type | Count Rate (cts/s) | selected |
|---|---|---|---|---|---|
| 0111100101 | PSR J0218+42 | Thin1 | Pulsar | 1 | |
| 0111100301 | PSR J0751+18 | Thin1 | Pulsar | 1 | |
| 0111230101 | X1822-371 | Medium | LMXB | 63 | X |
| 0111310201 | SS Cyg | Medium | Dwarf Nova | 41 | X |
| 0111370101 | AR Lacertae | Thick | Variable of RS CVn type | 24 | X |
| 0111390101 | UX Arietis | Medium | Variable of RS CVn type | 36 | X |
| 0111390301 | UX Arietis | Medium | Variable of RS CVn type | 32 | X |
| 0111400101 | Pi1 Ursae Majoris | Medium | Variable Star | 3 | X |
| 0111410101 | Kappa1 Ceti | Medium | Variable Star | 7 | X |
| 0111470101 | Sigma2 CrB | Medium | Variable of RS CVn type | 69 | X |
| 0111470201 | Sigma2 CrB | Medium | Variable of RS CVn type | 66 | X |
| 0111470301 | Sigma2 CrB | Medium | Variable of RS CVn type | 66 | X |
| 0111490101 | VY Arietis | Medium | Variable of RS CVn type | 24 | X |
| 0111490401 | VY Arietis | Medium | Variable of RS CVn type | 16 | X |
| 0111500101 | Chi1 Orionis | Medium | High proper-motion star | 16 | X |
| 0112200101 | PSR0656+14 | Thin1 | Pulsar | 5 | X |
| 0112320101 | PSR J0030+0451 | Thin1 | Pulsar | 2 | |
| 0112320201 | PSR J0437-4715 | Thin1 | Pulsar | 1 | |
| 0112320301 | PSR J1024-0719 | Thin1 | Pulsar | 0 | |
| 0112320601 | PSR J2124-3358 | Thin1 | Pulsar | 2 | |
| 0112440101 | Aql X-1 | Thin1 | LMXB | 7 | X |
| 0112440301 | Aql X-1 | Thin1 | LMXB | 0 | |
| 0112440401 | Aql X-1 | Thin1 | LMXB | 0 | |

Table A.4: Log of observations. – Part IV

| Obsid | Source | Filter | Type | Count Rate (cts/s) | selected |
|---|---|---|---|---|---|
| 0112781001 | 4U 0155+63 | Medium | HMXB | 2 | |
| 0112900101 | LMC X-1 | Thick | HMXB | 130 | X |
| 0112900201 | GX 339-4 | Thick | LMXB | 0 | |
| 0113020201 | PSR J0537-6909 | Medium | Pulsar | 4 | X |
| 0113050101 | PSR 1055-52 | Medium | Pulsar | 1 | |
| 0113050201 | PSR 1055-52 | Medium | Pulsar | 1 | |
| 0113050701 | 1E 1613-5055 off | Medium | X-ray source | 27 | X |
| 0122340101 | GX13+1 | Medium | LMXB | 651 | |
| 0122340901 | GX13+1 | Medium | LMXB | 757 | |
| 0122341001 | GX13+1 | Medium | LMXB | 669 | |
| 0124710401 | Coma4 | CalClosed | | 5 | |
| 0124930301 | PKS2155-304 | Medium | BL Lac type object | 175 | X |
| 0124930601 | PKS2155-304 | Thick | BL Lac type object | 46 | X |
| 0125100101 | N132D | Medium | SNR | 51 | |
| 0125100301 | N132D | Medium | SNR | 100 | |
| 0125120201 | PSR0540 on axis | Medium | Pulsar | 33 | X |
| 0126130201 | AB Dor | CalClosed | Rotationally variable star | 5 | |
| 0127720501 | V4743 Sgr | Thin1 | Nova | 1089 | |
| 0128120401 | PSR 1509 | Medium | Pulsar | 8 | X |
| 0133120101 | AB Dor | Thick | Rotationally variable star | 18 | X |
| 0134120101 | Her X-1 | Medium | XRB | 401 | |
| 0134721501 | Capella | Thick | Variable of RS CVn type | 63 | |
| 0136541001 | Mkn 421 | Medium | BL Lac type object | 246 | |

Table A.5: Log of observations. – Part V

| Obsid | Source | Filter | Type | Count Rate (cts/s) | selected |
|---|---|---|---|---|---|
| 0137550301 | Cas A | Medium | SNR | 169 | |
| 0137551001 | 3C 273 | Medium | Quasar | ? | |
| 0148220201 | GX 339-4 | Medium | LMXB | 844 | |
| 0148220301 | GX 339-4 | Medium | LMXB | 1001 | |
| 0148590201 | BY Cam | Thin1 | Cataclysmic var. AM Her type | 16 | X |
| 0148590301 | BY Cam | Thin1 | Cataclysmic var. AM Her type | 14 | X |
| 0148590401 | BY Cam | Thin1 | Cataclysmic var. AM Her type | 22 | X |
| 0148590501 | BY Cam | Thin1 | Cataclysmic var. AM Her type | 17 | X |
| 0148590701 | BY Cam | Thin1 | Cataclysmic var. AM Her type | 18 | X |
| 0148590801 | BY Cam | Thin1 | Cataclysmic var. AM Her type | 13 | X |
| 0148590901 | BY Cam | Thin1 | Cataclysmic var. AM Her type | 12 | X |
| 0149550401 | SAX J2103.5+4545 | Thick | HMXB | 34 | X |
| 0149810101 | 4U 1728-34 | Thick | LMXB (slow burster?) | 89 | X |
| 0150498701 | Mkn 421 | Thin1 | BL Lac type object | 666 | |
| 0153090101 | HU Aqr | Thin1 | Cataclysmic var. AM Her type | 3 | X |
| 0153750401 | Crab | Thick | SNR | 1965 | |
| 0154750301 | XTE J1751-305 | Thin1 | Millisecond XRP | 96 | X |
| 0154750601 | IGR J17544-2619 | Thin1 | Gamma-ray source | 8 | |
| 0157960101 | XTE J1807-294 | Thick | LMXB | 39 | X |
| 0159360401 | Zeta Puppis | Thick | Variable of BY Dra type | 4 | X |
| 0160960201 | Crab | Thick | SNR | 1927 | |
| 0160960301 | Crab | Thick | SNR | 1930 | |
| 0164570301 | 1E 1048.1-5937 | Medium | HMXB | 4 | X |

In the following the comparison plots between the standard Timing mode RMF and the Modified Timing mode RMF for the "thin1" and “medium” filter are shown. Both plots show that the newly calculated response matrix is perfectly able to account for the effects of the spectral softening as described in the text in section 4.3.1.

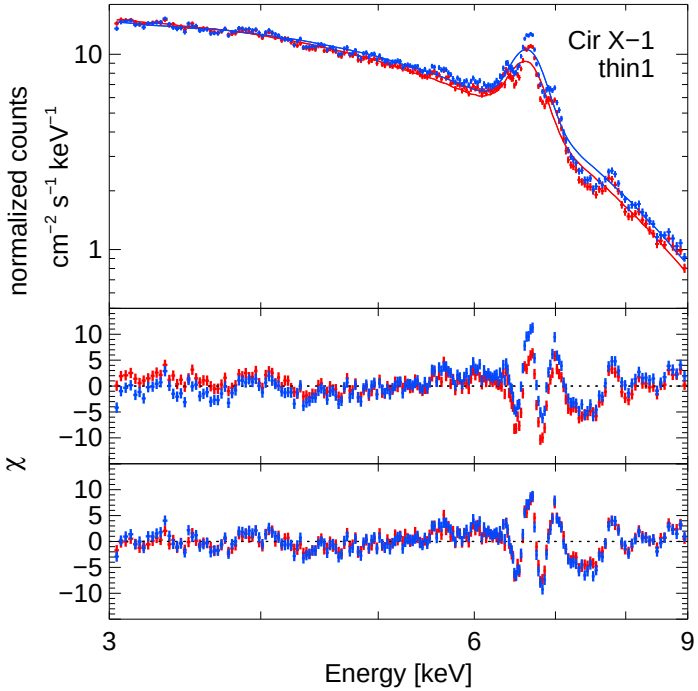


Figure A.1: Comparison of the standard Timing mode response matrix and the newly calculated response matrix for the Modified Timing mode for the "thin1" filter. The red spectrum is a simulated modified Timing mode observation of Cir X-1 whereas the blue one shows the normal Timing mode observation. The upper panel displays the residuals for a fit to the data just using the standard rmf and arf files for both observations, resulting in differences in the data. The bottom panel shows the same but now using the correct response matrix for the Modified Timing mode.

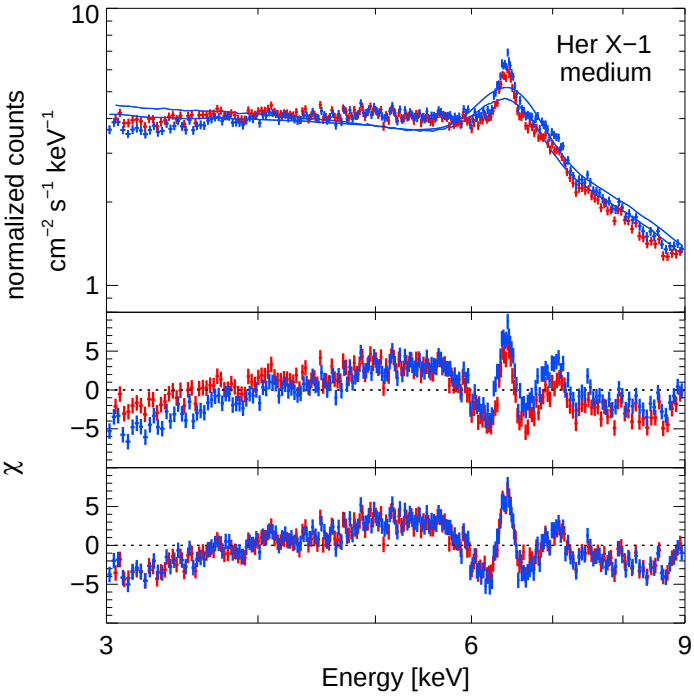


Figure A.2: Same comparison as in Fig A.1. The source chosen is Her X-1, the observation was executed with the medium filter.

# *Acknowledgments*

I'd like to thank all the people who helped me during my PhD years in many ways:

First of all a really BIG thank you goes to Prof. Jörn Wilms for his continued support and never ending patience in answering my questions. He is also to blame for organizing a DAAD grant which allowed me to spent two very interesting weeks at the University of California, San Diego.

The second thank you goes to Prof. Andrea Santangelo for the possibility to write this thesis in his working group.

I am very grateful to Prof. Rüdiger Staubert for his support in analyzing the 4U 1907+09 data and for always being available for advice.

Many thanks go to Dr. Ingo Kreykenbohm for his never ending help in all problems of "everyday science life" and for his continued interest in 4U 1907+09 which only made the paper possible in the first place.

Dr. Eckhard Kendziorra always found time to answer questions about *XMM-Newton* in general or the Modified Timing mode in particular. Another thing he always found was the money to send me to several conferences as well as the summer school on astroparticle physics. Thanks a lot for that.

Many thanks go to Dr. Thorsten Nagel for lots of helpful discussions. He has always been working as assistant not only for the stellar atmosphere group but also for our X-ray group. Thanks, Thorsten!!!

I owe another big thank you to the "Jungs" in Bamberg. They always made me feel really welcome during my visits there. A special thank you goes to Manfred Hanke and Moritz Böck "fürs Hirn verknoten" and for many more discussions and their help. It's good to see that Bamberg has become a place like Tübingen used to be.

A special thank you also goes to Agnes Hoffmann – not only for her help in structuring chapters 4 and 5, but also for many more helpful discussions.

Michael Martin also deserves a big thank you for introducing me into the secrets of detector physics as well as for many comforting chats and cups of coffee.

Without the "Espressorunde" and #ait the PhD years would not have been the same. Thanks to you all.

I'd like to thank Elke Reiff for always being the best friend one could imagine. I really missed the shared lunch breaks, the AADs, and the many serious and witty discussions during the last eight months.

I am grateful to Susanne Limpert, Daniel Duffner, and Franziska Piontek for reminding me that there is a life outside university and for staying friends during all those years.

A very special thank you goes to the “private” Ingo for the last two years which have been simply wonderful, and for his encouragement and motivation especially during the last weeks of writing this thesis. Thank you so much that you are always there!

Last but not least I want to deeply thank my parents for enabling me to study physics and supporting me in any conceivable way.

# *Curriculum Vitae*

| | |
|---|---|
| 14. March 1980 | born in Tübingen, Germany |
| 08.1986 – 07.1990 | Elementary school Metzingen-Neuhausen |
| 09.1990 – 06.1999 | Gymnasium (High School) Metzingen |
| 06.1999 | Abitur (High School Graduation) |
| 09.1999 – 12.2004 | Eberhard-Karls Universität Tübingen<br>major: physics |
| 12.2003 – 12.2004 | preparation of the Diploma-Thesis:<br>"Die *INTEGRAL* Galactic Plane Scans"<br>under the supervision of R. Staubert at the IAAT |
| 12.2004 | Diploma |
| 12.2004 – 06.2008 | Scientific employee at the IAAT (part time) |
| 12.2004 – 06.2008 | Preparation of this thesis entitled<br>"X-ray observations of black hole and neutron star binary systems"<br>under the supervision of J. Wilms (U. Erlangen-Nürnberg) and A. Santangelo at the IAAT |

My academic teachers have been the professors and lecturers:

| | |
|---|---|
| Astronomy | : A. Santangelo, E. Haug, J. Frauendiener, W. Kley, R. Staubert, K. Werner, J. Wilms |
| Chemistry | : H. Ebert, J. Strähle |
| Business Studies | : W. Neuss, R. Berndt, F. X. Bea |
| Experimental Physics | : H. Clement, P. Grabmayr, R. Kleiner, R. Maier, G. Wagner, M. Weitz, C. Zimmermann |
| Mathematics | : H. Fischer, M. Wolff |
| Theoretical Physics | : M. Liu, H. Müther, N. Schopohl |